

The Ursa Major Supercluster of Galaxies: II. The Structure and Peculiar Velocities

F. G. Kopylova and A. I. Kopylov*

Special Astrophysical Observatory, Russian Academy of Sciences, Nizniĭ Arkhyz, Karachaevo-Cherkessia, 357147 Russia
Received October 30, 2000

Abstract—Kormendy's relation ($\mu_e - \log R_e$) is used to investigate the structure of the compact Ursa Major supercluster of galaxies ($11^{\text{h}}30^{\text{m}} + 55^\circ$, $cz = 18\,000 \text{ km s}^{-1}$); this relation allows the distances of early-type galaxies to be estimated. The relative distances of 13 clusters in the supercluster and their peculiar velocities are determined with a mean statistical accuracy of 6%. In general, the supercluster obeys the Hubble relation between radial velocity and distance. However, there is reason to suggest that the supercluster consists of two subsystems with mean radial velocities of 16 200 and 19 700 km s^{-1} . For a velocity dispersion in the subsystems of $\sim 1\,100 \text{ km s}^{-1}$, the fact that each of them is gravitationally bound is not ruled out. © 2001 MAIK "Nauka/Interperiodica".

Key words: *galaxies, groups and clusters of galaxies*

INTRODUCTION

The distribution of galaxies and clusters of galaxies is revealed by redshift measurements. Its pattern is distorted by peculiar motions additional to the Hubble expansion that arise as space structures grow due to gravitation. The most contrasting structures on scales of 30–300 Mpc are superclusters of galaxies. It follows from galaxy redshift surveys that the sizes of superclusters reach 20–100 Mpc and their masses are $\sim 10^{16} M_\odot$ (below, we use $H_0 = 50 \text{ km s}^{-1} \text{ Mpc}^{-1}$ and $q_0 = 0.5$). The growth of nonuniformities in the matter distribution at the linear stage of the development of gravitational instability or at the onset of gravitational collapse in the most compact systems can be traced by the distribution and motion of clusters in superclusters.

The observationally determined peculiar velocities of galaxy clusters generally do not exceed 1000 km s^{-1} . One might expect larger velocities in rare, compact, and rich superclusters of galaxies, which exhibit elongation along the line of sight if their distances are assumed to be directly proportional to the redshifts of their constituent galaxy clusters. The Ursa Major and Corona Borealis superclusters in the northern sky are of greatest interest in this respect (Rood 1992).

For the component additional to the Hubble component (peculiar velocity) to be separated from the directly observed velocity (cz), the positions of clusters within the supercluster along the line of sight must be determined by a method independent of redshift determination. We used Kormendy's relation for early-type

(E and S0) galaxies, which dominate at the cluster center, as this method.

Using this purely photometric method, we investigated the structure and peculiar motions in various systems of galaxies: in two compact superclusters of galaxies and in the system of galaxy clusters surrounding a void (Kopylov and Kopylova 1998). Our sample includes 39 clusters, in which we measured ~ 440 galaxies in total. Our study of the compact Corona Borealis supercluster (Kopylova and Kopylov 1998) shows that the nucleus of this system composed of eight rich Abell clusters is gravitationally bound and is at the stage of gravitational collapse. Preliminary estimates of peculiar cluster motions around the void revealed a small outward-directed motion of clusters (Kopylov and Kopylova 1998). Here, our goal is to determine the structure (along the line of sight) of the second compact supercluster in the northern sky, Ursa Major ($11^{\text{h}}30^{\text{m}} + 55^\circ$, $cz = 18\,000 \text{ km s}^{-1}$). In comparison with our previous paper (Kopylov and Kopylova 1996), we made more accurate measurements for a larger number of galaxies and added two additional clusters (A1452 and A1507) located on the periphery of the supercluster.

OBSERVATIONS AND PHOTOMETRIC MEASUREMENTS

Ursa Major is one of the nearest ($z \approx 0.06$) compact superclusters. Figure 1 shows the cluster positions in the sky in equatorial coordinates. As we see from the figure, the supercluster is a compact group of clusters, at least in projection onto the sky. The apparent density contrast of the system, if it is determined with respect to the number of Abell clusters in the surrounding region of ~ 200 Mpc in size, is 30. A more detailed

* E-mail address for contacts: akop@sao.ru

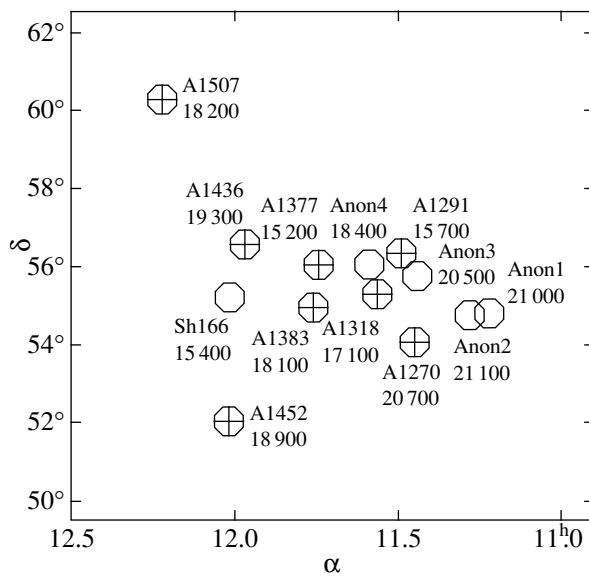


Fig. 1. The positions of clusters from the Ursa Major supercluster in equatorial coordinates at epoch B1950. Cluster numbers and mean radial velocities rounded off to 100 km s^{-1} are shown. Clusters from the catalog by Abell *et al.* (1989) are marked by circled crosses; other clusters (Baier 1980; Shectman 1985) are marked by circles.

description of the clusters in the supercluster and their luminosity function can be found in Kopylov and Kopylova (2001), where the sample of objects (bright E and S0 galaxies in clusters) was drawn by using the $B-R$ color index. We determined the redshifts of galaxies and clusters from the spectra taken in 1991–1993 with a 1024-channel photon counter—the scanner (IPSC) mounted at the Nasmyth-1 focus of the 6-m telescope on the SP-124 spectrograph (Drabek *et al.* 1986; Afanas'ev *et al.* 1986). The observations were carried out with the B1 grating ($600 \text{ lines mm}^{-1}$) in the spectral range 3600 to 5500 \AA with a dispersion of 1.9 \AA per channel. The accuracy of measuring radial velocities was $100\text{--}200 \text{ km s}^{-1}$.

We determined the photometric parameters for 107 galaxies in 13 clusters from direct (Cron–Cousins) R_c images obtained with the 6-m Special Astrophysical Observatory (SAO) telescope in 1992–1994 and with a 1-m telescope in 1996–1998. The images were obtained at a mean seeing of $1''.7 \pm 0''.3$ measured as the $FWHM$ profiles of stars. We used an ISD015A 520×580 CCD array with a pixel size of $18 \times 24 \text{ \mu m}$, which corresponded to angular sizes of $0''.28 \times 0''.37$ and $0''.154 \times 0''.205$ on the 1-m and 6-m telescopes, respectively. The exposure time was 200 and 500 s on the 6-m and 1-m telescopes, respectively. For photometric calibration, standard stars from Landolt (1992) were observed several times during each night. The 1-m telescope observations were performed on most of the photometric nights.

The observational data were reduced with the PC VISTA (Treffers and Richmond 1989) and MIDAS (Munich Image Data Analysis System) (Grosbol 1989) packages. We also used the RING code (Georgiev 1991), which we adapted for surface photometry of galaxies through circular apertures. The standard image processing procedures were applied: median-dark-frame subtraction, flat fielding, and subtraction of the sky background fitted by a second-degree surface. Based on multi-aperture photometry, we determined the asymptotic total magnitudes of galaxies. The total magnitude was then used to determine the effective radius r_e at which the galaxy luminosity decreased by half and the effective surface brightness μ_e at this radius [see Kopylova and Kopylov (1998) for more details on this technique]. The photometric parameters were corrected for seeing by the method described in Saglia *et al.* (1993). By comparing independent measurements for 15 galaxies that we observed twice, we found the rms measurement errors of μ_e and $\log r_e$ to be $0''.09$ and 0.02 , respectively.

For several large galaxies with extended envelopes, i.e., those of type cD (these include galaxies 61 in Anon1, 157 and 97 in A1377, and 80 and 19 in A1318), we determined the parameters by fitting an $r^{1/4}$ profile (de Vaucouleurs 1948) to the observed surface brightness profile. We had to do this, because the extended envelopes of these galaxies were partially outside our images.

Our photometric and spectroscopic measurements are given in Table 1.¹ The table lists the following galaxy parameters: Abell cluster numbers; galaxy numbers [all numbers correspond to those from Kopylov and Kopylova (2001)]; galaxy equatorial coordinates at epoch B1950; total (asymptotic) R_c magnitudes; heliocentric radial velocities, in km s^{-1} ; effective galaxy radii, in arcseconds, corrected for seeing; effective surface brightnesses (mag arcsec^{-2}) at the effective radius corrected for seeing; and mean effective surface brightnesses (mag arcsec^{-2}) within the effective radius corrected for seeing. In A1377, the radial velocities for the four galaxies marked in Table 1 by an asterisk were taken from Humason *et al.* (1956). In the same cluster, we give the coordinates for two other galaxies, designated as D45 and D47, from Dressler (1980). They are located near the region we studied (Kopylov and Kopylova 2001) and were additionally included in the list for CCD photometry, because they were classified by Dressler (1980) as S0 and E, respectively.

Data for the two additional clusters, A1452 and A1507, which we have not studied previously, are presented in Table 2. It gives the same parameters as those in Table 1 and the coordinates of galaxies at epoch B1950. The radial velocities for the galaxies in A1452

¹ Table 1 is published in electronic form only and is accessible via <ftp://cdsarc.u-strasbg.fr/pub/cats/J> (130.79.128.5) or at <http://cdsweb.u-strasbg.fr/pub/cats/J>.

Table 2. Data for two additional clusters

Cluster	Galaxy	α	δ	m_R	$V_h, \text{ km s}^{-1}$	r_e	μ_e	$\langle \mu_e \rangle$
A1452	2	12 ^h 00 ^m 34. ^s 23	51°57'12."3	14.00	19014	8."97	22.03	20.74
	1	12 00 55.48	51 59 37.8	14.04	18272	7.18	21.64	20.30
	5	12 00 49.46	52 05 57.4	15.34	18333	2.48	20.56	19.29
	10	12 00 36.85	51 57 22.8	15.77	18173	2.72	21.19	19.94
A1507	5	12 12 21.83	60 11 01.5	13.91	18100	9.02	21.83	20.67
	4	12 12 52.81	60 14 42.2	14.43	18106	5.26	21.17	20.03
	10	12 13 57.45	60 18 33.4	15.03		2.79	20.55	19.26
	8	12 13 01.50	60 15 51.3	15.11	18045	2.51	20.31	19.10
	11	12 12 24.89	60 11 09.3	15.21	18348	3.38	21.09	19.86

and A1507 were measured by Ulrich (1978) and Huchra *et al.* (1990), respectively.

Our measured radial velocities for several galaxies that were not observed with the CCD array are listed in Table 3. Most of these galaxies are either field galaxies or cluster members of late morphological types (spiral and irregular). In addition to the cluster and galaxy numbers, Table 3 gives the heliocentric radial velocities of galaxies and an indication (column 4) of whether they belong to the foreground (fg) or background (bg) relative to the corresponding cluster. Coordinates of these galaxies can be found in Kopylov and Kopylova (2001).

DETERMINING THE DISTANCES AND PECULIAR VELOCITIES

The relation of Kormendy (1977) relates the effective radius R_e within which half of the light from the galaxy is contained to the effective surface brightness μ_e at this radius (or the mean effective surface brightness within this radius). Being the projection of the “fundamental plane,” which is specified by adding a third parameter: the central velocity dispersion of galaxy stars (Dressler *et al.* 1987; Djorgovski and Davis 1987), onto the plane specified by the photometrically determined parameters μ_e and $\log R_e$, Kormendy’s relation (KR) allows cluster distances to be estimated in a simpler way.

KR is

$$\mu_e = A \log R_e + C. \quad (1)$$

The free term in this relation (C) changes with distance. When using KR, the following assumptions are made: (1) KR is the same for all clusters; (2) all clusters are studied in their central parts, with the size of the selected region being $\approx 3 \times 3$ Mpc; and (3) a magnitude of $\approx -21.^m5$ is chosen as the limit, because galaxies fainter than this magnitude deviate greatly from KR.

Figure 2 shows a common $\mu_e - \log R_e$ diagram for our entire sample (434 galaxies from 39 clusters reduced to the same distance by applying cosmological corrections corresponding to our measured individual cluster distance to the measured magnitudes). Relativ-

Table 3. Additional radial velocities

Cluster	Galaxy	$V_{h,-1}$ km s ⁻¹	Background/ foreground	Cluster	Galaxy	$V_{h,-1}$ km s ⁻¹	Background/ foreground
Anon1	28	21568		A1318	66	22120	bg
"	38	21045		"	85	20756	bg
"	66	19957		"	97	17540	
"	94	21349		"	105	18760:	bg
Anon2	39	12 655	fg	A1377	22	14408	
Anon3	20	14240	fg	"	23	14332	
"	59	19930		"	76	14110	
"	60	8240	fg	"	88	15373	
"	73	11490	fg	"	107	23440	bg
Anon4	30	18796		"	112	23397	bg
"	34	18950:		"	113	14671	
Sh166	95	19350	bg	"	115	14874	
A1270	25	19930		"	124	14700	
"	93	20150		"	126	15507	
A1291	17	22070	bg	"	127	23364	bg
"	18	14850		"	161	14916	
"	31	21367:	bg	A1383	55	16972	
"	106	6101	fg	"	98	18613	
"	120	15109		A1436	30	18895	
"	132	15950		"	47	21515	bg
A1318	13	5574	fg	"	52	18860	
"	24	17543		"	73	20995	bg
"	40	5749	fg	"	100	18950	
"	54	17100					

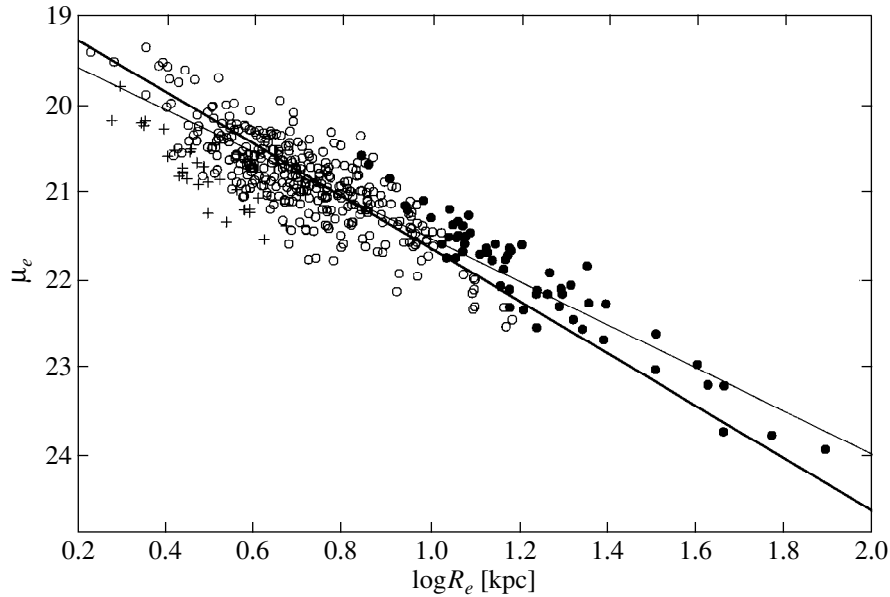


Fig. 2. The $(\log R_e - \mu_e)$ diagram for our 434 program galaxies. The filled circles, open circles, and crosses denote, respectively, galaxies brighter than $-23^m.5$, with $-21^m.5 < M_R < -23^m.5$, and fainter than $-21^m.5$. The straight lines represent the regression relations: direct (2) (thin line) and inverse (3) (heavy line). The cosmological corrections correspond to z_{spec} . The data were corrected for seeing.

istic effects and changes in the geometry of the Universe determine the correction $\delta\mu_e = 10 \log(1 + z_{\text{spec}})$, where z_{spec} is the measured redshift that includes the object's peculiar velocity. We denote the redshift corresponding to the actual cosmological distance by z_{phot} . We also applied the K correction [$K_R(z) = 1.1z$]. The angular size r_e was converted to the linear size R_e (in kpc). The galaxy parameters were corrected for seeing by the method described in Saglia *et al.* (1993). Thus, all data in Fig. 2 are shown in a comoving coordinate system for the “standard” cosmological model ($H_0 = 50 \text{ km s}^{-1} \text{ Mpc}^{-1}$, $q_0 = 0.5$). All the data shown in Fig. 2 were obtained at seeing $1''.1$ – $2''.0$. The thin line in Fig. 2 indicates the direct regression relation

$$\mu_e = 2.437(\pm 0.054) \log R_e + 18.976(\pm 0.266), \quad (2)$$

which was constructed by using 381 galaxies from our entire sample brighter than $-21^m.5$. The error in the free term is given per single galaxy.

The inverse relation (heavy line in Fig. 2) is

$$\log R_e = 0.3468(\pm 0.0080) \mu_e - 6.4588(\pm 0.100). \quad (3)$$

The rms scatter determined from the direct and inverse relations for the selected limit is equivalent to the error in the distance estimated from a single galaxy and is 25 and 23%, respectively (uncorrected for peculiar velocities). We see from the figure that galaxies brighter than $-23^m.5$ (filled circles) are better described by the direct regression (these are the brightest galaxies with one to three galaxies in each cluster). At the same time, as our determinations show, the error in the dis-

tance estimated from a single galaxy and the total formal error in the cluster distance are smaller than those inferred from the inverse regression, because most of the galaxies are fainter. To determine cluster distances, we took the mean coefficients between the direct and inverse regressions and derived KR in the final form

$$\log R_e = 0.3786 \mu_e - 7.123. \quad (4)$$

The coefficient and the free term depend on the selected limit. If we take a different magnitude limit, for example, $-22^m.0$, then the coefficients in the direct (2) and inverse (3) relations will be 2.555 and 0.338, respectively, while the errors in the distance estimated from a single galaxy will be 23 and 21%, respectively. In Fig. 2, galaxies fainter than $\sim -21^m.5$ (crosses) deviate from KR, as was previously noted by Capaccioli *et al.* (1992). Figure 3 shows KR for the Ursa Major supercluster (open circles) against the background of the complete sample.

Figure 4 illustrates the displacement of galaxies of individual clusters in the $\mu_e - \log R_e$ diagram from the mean regression relation (4) under the assumption that the cluster distances follow the Hubble law (the cosmological corrections were determined from z_{spec}). We did not use galaxies outside the 2.5σ range. They are marked by crosses in Fig. 4 and include galaxies 40 in A1270, 73, 74, and 85 in A1291, and 49 in Sh166. Three of them (40, 74, 49) are radio galaxies, 74 and 73 are interacting galaxies, and 85 is probably a background galaxy. In addition, the crosses mark galaxies within the 2.5σ range, but with different peculiarities: 51 in Anon3 and 27 and 24 in Sh166 are, respectively,

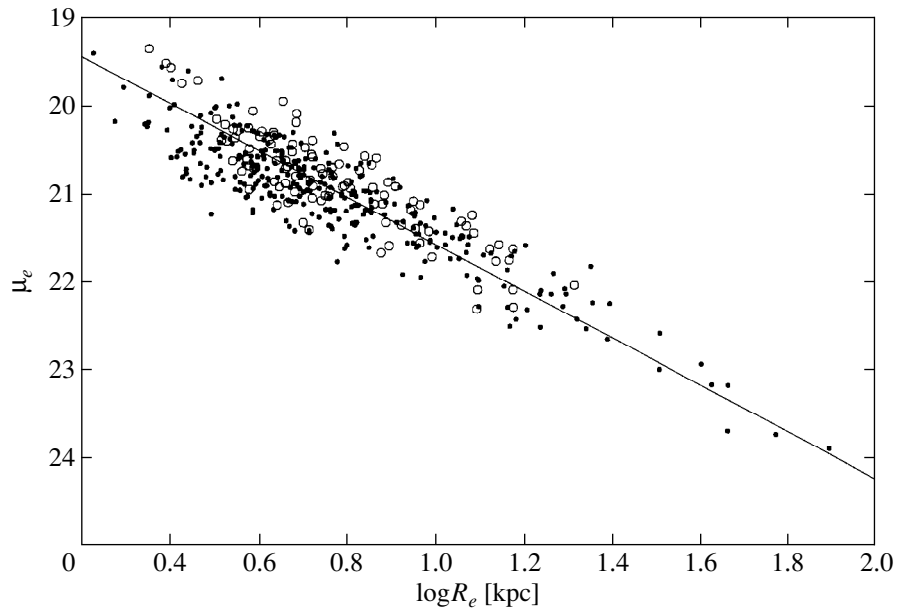


Fig. 3. The same as Fig. 2, but the galaxies belonging to the Ursa Major supercluster are indicated by open circles. The straight line represents the regression relation (4).

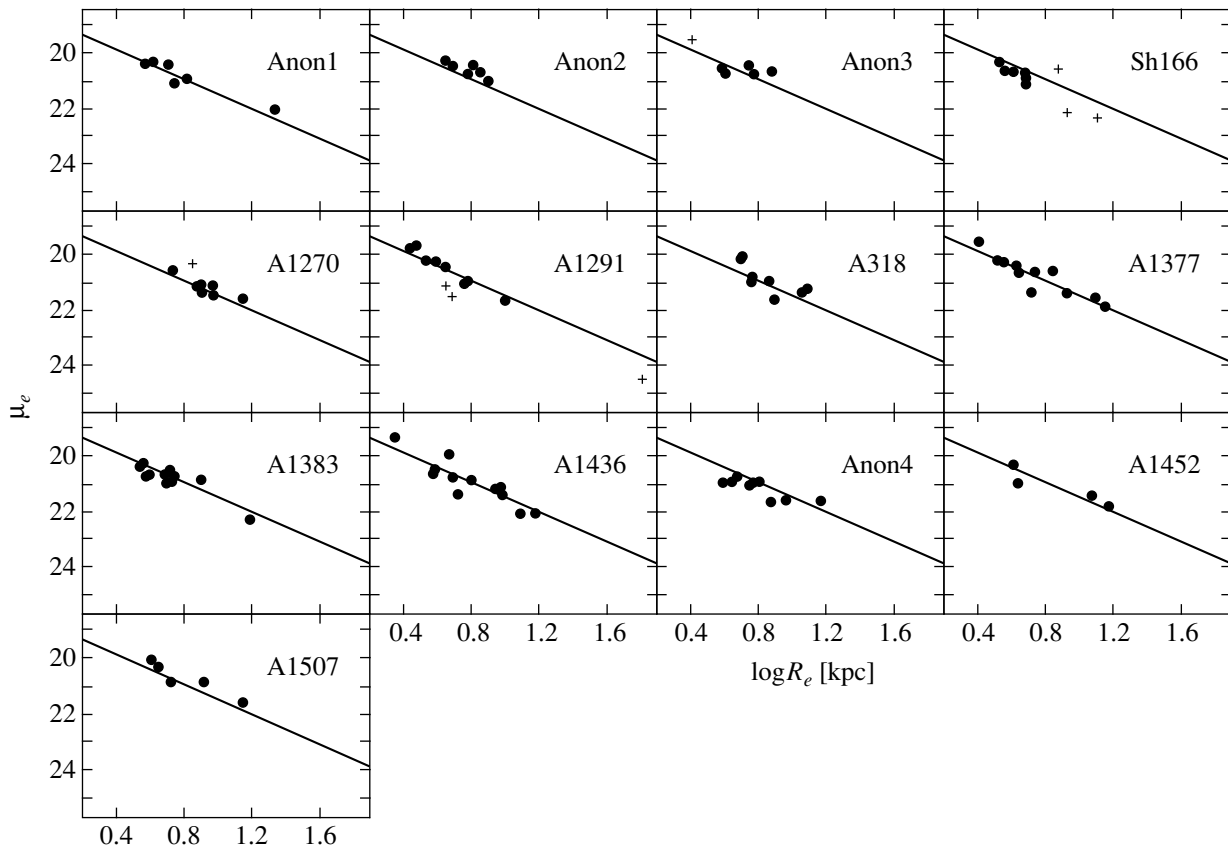


Fig. 4. Individual $(\log R_e - \mu_e)$ diagrams for 13 clusters in the Ursa Major supercluster. The straight line indicates the mean regression relation (4), which corresponds to the mean supercluster distance. The galaxies that were not involved in determining the cluster distances are marked by crosses. The cosmological corrections correspond to z_{spec} .

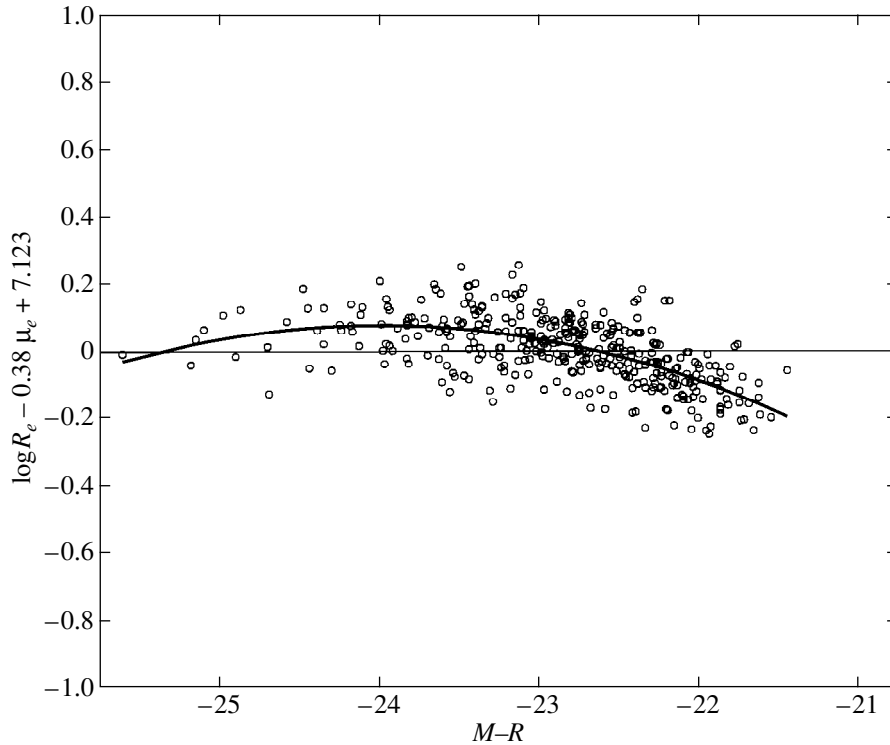


Fig. 5. Residuals from Kormendy's relation. The heavy line indicates the fit: $\log R_e - 0.3786\mu_e + 7.123 = 2.00M_R + 0.042M_R^2 + 23.95$.

a high-surface-brightness galaxy, an interacting galaxy, and a high-surface-brightness radio galaxy.

Since all cluster members are roughly at the same distance, we can perform averaging over several galaxies (from 5 to 20, depending on the cluster richness) and considerably increase the statistical accuracy of determining the distance to the cluster as a whole. To determine the distances for each of the clusters, we calculated the mean value of the free term in relation (4), $C_{\text{rms}} = \log R_e - 0.3786\mu_e$, which must be the same for all clusters when there are no deviations from the Hubble relation between velocity and distance.

The residuals from KR are defined as $\Delta = \log R_e - 0.3786\mu_e + 7.123$, and, consequently, the measured distances depend on the galaxy magnitude. This makes the method of determining distances in question sensitive to sample incompleteness (generally at faint magnitudes), which was also pointed out by Scodggio *et al.* (1997). Figure 5 shows this effect, and it may be noted that this relation is nearly quadratic. In order to reduce the sensitivity to sample incompleteness, we fitted the relation in Fig. 5 by a second-degree polynomial:

$$\log R_e - 0.3786\mu_e + 7.123 = a_1M_R + a_2M_R^2 + a_3. \quad (5)$$

We obtained the following coefficients: $a_1 = -2.001820$, $a_2 = -0.041696$, $a_3 = -23.949609$. The rms deviation of the regression is 0.081. The mean statistical error in C_{rms} when averaged over 5 to 14 cluster galaxies is 0.033 (8%) and 0.026 (6%) without and with allowance for the galaxy magnitude, respectively. The derived C_{rms}

for each cluster was used to determine the deviation from the mean supercluster distance C_{mean} and to calculate the photometric redshift

$$z_{\text{phot}} = z_{\text{spec}} \times 10^{C_{\text{mean}} - C_{\text{rms}}}, \quad (6)$$

i.e., the redshift that corresponds to the cosmological distance of the cluster when there is no peculiar velocity caused by gravitational interaction in the supercluster.

Table 4 contains the following data: Abell cluster numbers; the number of galaxies with measured photometric parameters; mean relative distances with their errors; z_{spec} and z_{phot} determined from the redshift and the photometric distance, respectively; peculiar cluster velocities relative to the supercluster centroid, which were calculated from the formula

$$V_{\text{pec}} = (cz_{\text{spec}} - cz_{\text{phot}})/(1 + z_{\text{phot}}) \quad (7)$$

and their errors δV_{pec} .

The Hubble diagram for the Ursa Major supercluster that corresponds to Table 4 is shown in Fig. 6. An analysis of this figure leads us to the following conclusions. In general, the supercluster obeys the Hubble relation between radial velocity and distance. However, there is a significant gap at $z_{\text{phot}} \sim 0.06$ that separates the supercluster into two subsystems composed of five and eight clusters with mean radial velocities of 16 200 and 19 700 km s⁻¹. The statistical significance of this separation is rather low, because the gap is comparable with the distance measurement error and is determined by the distance estimates for a mere two or three clusters

Table 4. Peculiar velocities in the Ursa Major supercluster

Cluster	N	C_{cl}	z_{spec}	z_{phot}	V_{pec}	δV_{pec}
A1377	11	-7.106 ± 0.033	0.0507	0.0505	53	± 1140
Sh166	6	-7.137 ± 0.015	0.0512	0.0548	-1023	± 570
A1291	8	-7.104 ± 0.039	0.0550	0.0546	124	± 1500
A1318	8	-7.103 ± 0.035	0.0572	0.0566	170	± 1380
A1507	5	-7.059 ± 0.024	0.0592	0.0530	1768	± 900
A1383	10	-7.127 ± 0.019	0.0603	0.0631	-787	± 840
Anon4	9	-7.168 ± 0.023	0.0614	0.0705	-2583	± 1260
A1452	4	-7.107 ± 0.031	0.0631	0.0630	25	± 1350
A1436	12	-7.117 ± 0.036	0.0642	0.0656	-387	± 1620
Anon3	7	-7.080 ± 0.029	0.0683	0.0641	1190	± 1140
A1270	6	-7.119 ± 0.020	0.0689	0.0707	-502	± 990
Anon1	7	-7.113 ± 0.022	0.0699	0.0708	-242	± 1080
Anon2	5	-7.059 ± 0.016	0.0703	0.0629	2080	± 690

with $z_{spec} \sim 0.06$. If the subsystems are real, then, for a velocity dispersion of $\sim 1100 \text{ km s}^{-1}$ in each of them, each of the subsystems may be gravitationally bound. Judging by the deviation of the subsystem centroids from the Hubble relation, the interaction between them appears to be insignificant.

Note that the five poorest clusters (Kopylov and Kopylova 2001)—Anon2, Anon3, Anon4, Sh166, and A1507—exhibit the largest peculiar velocities. In these cases, the derived peculiar velocities may be affected by an age difference between the stellar populations of galaxies in poor and rich galaxies (Jörgensen and Jönch-Sorensen 1998).

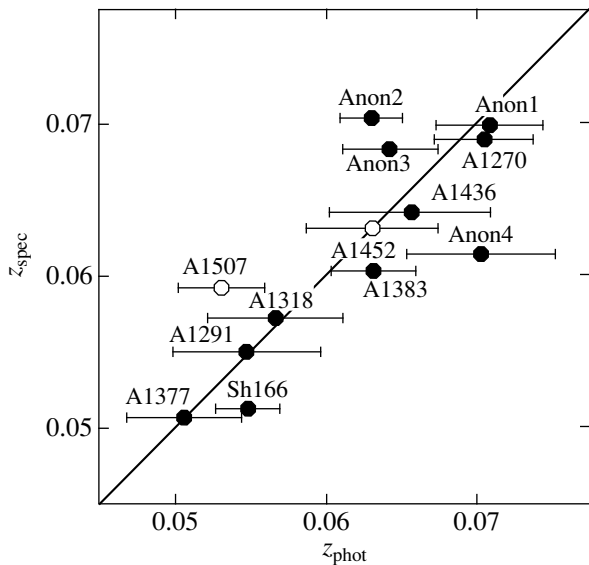


Fig. 6. The Hubble diagram for the Ursa Major supercluster. The errors correspond to the error in the mean cluster distance. The two clusters lying aside (in projection onto the sky) are marked by open circles.

CONCLUSION

We have obtained photometric parameters (m_R , μ_e , $\log r_e$) of 107 galaxies (CCD measurements virtually for all galaxies and spectroscopic measurements for 90% of the galaxies have been made for the first time) in the R_c band for 13 clusters of the Ursa Major supercluster. We have also estimated for the first time the relative distances and peculiar velocities in this supercluster using Kormendy's relation by taking into account the dependence of residuals from KR on the galaxy absolute magnitude. The photometrically measured cluster distances allowed us to estimate the dynamical state of the supercluster more accurately and to determine the peculiar velocity field within it.

The strong correlation between distance and velocity leads us to conclude that the Hubble expansion law holds, within the limits of the measurement errors, for the Ursa Major supercluster (Fig. 6). The apparent compactness of the Ursa Major supercluster in the sky results from a chance line-of-sight projection of an elongated supercluster, which may consist of two subsystems. However, even in this case, the volume density contrast for the supercluster is high (~ 7). This provides evidence that the supercluster is actually a physically isolated system rather than a chance association of clusters.

REFERENCES

1. G. O. Abell, H. G. Corwin, Jr., and R. P. Olowin, *Astrophys. J., Suppl. Ser.* **70**, 1 (1989).
2. V. L. Afanas'ev, V. A. Lipovetskiĭ, V. P. Mikhaĭlov, *et al.*, *Otchet SAO*, No. 138 (1986).
3. F. W. Baier, *Astron. Nachr.* **301**, 17 (1980).
4. M. Capaccioli, N. Caon, and M. D'Onofrio, *Mon. Not. R. Astron. Soc.* **259**, 323 (1992).
5. S. Djorgovski and M. Davis, *Astrophys. J.* **313**, 59 (1987).

6. S. V. Drabek, I. M. Kopylov, N. N. Somov, and T. A. Somova, *Astrofiz. Issled.* **22**, 64 (1986).
7. A. Dressler, *Astrophys. J., Suppl. Ser.* **42**, 565 (1980).
8. A. Dressler, D. Lynden-Bell, D. Burstein, *et al.*, *Astrophys. J.* **313**, 42 (1987).
9. Ts. B. Georgiev, *Izv. SAO* **33**, 213 (1991).
10. P. Grosbol, in *Reviews in Modern Astronomy*, Ed. by Q. Klark (Springer-Verlag, Berlin, 1989), Vol. 2, p. 242.
11. J. P. Huchra, J. P. Henry, M. Postman, and M. J. Geller, *Astrophys. J.* **365**, 66 (1990).
12. M. L. Humason, N. U. Mayall, and A. R. Sandage, *Astron. J.* **61**, 97 (1956).
13. I. Jørgensen and H. Jönch-Sørensen, *Mon. Not. R. Astron. Soc.* **297**, 968 (1998).
14. A. I. Kopylov and F. G. Kopylova, *Bull. Spec. Astrophys. Obs.* **39**, 44 (1996).
15. A. I. Kopylov and F. G. Kopylova, *Bull. Spec. Astrophys. Obs.* **45**, 66 (1998).
16. A. I. Kopylov and F. G. Kopylova, *Pis'ma Astron. Zh.* **27**, 170 (2001) [*Astron. Lett.* **27**, 140 (2001)].
17. F. G. Kopylova and A. I. Kopylov, *Pis'ma Astron. Zh.* **24**, 573 (1998) [*Astron. Lett.* **24**, 491 (1998)].
18. J. Kormendy, *Astrophys. J.* **218**, 333 (1977).
19. A. U. Landolt, *Astron. J.* **104**, 340 (1992).
20. H. J. Rood, *Mon. Not. R. Astron. Soc.* **254**, 67 (1992).
21. R. P. Saglia, E. Bertschinger, G. Baggley, *et al.*, *Mon. Not. R. Astron. Soc.* **264**, 961 (1993).
22. M. Scodeggio, R. Giovanelli, and M. Haynes, *Astron. J.* **113**, 2087 (1997).
23. S. A. Shectman, *Astrophys. J., Suppl. Ser.* **57**, 77 (1985).
24. R. R. Treffers and M. W. Richmond, *Publ. Astron. Soc. Pac.* **101**, 725 (1989).
25. M.-H. Ulrich, *Astrophys. J.* **221**, 422 (1978).
26. G. de Vaucouleurs, *Ann. Astrophys.* **11**, 247 (1948).

Translated by V. Astakhov

Type Ia Supernovae: An Explosion in the Regime of a Convergent Delayed Detonation Wave

N. V. Dunina-Barkovskaya, V. S. Imshennik*, and S. I. Blinnikov

Institute for Theoretical and Experimental Physics, ul. Bol'shaya Cheremushkinskaya 25, Moscow, 117259 Russia
Max-Planck-Institut fuer Astrophysik, Karl Schwarzschild Strasse 1, 86740 Garching bei Muenchen, Germany

Received December 25, 2000

Abstract—The model of a presupernova's carbon–oxygen (C–O) core with an initial mass of $1.33M_{\odot}$, an initial carbon abundance $X_C^{(0)} = 0.27$, and a mean rate of increase in mass of $5 \times 10^{-7} M_{\odot} \text{ yr}^{-1}$ through accretion in a binary system evolved from the central density and temperature $\rho_c = 10^9 \text{ g cm}^{-3}$ and $T_c = 2.05 \times 10^8 \text{ K}$, respectively, by forming a convective core and its subsequent expansion to an explosive fuel ignition at the center. The evolution and explosion equations included only the carbon burning reaction $^{12}\text{C} + ^{12}\text{C}$ with energy release corresponding to the complete conversion of carbon and oxygen (at the same rate as that of carbon) into ^{56}Ni . The ratio of mixing length to convection-zone size α_c was chosen as the parameter. Although the model assumptions were crude, we obtained an acceptable (for the theory of supernovae) pattern of explosion with a strong dependence of its duration on α_c . In our calculations with sufficiently large values of this parameter, $\alpha_c = 4.0 \times 10^{-3}$ and 3.0×10^{-3} , fuel burned in the regime of prompt detonation. In the range $2.0 \times 10^{-3} \geq \alpha_c \geq 3.0 \times 10^{-4}$, there was initially a deflagration with the generation of model pulsations whose amplitude gradually increased. Eventually, the detonation regime of burning arose, which was triggered from the model surface layers (with $m \approx 1.33M_{\odot}$) and propagated deep into the model up to the deflagration front. The generation of model pulsations and the formation of a detonation front are described in detail for $\alpha_c = 1.0 \times 10^{-3}$. © 2001 MAIK “Nauka/Interperiodica”.

Key words: *supernovae and supernova remnants; plasma astrophysics, hydrodynamics, and shock waves; detonation and deflagration*

INTRODUCTION

The evolution of a degenerate stellar C–O core with a mass close to the Chandrasekhar limit of $1.43M_{\odot}$ for a carbon white dwarf (see, Bisnovatyĭ-Kogan 1989) leads to the growth of thermal instability and an explosion. The critical central density $\rho_{c, \text{cr}}$ at which an explosion begins can take on values from $\sim 2 \times 10^9$ to $\sim 10^{10} \text{ g cm}^{-3}$. It grows with decreasing rate of increase in core mass \dot{M} , which is given by the Paczyński–Uus relation (Paczyński 1970) in a single asymptotic-giant-branch (AGB) star:

$$\dot{M} = 6 \times 10^{-7} (M/M_{\odot} - 0.5) M_{\odot} \text{ year}^{-1}, \quad (1)$$

and can take on values from 10^{-8} to $5 \times 10^{-7} M_{\odot}$ in an accreting white dwarf (Iben 1982; Hachisu *et al.* 1996). Here, we chose $\dot{M} = 5 \times 10^{-7} M_{\odot}$, which may corre-

spond both to a single AGB star and to a component of a binary system.

Explosion calculations, including those with convection, have been performed repeatedly (Arnett 1969; Ivanova *et al.* 1974; Nomoto *et al.* 1976; see also the review by Niemeyer and Woosley 1997). In Ivanova *et al.* (1974), carbon burned in the deflagration regime with the generation of pulsations, but these authors ignored convection at the supernova stage and obtained the initial temperature profile by estimating the contribution of convection rather than evolutionarily.

Woosley (1997) performed a series of one-dimensional explosion calculations for accreting white dwarfs (unfortunately, this author gave no accretion rates) with critical central densities from 2×10^9 to $8.2 \times 10^9 \text{ g cm}^{-3}$ and with the inclusion of nucleosynthesis for 442 isotopes. However, he considered only adiabatic convection at the presupernova stage, with convection being artificially turned off (because maintaining an adiabatic temperature gradient in his model any further would result in a prompt detonation) at the onset of a thermal flash (at $T_c = 7 \times 10^8 \text{ K}$). The burning-

* E-mail address for contacts: imshennik@vxitep.itep.ru

front velocity was determined as prescribed by Woosley and Timmes (1992) by taking into account the fractal dimension of the front.

BASIC EQUATIONS FOR A CONVECTIVE HYDRODYNAMIC MODEL

When calculating the evolution of a presupernova (on time scales of $\sim 10^4$ years), most authors (see, e.g., Iben 1982) use a hydrostatic system of equations with adiabatic convection in the stellar core, which is justifiable at this stage but can be too crude for a transition to an explosion. Here, based on the hydrodynamic model previously developed by Blinnikov and Rudzskii (1984), Blinnikov and Bartunov (1993), and Blinnikov and Dunina-Barkovskaya (1993, 1994), we performed calculations both at the presupernova stage and at the stage of explosive burning. In the latter two papers, this hydrodynamic model was used to calculate the evolution of white dwarfs. Our equations also included non-adiabatic unsteady convection in the standard mixing-length approximation:

$$\frac{\partial r}{\partial t} = v, \quad (2)$$

$$\frac{\partial v}{\partial t} = -\frac{Gm}{r^2} - 4\pi r^2 \frac{\partial P}{\partial m}, \quad (3)$$

$$\frac{\partial T}{\partial t} = \left[\varepsilon_{\text{CC}} + \varepsilon_{\nu} - 4\pi \frac{\partial(r^2 F_{\text{conv}})}{\partial m} - 4\pi \frac{\partial(r^2 F_{\text{rad}})}{\partial m} + \varepsilon_{\text{g}} \right] / \left(\frac{\partial E}{\partial T} \right)_{\rho}, \quad (4)$$

$$\frac{\partial X_{\text{C}}}{\partial t} = -X_{\text{C}}^2 r_{\text{CC}} + \left(\frac{\partial X_{\text{C}}}{\partial t} \right)_{\text{conv}}, \quad (5)$$

$$\frac{\partial u_{\text{c}}}{\partial t} = \frac{2(v_{\text{c}}^2 - u_{\text{c}}^2)}{l_{\text{mix}}}, \quad (6)$$

where X_{C} is the mass fraction of ^{12}C , ε_{CC} is the energy release through carbon burning, ε_{ν} are the standard neutrino energy losses [calculated from the formulas of Schinder *et al.* (1987); see also Haft *et al.* (1994)], ε_{g} is the energy release through gravitational contraction, F_{rad} is the radiative energy flux, F_{conv} is the convective energy flux, u_{c} is the velocity of unsteady convection, and v_{c} is the velocity of steady convection in the mixing-length approximation calculated from the following formula (see, e.g., Bisnovatyĭ-Kogan 1989):

$$v_{\text{c}} = \left(g \left(\frac{\partial \ln \rho}{\partial r} - \left(\frac{\partial \ln \rho}{\partial r} \right)_{\text{s}} \right) \right)^{1/2} l_{\text{mix}}. \quad (7)$$

The convective energy flux F_{conv} and the quantity $(\partial X_{\text{C}}/\partial t)_{\text{conv}}$, which is equal to the change in carbon

mass fraction X_{C} through convection, were calculated by using the formulas

$$F_{\text{conv}} = \left(\left(\frac{\partial T}{\partial r} \right)_{\text{s}} - \frac{\partial T}{\partial r} \right) \frac{c_{\text{P}} \rho u_{\text{c}} l_{\text{mix}}}{2}, \quad (8)$$

$$\left(\frac{\partial X_{\text{C}}}{\partial t} \right)_{\text{conv}} = \frac{1}{r^2} \frac{\partial}{\partial r} \left(r^2 l_{\text{mix}} u_{\text{c}} \frac{\partial X_{\text{C}}}{\partial r} \right). \quad (9)$$

The arrangement and sizes of (generally several) convection zones are determined by the Schwarzschild criterion [in accordance with Eqs. (7) and (8)]. Unsteady convection was disregarded at the presupernova stage, while Eqs. (8) and (9) included v_{c} from Eq. (7) instead of u_{c} . The calculations with steady and unsteady convection at the presupernova stage are compared in Dunina-Barkovskaya and Imshennik (2000).

The mixing length in the i th mass zone, $l_{\text{mix}}^{(i)}$, is given by

$$l_{\text{mix}}^{(i)} = \min \left(\alpha_{\text{p}} \left(\frac{\partial |\ln P|}{\partial r} \right)_i^{-1}, \alpha_{\text{c}} \Delta r_{\text{c}} \right), \quad (10)$$

where Δr_{c} is the size of the convection zone that includes the i th zone, and α_{p} was taken to be unity in our calculations.

Thermodynamic quantities (pressure P , entropy S , etc.) were calculated for an electron-positron gas by using Nadyozhin's asymptotics described in Blinnikov *et al.* (1996) and for an ion gas with screening by using the formulas of Yakovlev and Shalybkov (1988).

INITIAL AND BOUNDARY CONDITIONS. CALCULATIONS AT THE PRESUPERNOVA STAGE

It is appropriate to choose the initial state of a presupernova's C–O core from reliable evolution calculations. We began our calculation with the central density $\rho_{\text{c}} = 10^9 \text{ g cm}^{-3}$. At this density, the central temperature must be approximately equal to $T_{\text{c}}^{(0)} = 2.05 \times 10^8 \text{ K}$, as follows from the calculations of Iben (1982). Below, by the onset of explosion and, accordingly, by the end of the presupernova stage, we arbitrarily mean the instant in time when the temperature in the central mass zone reaches $5 \times 10^9 \text{ K}$.

The initial carbon mass fraction $X_{\text{C}}^{(0)} = 0.27$ (constant throughout the C–O core) was chosen to be the same as that in Iben (1982). With the above central parameters of the C–O core and with a total mass of $1.33 M_{\odot}$, we calculated a hydrostatically equilibrium adiabatic configuration, which was used below as the initial condition. Note that its deviation from the model of Iben (1982) is most likely insignificant.

When calculating the evolution of this model with a constant mass accretion rate of $5 \times 10^{-7} M_{\odot} \text{ yr}^{-1}$, which may be typical of accreting white dwarfs in binary systems (see above), it makes sense to specify a nonzero

external boundary condition for the pressure. Previously (Dunina-Barkovskaya and Imshennik 2000), we included the entire accreted mass in the external boundary condition for the relatively small changes in total mass before the onset of explosion confirmed by calculations.

This condition can be straightforwardly derived in the approximation of a thin ($\Delta R/R \ll 1$), light ($\Delta M/M \ll 1$) envelope. Indeed, integrating the equation of hydrostatic equilibrium

$$-\frac{dP}{dm} = \frac{Gm}{4\pi r^4}$$

over the envelope thickness yields an expression for the pressure P_b at the outer boundary of the zone with Lagrangian coordinate M :

$$P_b(M) = \frac{G}{4\pi} \int_M^{M+\Delta M} \frac{mdm}{r^4} \approx \frac{G}{8\pi R^4} (m^2)_M^{M+\Delta M} \quad (11)$$

$$\approx \frac{GM}{4\pi R^4} \Delta M,$$

where $\Delta M = \dot{M}t$ and $R = R(t)$ during the hydrostatic evolution; i.e., the external pressure P_b (11) increases through accretion with time t measured from the initial time of the C–O core calculation. In this case, the total mass $M_N + \Delta M$ (where M_N is the mass of N Lagrangian zones included in the hydrodynamic model) increased to $\sim 1.351M_\odot$; accordingly, the evolution time is 4.25×10^4 years (Dunina-Barkovskaya and Imshennik 2000).

Here [by analogy with Woosley (1997)], we gradually, in the course of accretion, added new Lagrangian zones to the model; their mass decreased in geometric progression from $7.83 \times 10^{-3}M_\odot$ (zone no. 151) to $7.50 \times 10^{-5}M_\odot$ (the last zone no. 170). The equality (11) was found to be inaccurate (clearly because $\Delta R/R$ was not small enough), and, as a result, the evolution time at the presupernova stage almost doubled. For our calculations with nonzero α_c , the model mass reached $1.3658M_\odot$ in $t \approx 7.2 \times 10^4$ years, and the number of Lagrangian zones was $N = 170$. Subsequently, we added no Lagrangian zones and modeled the accretion by increasing the boundary pressure. At the time of explosion ($t \approx 7.9 \times 10^4$ years after the beginning of our calculations), the boundary pressure corresponded to an additional external mass from $2.316 \times 10^{-3}M_\odot$ (for $\alpha_c = 3.0 \times 10^{-4}$) to $2.342 \times 10^{-3}M_\odot$ (for $\alpha_c = 4.0 \times 10^{-3}$). In the check calculation with $\alpha_c = 0$, the temperature in the central zone rose to 5×10^9 K in 6.789×10^4 years; therefore, the model mass had time to increase only to $1.3636M_\odot$, which corresponded to the number of zones $N = 161$.

Let us consider the boundary condition (11) during an explosion for the calculation with $\alpha_c = 1.0 \times 10^{-3}$ when $\Delta M = 2.338 \times 10^{-3}M_\odot$ and $R_0 = 1.85 \times 10^8$ cm (see Fig. 1):

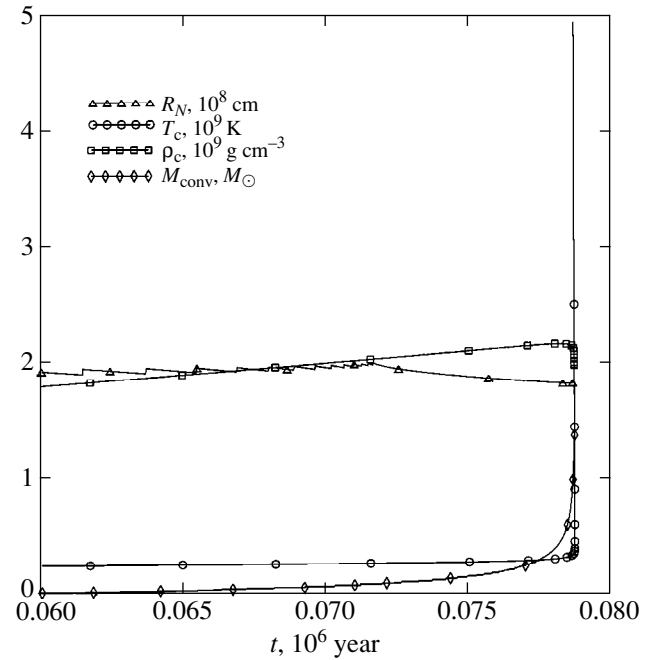


Fig. 1. The evolution of a presupernova after the formation of a convective core: central temperature T_c , central density ρ_c , convective-core mass M_{conv} , and radius R_N of the last (N th) mass zone versus time for $\alpha_c = 1.0 \times 10^{-3}$.

$$P_b(1.33M_\odot) = P_0 \left(\frac{R_0}{R} \right)^4, \quad (12)$$

where $P_0 = 5.72 \times 10^{22}$ dynes cm^{-2} . This value should be compared with the central density of a C–O core, which has the standard lower limit, $P_c(0) > GM^2/(8\pi R^4)$. The boundary-to-central pressure ratio, $P_b(M)/P_c(0) < 2\Delta M/M = 3.42 \times 10^{-3}$, is then definitely small at the onset of explosion. Subsequently, it certainly changes and can increase several-fold when pulsations emerge, but it still remains small enough, as we see from this calculation.

It is easy to estimate that the relative contribution of the inertial term to the boundary condition (12) with characteristic pulsation parameters of a C–O core ($4v_p/\tau_p$)($R_0^2/(GM)$) is minor, no more than a few percent. This justifies ignoring this term in Eq. (11) even for the largest pulsation amplitude $\Delta R \approx R_0$ and $\tau_p \approx 5$ s by the end of deflagration (see Fig. 4). The close match between this boundary condition attributable to mass accretion onto the surface of a C–O core and the external boundary condition assumed previously (Ivanova *et al.* 1974, 1977a) is lucky: with the same dependence on outer radius R , $P_b(M) \propto R^{-4}$ (Eq. (12)). Recall that in the cited papers, this external pressure simulated the presence of an outer envelope of the stellar C–O core, and it was taken to be small enough, approximately twice the value of Eq. (12). Thus, the effect of the external boundary condition in the above papers was more pronounced than here, but less pronounced than in

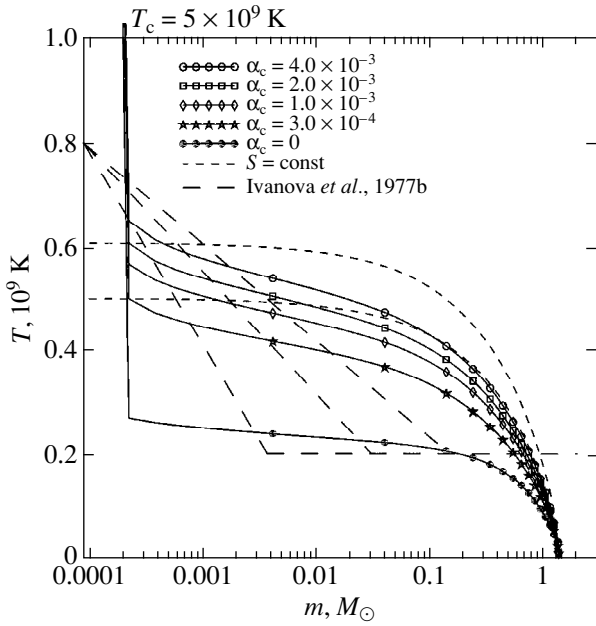


Fig. 2. Temperature profiles at the onset of supernova explosion (at the times when the central temperature reaches 5×10^9 K) for various α_c .

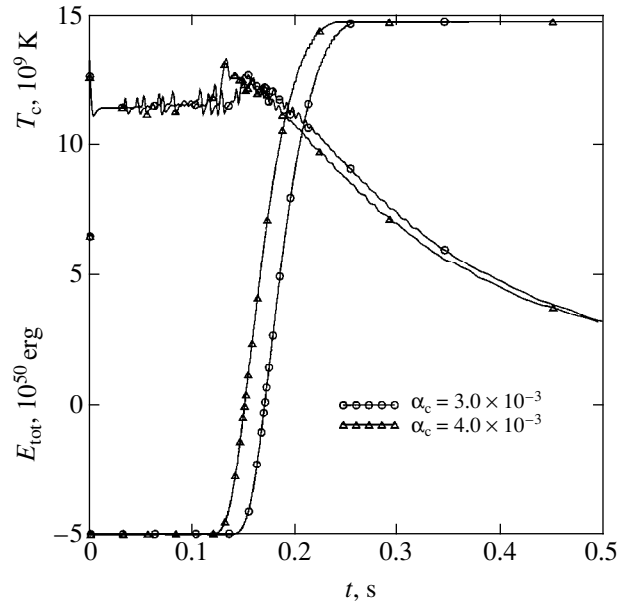


Fig. 3. Central temperature T_c and total energy E_{tot} of a C–O core versus time for $\alpha_c = 4.0 \times 10^{-3}$ and 3.0×10^{-3} (rapid detonation).

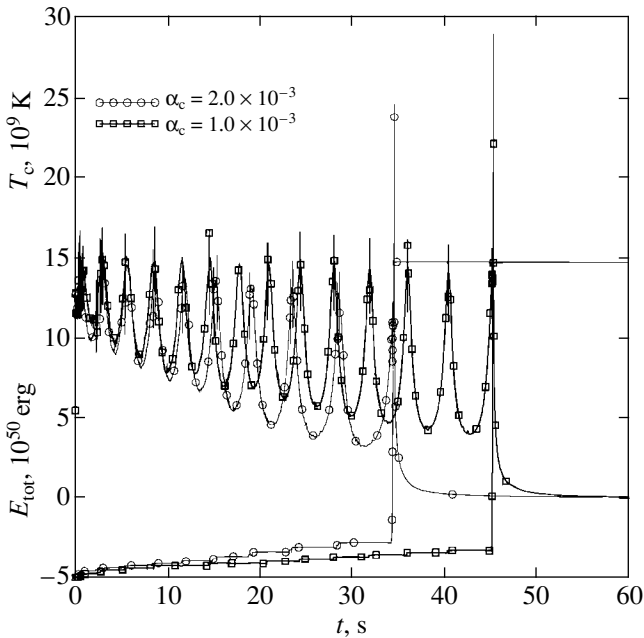


Fig. 4. The same as Fig. 3 for $\alpha_c = 2.0 \times 10^{-3}$ and 1.0×10^{-3} (pulsational deflagration with delayed detonation).

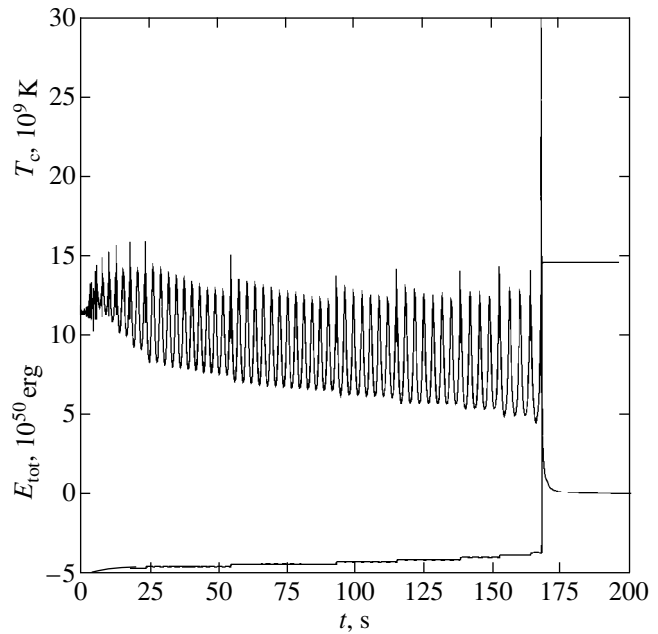


Fig. 5. The same as Fig. 3 for $\alpha_c = 3.0 \times 10^{-4}$ (deflagration-pulsational regime with delayed detonation).

Dunina-Barkovskaya and Imshennik (2000). It should also be noted that the presence of an external pressure, $P_b(M) \neq 0$, violates the energy conservation law during an explosion (see Figs. 4, 5) when pulsations emerge and when the radius of the C–O core R changes. Naturally, allowance for the accreted matter in the external boundary condition (11) and (12) implies its addition to

the evolving C–O core without any additional energy release, i.e., simply adhesion. In reality, this matter, which generally has a different chemical composition, can experience thermonuclear reactions with energy release and even with the partial outward ejection of accreted matter. Of course, we ignore such processes. On the other hand, the external boundary condition (12)

plays a crucial role during an explosion, especially during the formation of a detonation wave from the surface (see below).

DISCUSSION

Here, we systematically and numerically analyzed models with various values of α_c in the mixing length (10): 4.0×10^{-3} , 3.0×10^{-3} , 2.0×10^{-3} , 1.0×10^{-3} , and 3.0×10^{-4} . From a physical point of view, it is difficult to prefer any α_c from this wide range in the approximate theory of nonadiabatic convection we use. The energy release in the thermonuclear reaction of carbon burning, $^{12}\text{C} + ^{12}\text{C} \rightarrow ^{24}\text{Mg} + \gamma$, was taken, first, from the crude formula derived by Fowler and Hoyle (1965) with the electron screening factor from Salpeter (1954) (see also Salpeter and Van Horn 1969; Arnett 1969) and, second, with the maximum possible energy release of burning corresponding to instantaneous burning of the entire carbon-oxygen mixture up to ^{56}Ni . The energy release used here was taken from Ivanova *et al.* (1974), but with a correction for the presence of oxygen in the fuel. It is convenient for the subsequent comparison of all previous calculations with those performed here. This simplification of thermonuclear energy release cannot significantly affect our results, because the ignition conditions for a C–O mixture are only slightly sensitive to all pre-exponential quantities in the expression for the rate of thermonuclear burning.

Our calculations of a presupernova's evolution revealed that the density slightly decreased immediately before the onset of explosion; this decrease depended nonmonotonically on α_c and was at a maximum for $\alpha_c = 4.0 \times 10^{-3}$. The initial critical central density, $\rho_{c,cr,9} \approx (1.88\text{--}2.03)$ (in units of 10^9 g cm^{-3}) proves to be close to that taken by Ivanova *et al.* (1974, 1977a) ($\rho_{c,9} = 2.33$) as the initial one, although it is slightly lower. Recall that at that time, the view of the evolution of intermediate-mass single stars along the convergent track of Paczyński (1970) after the formation of a carbon (or carbon-oxygen) core was most popular. The current interpretation of presupernovae suggests their evolution in a close binary system with an accreting white dwarf. In this case, according to Yungelson (1998), all main-sequence stars with masses in the range $2.5 \leq M/M_\odot \leq 10$, which differs only slightly from the same range for previously considered single stars, $3.5 \leq M/M_\odot \leq 8$ (Paczyński 1970), can become carbon-oxygen white dwarfs in close binary systems.

Figure 1 shows some of the quantities that characterize a stellar C–O core before the onset of explosion: mass M_{conv} of the convective core, central temperature T_c , central density ρ_c , and radius R_N of the C–O core in the evolution time from 6×10^4 years (the beginning of the C–O core formation) to 7.87×10^4 years for $\alpha_c = 1.0 \times 10^{-3}$. The small jumps in radius R_N of the last (N th) mass zone (see Fig. 2) clearly demonstrate the above procedure of adding new Lagrangian zones. The phase

of the star's slow expansion before its explosion (see above) is barely noticeable in this figure, because its duration ($\sim 3 \times 10^2$ years) is short compared to the total evolution time (during which the star slowly contracted) and is virtually independent of α_c . By the onset of explosion, convection encompasses the entire C–O core; i.e., $M_{\text{conv}} = 1.3658M_\odot$ for all the values of $\alpha_c \neq 0$ considered. In the immediate vicinity of $\alpha_c = 0$, the development of the convective core is incomplete—it does not reach the C–O core surface, and no explosion occurs (see below).

Figure 2 shows temperature profiles as a function of mass coordinate at the time of explosion onset corresponding to the specified α_c (see above). The temperature for the calculations with convection is seen to be appreciably higher within the convective core than that for the calculation without convection. Even at $\alpha_c = 3.0 \times 10^{-4}$, the temperature is twice as high as this value in the central part of the convective core. For comparison, Fig. 2 shows approximate temperature profiles from Ivanova *et al.* (1977b); an explosion developed for two (upper) profiles. It therefore comes as no surprise that in this calculation, the explosion developed into the complete destruction of the entire star for all $\alpha_c \geq 3.0 \times 10^{-4}$ (see below). For the calculations with $\alpha_c = 2.0 \times 10^{-3}$ and 3.0×10^{-4} , which constrain pulsational deflagration (see below), the figure also shows adiabatic temperature profiles with an entropy equal to the entropy of the second mass zone for each calculation. We see that our profiles lie well below the corresponding adiabatic profiles and have a different shape at $m < 0.1M_\odot$, which, clearly, affects the development of an explosion with the absence of spontaneous burning (Blinnikov and Khokhlov 1986).

Interestingly, the smooth temperature profile in the second mass zone (with $m = 2.24 \times 10^{-4}M_\odot$) at the largest $\alpha_c = 4.0 \times 10^{-3}$ touches the third steep profile, for which no explosion developed in the calculations of Ivanova *et al.* (1977b). By contrast, the initial temperature profile for the calculation with the smallest $\alpha_c = 3.0 \times 10^{-4}$, which barely exploded (see Fig. 5), lies well below the third profile from Ivanova *et al.* (1977b) at $m < 7 \times 10^{-4}M_\odot$ (in the first four mass zones). In general, it may be assumed that there is qualitative agreement between our results and the calculations of Ivanova *et al.* (1977b).

The explosion develops differently for $\alpha_c \geq 3.0 \times 10^{-3}$ (Fig. 3) and $\alpha_c \leq 2.0 \times 10^{-3}$ (Fig. 4). In these figures, the central temperature T_c and total energy E_{tot} of a C–O core are plotted against time. The latter is eventually equal to $\sim 1.5 \times 10^{51}$ erg, which corresponds to complete burning up to ^{56}Ni in all calculations, irrespective of α_c . E_{tot} at the onset of explosion ($\sim 4.3 \times 10^{50}$ erg) is also virtually the same in these calculations.

The main result of our numerical calculations should be considered to be the emergence of a deflagration-pulsational regime at a sufficiently small mixing length, $\alpha_c \leq 2.0 \times 10^{-3}$. We found a rapid detonation to

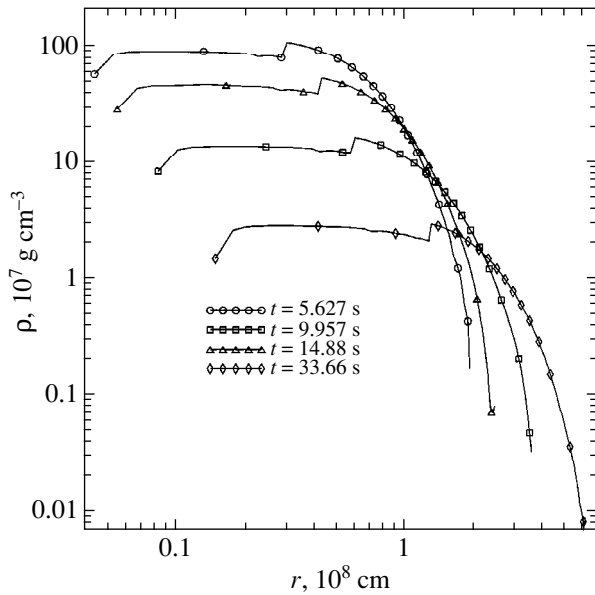


Fig. 6. Density versus radius for $\alpha_c = 1.0 \times 10^{-3}$ (pulsational deflagration).

take place at $\alpha_c \geq 3.0 \times 10^{-3}$ (see Fig. 3). Thus, we determined an accurate boundary of the transition from a rapid detonation to a pulsational deflagration.

Figure 4 shows ten and fourteen pulsations in the calculations with $\alpha_c = 2.0 \times 10^{-3}$ and 1.0×10^{-3} , respectively. In both cases, the burning ends with a powerful energy release in the last pulsation, with the burning regime changing abruptly. Whereas the burning in previous pulsations was in the deflagration regime, in the last pulsation the remaining mass of unburned fuel (about 90%) burns in the detonation regime. T_c reaches its maximum value of $(2.5\text{--}2.9) \times 10^{10}$ K slightly later, immediately after a collision of the detonation front propagating from the surface with the deflagration front, when the remaining fuel burns in the central zone. Thus, there is a mixed regime of the thermonuclear explosion of a carbon-oxygen white dwarf, which is most promising from the viewpoint of explosive nucleosynthesis (Niemeyer and Woosley 1997). On the other hand, Fig. 3 illustrates burning without noticeable pulsations in the ordinary detonation regime from the center (at $\alpha_c \geq 3.0 \times 10^{-3}$).

In Fig. 5, central density and total energy are plotted against time for the calculation with the smallest $\alpha_c = 3.0 \times 10^{-4}$. Here, the total number of pulsations is considerably larger than that in the preceding figure, but only fourteen of them were accompanied by the deflagration of another mass zone, which is clearly seen from the characteristic, narrow peaks of temperature T_c . Note that the small jumps in E_{tot} correspond to these narrow peaks because of energy release. In the calculation with $\alpha_c = 1.0 \times 10^{-3}$, from one to three mass zones burned out during each pulsation (except for the fifth

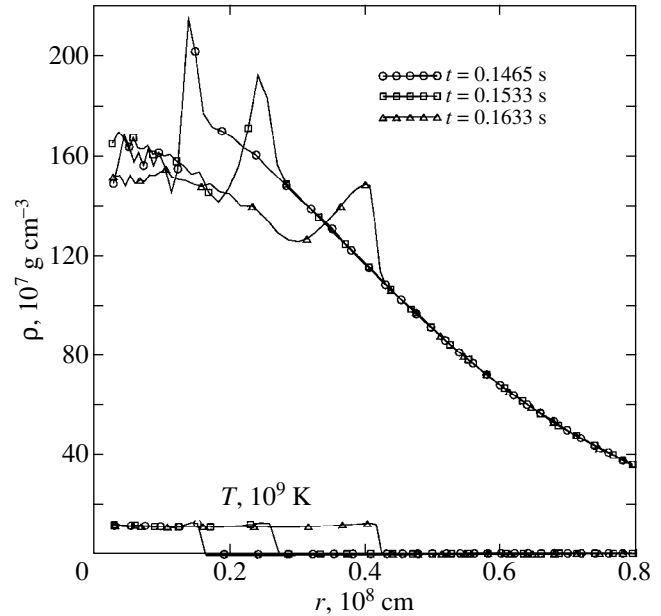


Fig. 7. Density and temperature versus radius for $\alpha_c = 3.0 \times 10^{-3}$ (rapid detonation).

and seventh pulsations), so almost all pulsations had the above temperature peaks (Fig. 4).

The deflagration regime is clearly characterized by the density profiles as a function of Euler radius r shown in Fig. 6 for $\alpha_c = 1.0 \times 10^{-3}$. At the deflagration front, the density abruptly decreases approximately by a factor of 1.5. Depending on the pulsation phase, the front sometimes retreats inward (compression phase), sometimes goes forward (expansion phase) against the general propagation (through mass zones). Pulsations are seen even more clearly in the behavior of the outer stellar shells, in as yet-unburned matter. The amplitude of these pulsations of the outer radius increases with time and reaches ~ 1.5 (this is clearly seen on the logarithmic density scale in Fig. 6).

The density profiles $\rho(r)$ for more intense convection are displayed in Fig. 7 for $\alpha_c = 3.0 \times 10^{-3}$. The temperature profiles $T(r)$, which clearly show (in the form of a jump) the location of the burning front, are displayed in the same figure on a small scale. We see that the matter density appreciably increases at the burning front, revealing the detonation regime of burning. The supersonic detonation is also revealed by the fact that the outer (with respect to the burning front) stellar shells are static.

Convection is completely characterized by the profiles of specific entropy, which are shown in Fig. 8 for $\alpha_c = 1.0 \times 10^{-3}$ as a function of mass coordinate m (on a logarithmic scale). At several typical instants of time, the convective zones that, according to the Schwarzschild criterion, correspond to the segments of a negative entropy gradient are marked on these profiles. This figure shows that the initial convective core breaks up during the explosion into several convective zones; the

largest of them includes one or two mass zones behind the burning front and the remnant of the convective core ahead of this front. The breakup is unsteady in nature and suggests that it is important to take into account unsteady convection.

Figure 8 shows entropy profiles before the emergence of detonation to the center. After this detonation emerges, the entropy behind the detonation front naturally increases in a short time of ~ 0.1 s to $(2-3) \times 10^8$ erg g^{-1} K $^{-1}$, which are also characteristic of deflagration, i.e., a factor of 4 to 6 larger than the initial entropy of $\sim 0.5 \times 10^8$ erg g^{-1} K $^{-1}$, with the gradient being positive. A negative entropy gradient remains only in the outermost shells (with $m \geq 1.36M_{\odot}$), and, consequently, convection that partly hampers the above detonation takes place.

The important role of the convection intensity characterized by α_c attracts particular attention. Clearly, the deflagration-pulsational burning (of course, deflagration is not necessarily accompanied by pulsations, but subsonic deflagration is a necessary condition for the latter) takes place over the entire range of α_c , $\alpha_{c \min} \leq \alpha_c \leq 2 \times 10^{-3}$. $\alpha_{c \min}$ is essentially higher than zero, because a hydrodynamic explosion at $\alpha_c = 0$ did not develop at all in our calculations, although the first mass zone burned out. Note that at higher critical central densities $\rho_{c \text{ cr}}$, which, in principle, increase with decreasing accretion rate (see above), $\alpha_{c \min}$ can decrease virtually to zero (Zmitrenko *et al.* 1978). At high densities $\rho_{c \text{ cr}}$, however, it becomes necessary to take into account neutrino energy losses and the kinetics of matter neutronization (Ivanova *et al.* 1977a, 1977c). In the case under consideration ($\rho_{c \text{ cr}} \approx 2 \times 10^9$ g cm $^{-3}$), these complex processes do not play a significant role, as was already shown by directly comparing the calculations of Ivanova *et al.* (1974), on the one hand, and Ivanova *et al.* (1977b), on the other, at a similar central density, $\rho_c = 2.33 \times 10^9$ g cm $^{-3}$. Thus, convection can prevent the development of pulsations in the deflagration regime of burning and can result in a detonation if α_c exceeds some critical value $\alpha_{c \text{ crit}}$. Here, we found that $\alpha_{c \text{ crit}} \approx 3 \times 10^{-3}$.

QUALITATIVE ANALYSIS OF PHYSICAL CONDITIONS FOR A DELAYED DETONATION

The formation of a detonation after the prolonged period of deflagration accompanied by the development of pulsations of an entire C–O stellar core may be called a delayed detonation (Niemeyer and Woosley 1997): several tens of seconds, i.e., much longer than the hydrodynamic time scale equal to the pulsation period (2–3 s) in order of magnitude, elapses since the central ignition of fuel. An analysis of the results shows that a detonation front forms approximately at a mass coordinate of $1.33M_{\odot}$ or, to be more precise, in zone no. 150 for the total number of zones equal to 170, with this coordinate being almost independent of α_c . In our model, zone no. 150 is distinguished, because Lagrangian zones decreasing in geometric progression

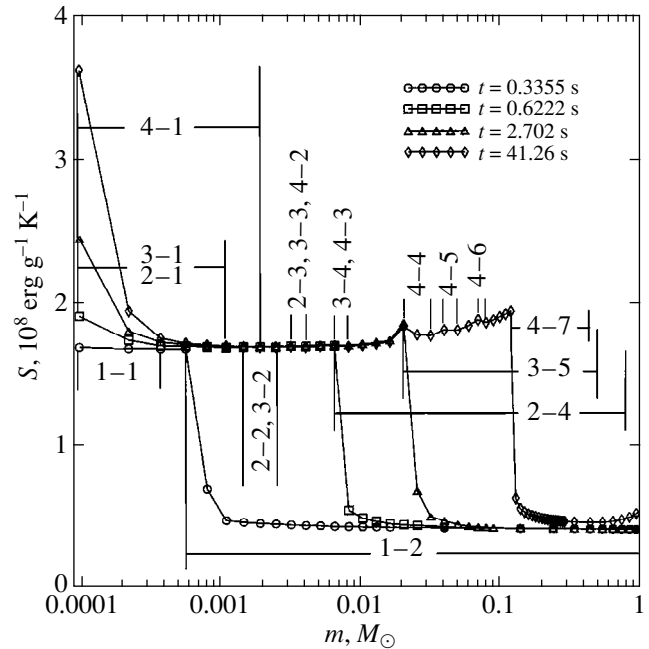


Fig. 8. Entropy versus mass for $\alpha_c = 1.0 \times 10^{-3}$ (before the formation of detonation). Convection zones are marked by numbers; for example, 2–1 denotes the first convection zone for the second instant of time ($t = 0.6222$ s).

were added after it at the presupernova stage. In the study by Dunina-Barkovskaya and Imshennik (2000), a detonation front formed in zone no. 127 (for the total number of zones equal to 150), after which the Lagrangian zones also decreased in geometric progression. Therefore, the effect of a nonuniform Lagrangian grid on the formation of detonation must be investigated in subsequent calculations. However, we will attempt to physically justify the increase in entropy that gives rise to a detonation.

Immediately after the first several pulsations, i.e., long before the formation of a detonation front, the entropy in the outer mass zones begins to increase (Fig. 9). Two local entropy peaks, closer to ($m \approx 1.36M_{\odot}$) and slightly farther from the stellar edge ($m \approx 1.33M_{\odot}$), are formed by $t = 45.098$ s (the beginning of the last pulsation). Although the specific entropy at the inner peak is smaller than that at the outer peak, the temperature at the former immediately before the onset of detonation increases more rapidly (because of the higher density). A detonation front forms near this peak (see Fig. 11). We can see that the increase in entropy was large even between close times, $t = 2.577$ and 2.850 s. These times lie between the minimum and maximum of the second (!) pulsation (see Fig. 4), which, however, is smaller in amplitude than the subsequent pulsations.

Based on the corresponding density profiles (Fig. 10), we can make sure that times close to the pulsation maxima are accompanied by the subsequent emergence of a compression wave on the stellar surface. Ivanova *et al.* (1982) estimated the increase in entropy (ΔS) in

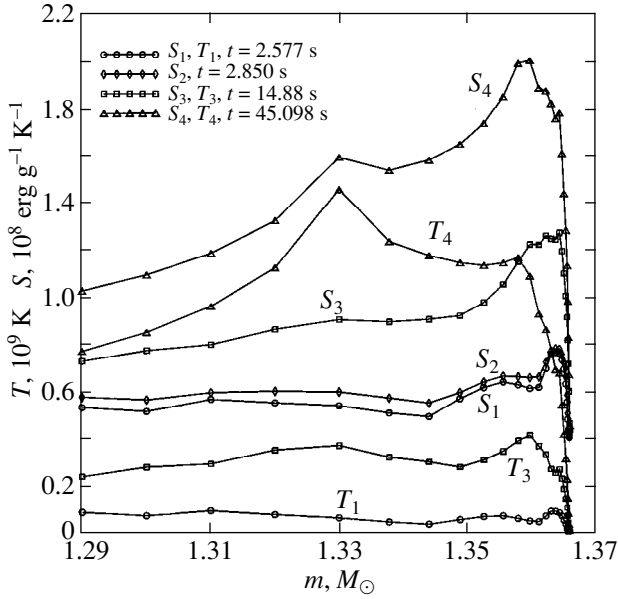


Fig. 9. Entropy and temperature versus mass in the outer shells of a C–O core for $\alpha_c = 1.0 \times 10^{-3}$ during pulsational deflagration (until the beginning of the last pulsation with the formation of detonation).

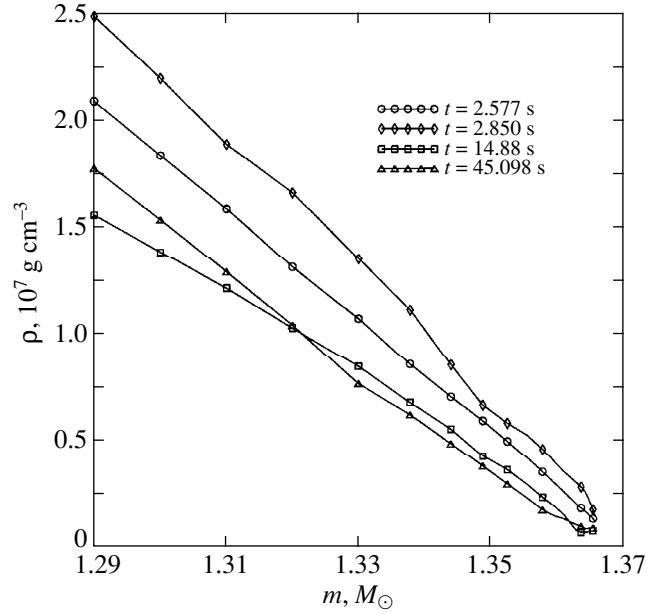


Fig. 10. Density versus mass in the outer layers of a C–O core for $\alpha_c = 1.0 \times 10^{-3}$ (pulsational deflagration until the formation of detonation).

such compression waves, which should be treated as weak shock waves with a jump in pressure ΔP with the well-known growth of entropy (Landau and Lifshitz 1954):

$$\Delta S = \frac{1}{12T_1} \left(\frac{\partial^2 V}{\partial P_1^2} \right)_s (\Delta P)^3. \quad (13)$$

It is easy to apply this relation to the case under consideration, because only the pressure of a completely degenerate ultrarelativistic electron gas may be taken into account when calculating the adiabatic second derivative from Eq. (13): $P_{le} = K\rho_1^{4/3}$, where $K = 4.90 \times 10^{14} \text{ cm}^3 \text{ g}^{-1/3} \text{ s}^{-2}$; hence

$$\left(\frac{\partial^2 V}{\partial P_1^2} \right)_s = \left(\frac{\partial^2 V}{\partial P_1^2} \right)_{s=0} = \frac{d^2 V}{dP_{le}^2} = \frac{21}{16} \frac{1}{K^2 \rho^{11/3}}. \quad (14)$$

This approximation is possible, because the values of ρ_1 and T_1 at $t = 2.577$ s may be taken as their estimates in front of a weak shock wave in the zone with $m = 1.33M_\odot$ under consideration: $\rho_1 = 1.073 \times 10^7 \text{ g cm}^{-3}$ and $T_1 = 6.64 \times 10^7 \text{ K}$. After simple transformations, we derive the final expression for the increase in specific entropy from Eq. (13) (S is in units of $10^8 \text{ erg g}^{-1} \text{ K}^{-1}$; see Fig. 9):

$$\begin{aligned} \Delta S_8 &= 0.536 \times 10^6 \frac{\rho_1^{1/3}}{T_1} \left(\frac{P_2}{P_1} - 1 \right)^3 \\ &= 1.78 \left[\left(\frac{\rho_2}{\rho_1} \right)^{4/3} - 1 \right]^3. \end{aligned} \quad (15)$$

The amplitude of a weak shock wave should also be specified in expression (15). The data of Fig. 10 yield $\rho_2 = 1.35 \times 10^7 \text{ g cm}^{-3}$ (for $t = 2.850$ s). Finally, we obtain from Eq. (15): $\Delta S_8 \approx 0.085$, whereas the increase in entropy between the same times in Fig. 9 is $\Delta S_8 \approx 0.06$. Thus, we can justifiably interpret the increase in entropy revealed by our calculations as resulting from the dissipation of weak shock waves in the region of a steep decrease in density. According to Eq. (15), the increase in entropy closer to the surface falls, because the density decreases to the edge; it most likely also falls inward because of the reduction in wave amplitude (see also Fig. 10). Nevertheless, the local entropy peak (Fig. 9) does not vanish in the course of time, but is preserved and greatly increases further by a factor of ~ 2.7 until the formation of detonation. It reaches $1.6 \times 10^8 \text{ erg g}^{-1} \text{ K}^{-1}$. Note that, unfortunately, this is not seen in Fig. 8, where the outer stellar shells are shown on a logarithmic mass scale, which is unsuitable in this region.

Figure 11 shows the temperature profiles from the formation of a detonation front ($t = 45.098$ s) until its collision with the deflagration front at $r \approx 5 \times 10^7 \text{ cm}$ (which corresponds to a mass from the center of $0.14M_\odot$) at $t = 45.212$ s. In this figure, we clearly see the started expansion of matter behind the detonation wave—the outer radius increased from 2.3×10^8 to $3.5 \times 10^8 \text{ cm}$ at a temperature of $\sim 10^9 \text{ K}$. In the detonation wave that propagates in the direction of increasing density, the temperature rises, in particular, because the heat capacity falls to 10^{10} K . The compression at the front is modest and characteristic—by a mere one and a half times (see Fig. 7). The jump in pressure is also

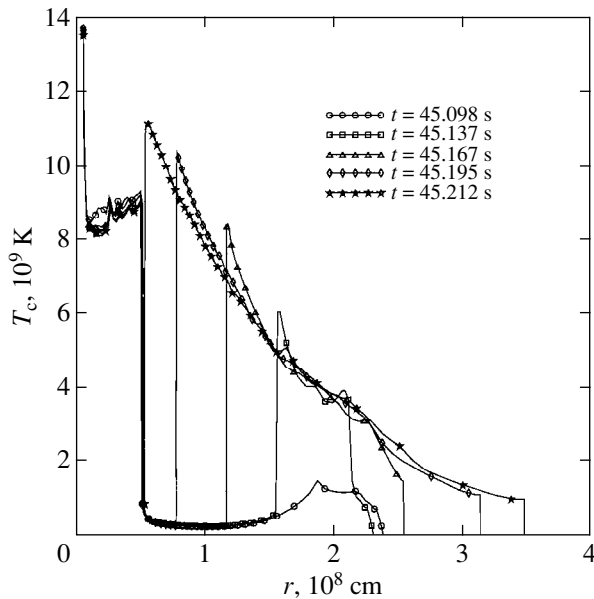


Fig. 11. Temperature versus radius during delayed detonation for $\alpha_c = 1.0 \times 10^{-3}$.

modest, approximately twofold until the end of burning. Remarkably, a detonation front is actually generated ($t = 45.137$ s) near the inner entropy peak (see Fig. 9), which corresponds to the inner temperature peak ($t = 45.098$ s) in Fig. 11.

The legitimate question arises as to whether this detonation front is stable against the galloping instability recently considered by Imshennik *et al.* (1999). This question requires an additional analysis, but stability intuitively seems more natural here: after all, the density ahead of the detonation front increases, which prevents the escape of the shock front from the burning zone. In all probability, stability against multidimensional perturbations is also supported by the large width of the burning zone, which is comparable to the radius of a C–O core at densities $\rho \sim 10^7$ g cm $^{-3}$ (Imshennik and Khokhlov 1984). This also means that the burning of a C–O mixture in the detonation wave “from the edge” actually does not reach the iron-peak elements, but is restricted mainly to the nuclides of Si etc. However, the problems of nucleosynthesis in the inferred regime of delayed detonation must be investigated further.

CONCLUSION

We have managed to derive the evolutionally justified initial conditions for the thermonuclear explosion of a carbon-oxygen stellar core with a mass close to the Chandrasekhar limit by taking into account accretion specified by a constant rate of $5 \times 10^{-7} M_\odot$ yr $^{-1}$. The latter was qualitatively justified in theoretical works on the evolution of C–O cores in close binary systems. In such a calculation, the explosion of a C–O core starts at some instant of time determined during this calcula-

tion. This removes the complex problem of choosing initial conditions, on which the very formation of explosion largely depended. Previously (Ivanova *et al.* 1974, 1977a–1977c), initial temperature profiles were specified as the initial conditions, strictly speaking, without an adequate justification.

Our series of calculations includes the standard approximate model of nonadiabatic convection—the mixing-length approximation specified with the only arbitrary parameter α_c (the ratio of mixing length l_{mix} to radial convection-zone size Δr_c). This parameter can most likely be determined from currently available multidimensional approaches (see Lisewski *et al.* 2000); i.e., the arbitrariness assumed in the approximate theory can be removed. Our calculations revealed that a delayed detonation takes place at a sufficiently low value of this parameter over a wide range, $3 \times 10^{-4} \leq \alpha_c \leq 2 \times 10^{-3}$, with the lower limit of this range being determined as a maximum estimate. At large values, $\alpha_c \geq 3 \times 10^{-3}$, our calculations yielded an ordinary detonation from the center of a C–O stellar core, which is unlikely to exist in reality because of burning-front instability etc. It would be of interest to establish whether the above range falls within the range of effective mixing-length parameters justified by the multidimensional theory of turbulence. However, the parameter α_c can be constrained by parametrically modeling the burning-front velocity. In particular, note that for $\alpha_c = 1.0 \times 10^{-3}$, this velocity is close to the laminar front velocity inferred by Woosley and Timmes (1992) when the first mass zone burns.

Here, using a new hydrodynamic code with a variable Lagrangian (difference) grid and taking into account the external boundary pressure attributable to accretion, we obtained a scenario for the development of a delayed detonation from the edge of a star to its center. The detonation is most likely stable against galloping instability and is determined by the preceding stage of the deflagration–pulsational regime of burning. This may prove to be important in connection with the recently appeared skepticism (Lisewski *et al.* 2000) over the previously published (Khokhlov *et al.* 1997) scenario for the deflagration-to-detonation transition due to the destruction of a laminar burning front by turbulent vortices.

ACKNOWLEDGMENTS

We are grateful to W. Hillebrandt for a helpful discussion. This study was supported in part by the International Science and Technology Center (project no. 0370) and the Russian Foundation for Basic Research (project no. 00-02-17230).

REFERENCES

1. W. D. Arnett, *Astrophys. Space Sci.* **5**, 180 (1969).
2. G. S. Bisnovatyĭ-Kogan, *Physical Problems in the Theory of Stellar Evolution* (Nauka, Moscow, 1989).

3. S. I. Blinnikov and O. S. Bartunov, *Astron. Astrophys.* **273**, 106 (1993).
4. S. I. Blinnikov and N. V. Dunina-Barkovskaya, *Astron. Zh.* **70**, 362 (1993) [*Astron. Rep.* **37**, 187 (1993)].
5. S. I. Blinnikov and N. V. Dunina-Barkovskaya, *Mon. Not. R. Astron. Soc.* **266**, 289 (1994).
6. S. I. Blinnikov and M. A. Rudzskii, *Pis'ma Astron. Zh.* **10**, 363 (1984) [*Sov. Astron. Lett.* **10**, 152 (1984)].
7. S. I. Blinnikov and A. I. Khokhlov, *Pis'ma Astron. Zh.* **12**, 318 (1986) [*Sov. Astron. Lett.* **12**, 131 (1986)].
8. S. I. Blinnikov, N. V. Dunina-Barkovskaya, and D. K. Nadyozhin, *Astrophys. J., Suppl. Ser.* **106**, 171 (1996).
9. N. V. Dunina-Barkovskaya and V. S. Imshennik, *Tr. Fiz. Inst. Akad. Nauk* **227**, 32 (2000).
10. W. Fowler and F. Hoyle, *Nucleosynthesis in Massive Stars and Supernovae* (University of Chicago Press, Chicago, 1965).
11. I. Hachisu, M. Kato, and K. Nomoto, *Astrophys. J. Lett.* **470**, L97 (1996).
12. M. Haft, G. Raffelt, and A. Weiss, *Astrophys. J.* **425**, 222 (1994).
13. I. Iben, *Astrophys. J.* **253**, 248 (1982).
14. V. S. Imshennik and A. M. Khokhlov, *Pis'ma Astron. Zh.* **10**, 631 (1984) [*Sov. Astron. Lett.* **10**, 262 (1984)].
15. V. S. Imshennik, N. L. Kal'yanova, A. V. Koldoba, and V. M. Chechetkin, *Pis'ma Astron. Zh.* **25**, 250 (1999) [*Astron. Lett.* **25**, 206 (1999)].
16. L. N. Ivanova, V. S. Imshennik, and V. M. Chechetkin, *Astrophys. Space Sci.* **31**, 497 (1974).
17. L. N. Ivanova, V. S. Imshennik, and V. M. Chechetkin, *Astron. Zh.* **54**, 354 (1977a) [*Sov. Astron.* **21**, 197 (1977a)].
18. L. N. Ivanova, V. S. Imshennik, and V. M. Chechetkin, *Astron. Zh.* **54**, 661 (1977b) [*Sov. Astron.* **21**, 374 (1977b)].
19. L. N. Ivanova, V. S. Imshennik, and V. M. Chechetkin, *Astron. Zh.* **54**, 1009 (1977c) [*Sov. Astron.* **21**, 571 (1977c)].
20. L. N. Ivanova, V. S. Imshennik, and V. M. Chechetkin, *Pis'ma Astron. Zh.* **8**, 17 (1981) [*Sov. Astron. Lett.* **8**, 8 (1982)].
21. A. M. Khokhlov, E. S. Oran, and J. C. Wheeler, *Astrophys. J.* **478**, 678 (1997).
22. L. D. Landau and E. M. Lifshitz, *Course of Theoretical Physics, Vol. 6: Fluid Mechanics* (GITTL, Moscow, 1954; Pergamon, London, 1959).
23. A. M. Lisewski, W. Hillebrandt, and S. E. Woosley, *Astrophys. J.* **538**, 831 (2000).
24. J. C. Niemeyer and S. E. Woosley, *Astrophys. J.* **475**, 740 (1997).
25. K. Nomoto, D. Sugimoto, and S. Neo, *Astrophys. Space Sci.* **39**, L37 (1976).
26. B. Paczyński, *Acta Astron.* **20**, 47 (1970).
27. E. E. Salpeter, *Aust. J. Phys.* **7**, 373 (1954).
28. E. E. Salpeter and H. M. van Horn, *Astrophys. J.* **155**, 183 (1969).
29. P. J. Schinder, D. N. Schramm, P. J. Wiita, *et al.*, *Astrophys. J.* **313**, 531 (1987).
30. S. E. Woosley, *Astrophys. J.* **476**, 801 (1997).
31. S. E. Woosley and F. X. Timmes, *Astrophys. J.* **396**, 649 (1992).
32. D. G. Yakovlev and D. A. Shalybkov, *Itogi Nauki Tekh., Ser. Astron.* **38**, 191 (1988).
33. L. R. Yungel'son, in *Proceedings of the International Conference "Modern Problems of Stellar Evolution," Zvenigorod, 1998* (GEOS, Moscow, 1998), p. 79.
34. N. V. Zmitrenko, V. S. Imshennik, M. Yu. Khlopov, and V. M. Chechetkin, *Zh. Éksp. Teor. Fiz.* **75**, 1169 (1978) [*Sov. Phys. JETP* **48**, 589 (1978)].

Translated by V. Astakhov

Low State of the X-ray Burster SLX 1732-304 in the Globular Cluster Terzan 1 According to RXTE Data

S. V. Molkov*, S. A. Grebenev, and A. A. Lutovinov

Space Research Institute, Russian Academy of Sciences, Profsoyuznaya ul. 84/32, Moscow, 117810 Russia

Received October 23, 2000

Abstract—Observations of the X-ray burster SLX 1732-304 in the globular cluster Terzan 1 with the PCA/RXTE instrument in April 1997 are presented. The source was in a low state; its flux in the standard X-ray band was half the flux recorded by the ART-P/Granat telescope in 1990 also during its low state. At the same time, its spectrum was softer than the ART-P spectrum; it was well described by a power law with a photon index of 2.3 without any evidence of a high-energy cutoff. © 2001 MAIK “Nauka/Interperiodica”.

Key words: *neutron stars, bursters, X-ray sources, and globular clusters*

INTRODUCTION

Globular clusters stand out from the Galactic stellar population by a high abundance of low-mass binary systems, with one of their components being a relativistic, degenerate object—a neutron star or a white dwarf. X-ray sources were discovered in twelve globular clusters (Hut *et al.* 1992). Type I X-ray bursts were observed from most of them, which is indicative of the nature of their compact object, a neutron star with a weak magnetic field.

X-ray emission from the region of the globular cluster Terzan 1 was first detected by the HAKUCHO satellite precisely during bursts (Makishima *et al.* 1981; Inoue *et al.* 1981). The two detected bursts were identified with a persistent X-ray source later, in 1985, when first X-ray images of this region were obtained with the XRT telescope of the SPACELAB-2 space laboratory (Skinner *et al.* 1987). The flux from the source, designated as SLX 1732-304, was 1.8×10^{-10} erg cm⁻² s⁻¹ in the 3–30-keV energy band. Subsequent observations of several X-ray missions showed that the source's emission was highly variable in intensity. The most catastrophic decline in flux was recorded in 1999 by the BeppoSAX observatory. The 2–10-keV flux fell to 4.8×10^{-13} erg cm⁻² s⁻¹ (Guainazzi *et al.* 1999). The data obtained with the ART-P X-ray telescope onboard the Granat observatory in the fall of 1990 (Pavlinky *et al.* 1995, 2001) were of considerable importance in investigating the variability of SLX 1732-304. The source was detected in two different intensity states, a

low state similar to that observed by the XRT telescope and a high state with 3–20-keV fluxes of 1.6×10^{-10} and 7.0×10^{-10} erg cm⁻² s⁻¹, respectively. Variations in intensity were apparently accompanied by hardness variations: whereas the source during its high state had the thermal spectrum with a distinct exponential cutoff at high energies typical of bright low-mass X-ray binaries, its low-state spectrum could be satisfactorily fitted by a power law with a photon index $\alpha \approx 1.7$. Here, we continue to analyze the spectral states of SLX 1732-304 based on its RXTE observations.

OBSERVATIONS

The PCA instrument onboard the RXTE (Rossi X-ray Timing Explorer) orbiting X-ray observatory consists of five identical proportional counters with a total area of 6500 cm², the operating energy range 2–60 keV, and an energy resolution $\approx 18\%$ at 6 keV (Bradt *et al.* 1993). Because of its large area, the instrument is sensitive enough for a spectral analysis of emission even from weak X-ray sources to be performed. The PCA field of view is limited by a collimator with a FWHM of 1°. Depending on peculiarities of the suggested study, observational data during their initial onboard reduction can be written in various telemetric formats. In the observations discussed here, we use data in three formats with a time resolution of 0.125 s, 16 s, and 1 μ s and an energy breakdown into 1, 129, and 256 channels, respectively. By the time the paper was written, SLX 1732-304 had been within the PCA field of view four times (table). The total exposure was eight hours.

We see from the table that during two observations, the flux from the source was approximately the same

* E-mail address for contacts: msv@hea.iki.rssi.ru

PCA/RXTE observations of SLX 1732-304 in 1997

Observation	Date	Starting time (UT)	Exposure, s	Flux, mCrab*
20071-10-01-00	April 18	06 ^h 02 ^m 08 ^s	5300	2.59 ± 0.06
20071-10-01-01	April 18	20 37 04	9200	2.70 ± 0.04
20071-10-01-02	April 19	17 20 16	10 800	2.75 ± 0.04
20071-10-01-03	April 20	01 04 48	3500	2.80 ± 0.09

* Mean 3–20-keV flux.

with an insignificant ($\sim 10\%$) trend toward its increase. The mean 3–20-keV flux was 6.7×10^{-11} erg cm $^{-2}$ s $^{-1}$; i.e., it was almost the flux recorded by ART-P in 1990 during the low state of SLX 1732-304. For this estimate, we subtracted the contribution of the 6.7-keV line of diffuse emission from hot gas in the Galactic bulge (see below). An analysis of the source's light curve revealed no appreciable variability of its emission on time scales of tens and hundreds of seconds. An analysis of the power spectra obtained from data written with a high time resolution revealed no variability at frequencies 1–1000 Hz either (the 3σ limit on the total power in this frequency range was 15%).

SPECTRUM

Since the spectra of SLX 1732-304 measured during different observing sessions were similar in shape, we

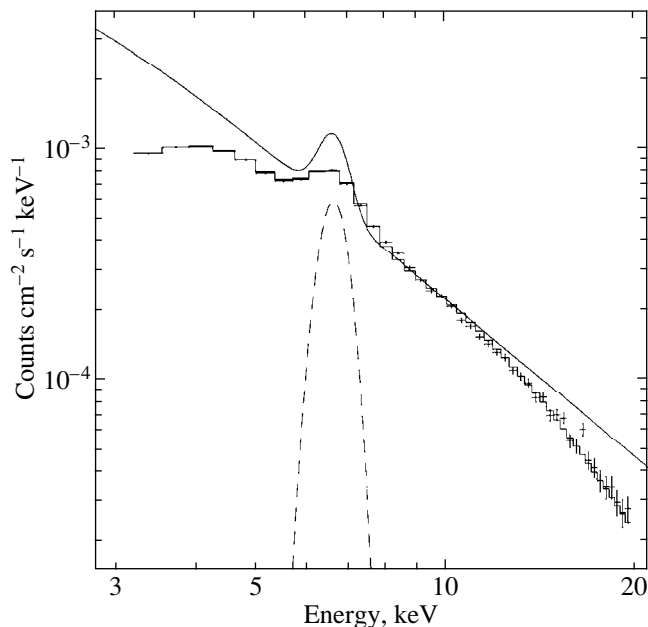


Fig. 1. PCA pulse-height spectrum of SLX 1732-304 in 1997. The histogram and the solid line indicate its best fit and the corresponding photon spectrum, respectively. The 6.7-keV line is attributable to the diffuse emission of hot plasma in the Galactic-center region.

performed a detailed analysis for the mean spectrum. Data written with a 16-s time resolution in the 3–20-keV energy band were used. The PCA response matrix at lower and higher energies is known with a large uncertainty. The pulse-height spectrum of the source is shown in Fig. 1 together with its power-law fit (histogram). The best-fit parameters are photon index $\alpha = 2.332 \pm 0.007$ and intensity at 10 keV $I_{10} = (2.236 \pm 0.023) \times 10^{-4}$ phot. cm $^{-2}$ s $^{-1}$. The interstellar absorption (atomic hydrogen column density) was fixed at $N_{\text{H}} = 1.8 \times 10^{22}$ cm $^{-2}$, which was measured by the ROSAT observatory under the assumption of solar elemental abundances (Johnston *et al.* 1995). In the PCA operating range, the effect of such absorption is essentially weak. As can be seen from the figure, the measured spectrum exhibits an intense emission line at energy ~ 6.7 keV. This line is most likely unrelated to the source SLX 1732-304 itself, but is a superposition of the diffuse 6.64-, 6.67-, 6.68-, and 6.7-keV lines of Fe XXV, whose ions recombine in clouds of hot plasma near the Galactic center. Using LAC/GINGA observations (Yamauchi and Koyama 1993), we estimated the expected intensity of the iron-line emission to be $F_{6.7}^* \approx (6-8) \times 10^{-4}$ phot. cm $^{-2}$ s $^{-1}$ toward the globular cluster Terzan 1. Direct measurements of the line intensity in the measured spectrum yielded $F_{6.7} = (4.92 \pm 0.22) \times 10^{-4}$ phot. cm $^{-2}$ s $^{-1}$. The line has the center at energy 6.662 ± 0.011 keV and a width of 339 ± 21 eV (σ in a Gaussian profile). Thus, the observed line can be entirely attributed to the diffuse emission of ionized iron.

Figure 2 shows that the above slight trend in the source's flux during the PCA observations was accompanied by changes in its spectrum. The figure presents the ratio of the April 18 (open circles) and April 20 (filled circles) spectra to the best fit to the mean spectrum. We see that maximum changes (up to 40%) took place at soft energies below 7 keV. We also see that there is a small excess of photons at energies ~ 8 keV in both spectra (or a deficit at energies ~ 10 keV) compared to the power-law fit to the mean spectrum.

DISCUSSION

Figure 3 shows the X-ray photon spectrum of SLX 1732-304 reconstructed from PCA data. The component attributable to the background diffuse 6.7-keV emission was removed. We ignored the possible contribution of the diffuse continuum emission. This spectrum was taken during the source's low state, in which it spends most of its time. Significantly, the observed spectrum is not just very hard, but it is well described by a power law over the entire PCA operating range without any evidence of a high-energy cutoff. The X-ray flux was a factor of ~ 2 lower than that recorded by ART-P in 1990, also during the source's low state. At the same time, the spectrum was steeper: the spectral slope had a photon index $\alpha \approx 2.3$, whereas the ART-P spectrum had a slope $\alpha \approx 1.7$. Discrepancies

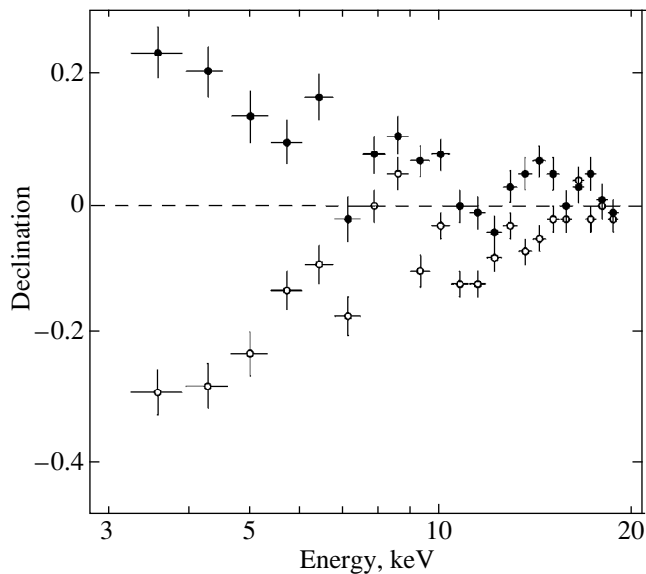


Fig. 2. Ratio of the pulse-height spectra measured from SLX 1732-304 on April 18 (open circles) and 20 (filled circles), 1997, to the power-law fit to the mean spectrum. The figure illustrates the source's spectral evolution on a time scale of three days of its PCA observations.

in the spectra are clearly seen in Fig. 3, in which the ART-P spectra of SLX 1732-304 observed in 1990 during its low and high states are indicated by open and filled circles, respectively. In particular, we see that the ART-P low-state spectrum is in better agreement with a hard Comptonized spectrum than with just a power law. This can serve as evidence that this spectrum originated in an optically thicker plasma than did the PCA spectrum. It is much more similar to the source's high-state spectrum. In general, it should be said that the PCA data contribute appreciably to the study of various spectral states of SLX 1732-304.

ACKNOWLEDGMENTS

This study was supported by the Russian Foundation for Basic Research (project nos. 99-02-18178 and 00-15-99297).

REFERENCES

1. H. V. Bradt, R. E. Rothschild, and J. H. Swank, *Astron. Astrophys.*, Suppl. Ser. **97**, 355 (1993).
2. M. Guainazzi, A. Parmar, and T. Oosterbroek, *Astron. Astrophys.* **349**, 819 (1999).

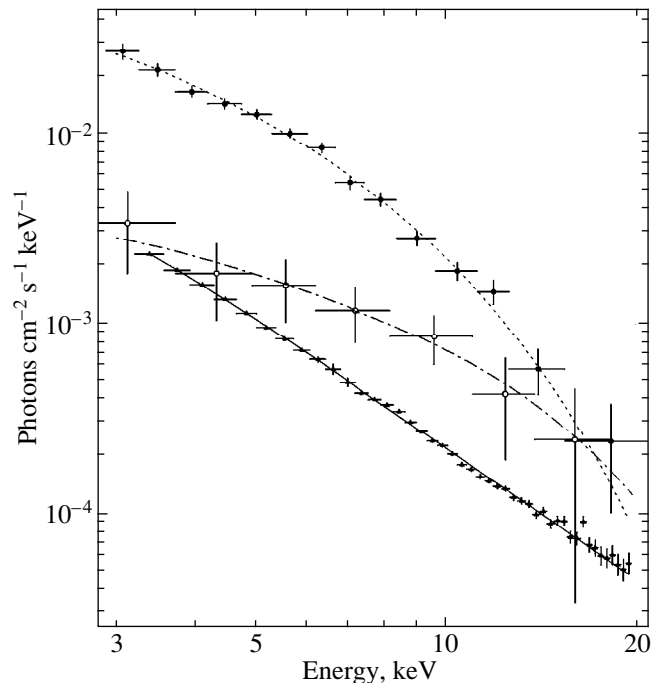


Fig. 3. PCA photon spectrum of the persistent X-ray emission (triangles) from SLX 1732-304 in 1997 during its low state. The source's ART-P/Granat spectra (Pavlinisky *et al.* 2001) measured during its low (open circles) and high (filled circles) states in 1990 are shown for comparison. The results of best fitting of these spectra by analytic models are indicated by curves.

3. P. Hut, S. McMillan, J. Goodman, *et al.*, *Publ. Astron. Soc. Pac.* **104**, 681 (1992).
4. H. Inoue, K. Koyama, K. Makishima, *et al.*, *Astrophys. J. Lett.* **250**, L7 (1981).
5. H. M. Johnston, F. Verbunt, and G. Hasinger, *Astron. Astrophys.* **298**, L21 (1995).
6. K. Makishima, T. Ohashi, H. Inoue, *et al.*, *Astrophys. J. Lett.* **247**, L23 (1981).
7. M. N. Pavlinsky, S. A. Grebenev, A. A. Lutovinov, *et al.*, *Pis'ma Astron. Zh.* **27**, 345 (2001) [*Astron. Lett.* **27**, 297 (2001)].
8. M. Pavlinsky, S. Grebenev, A. Finogenov, and R. Sunyaev, *Adv. Space Res.* **16** (3), 95 (1995).
9. G. Skinner, A. Willmore, C. Eyles, *et al.*, *Nature* **330**, 540 (1987).
10. S. Yamauchi and K. Koyama, *Astrophys. J.* **404**, 620 (1993).

Translated by V. Astakhov

Relativistic Gravitational Collapse of a Cool White Dwarf with Allowance for the Neutronization Kinetics

A. I. Voropinov and M. A. Podurets*

All-Russia Research Institute of Experimental Physics, Sarov, Russia

Received September 21, 2000

Abstract—We consider and numerically solve the problem of the relativistic gravitational collapse of a spherically symmetric cool nonrotating white dwarf with allowance for the neutronization kinetics. We propose a model equation of state and analyze the neutronization kinetics under simplifying assumptions. A comprehensive mathematical model is constructed for the phenomenon. The system of equations is integrated numerically. The gravitational collapse of a white dwarf that lost its stability is shown to lead to the envelope ejection and to the final state of a hot static neutron star. For comparison, we solve the problem with an equilibrium equation of state. We show that in this case, the entire mass ultimately goes under the gravitational radius to form a black hole. © 2001 MAIK “Nauka/Interperiodica”.

Key words: *general relativity, hydrodynamics, and kinetics*

INTRODUCTION

The mechanism for the transformation of a white dwarf into a neutron star has always aroused great interest. At present, this issue has not lost its topicality. Previously (Voropinov and Podurets 1976), we performed the first numerical calculations of relativistic gravitational collapse for a cool white dwarf under the most simplified assumptions. The main assumption was that of a single equation of state with the separation of pressure and energy density into cold and warm parts. The result of our calculations depended markedly on the asymptotics of the cold components of the equation of state. Collapse gives rise to a black hole for the ultrarelativistic asymptotics, $\epsilon_x = 3p_x$, and ceases for the hardest asymptotics, $\epsilon_x = p_x$. No envelope ejection is observed; the formation of accretion shock waves at the late stages of motion has no significant effect on the fate of the star. Note that these outgoing shock waves are the only source of entropy growth; the matter would remain cold without them during the entire motion.

At the same time, it has long been clear that there is another source of matter heating which acts virtually from the very beginning of the motion and therefore is capable of affecting the pattern of motion. This is nonequilibrium heating via the neutronization reaction. The nonequilibrium state takes place because the neutronization kinetics results from weak-interaction reactions and the corresponding time scales are comparable to the hydrodynamic time scales. It should be borne in

mind that, strictly speaking, heating is inevitable for a closed system, while our system (star) is open: neutrinos leave it freely. The net heating is therefore determined by the difference of two processes: nonequilibrium entropy production and heat losses into outer space. If these processes differ markedly in nature, then the result can be either: heating and cooling. In our case, however, these mechanisms are closely related. Both are determined by the neutronization kinetics; therefore, the result will be of fixed sign, and the net nonequilibrium heating will take place (see below for more details).

Thus, for a comprehensive mathematical model to be constructed, we must write the system of equations in general relativity, including the field equations and the equations of motion, kinetics, and state.

The system of field equations and the equations of motion and neutrino transfer for spherically symmetric motion in a comoving coordinate system was derived previously (Podurets 1998). For a numerical calculation, it was modified in much the same way as we did previously (Voropinov and Podurets 1976). Here, we do not use the neutrino transfer equation, because at this stage, our objective is to elucidate the role of the neutronization kinetics. The effect of the fact that neutrinos do not leave the system instantaneously will be elucidated in a different paper.

In addition to the system of equations, our model contains two important components: the equation of state and the kinetics. Below, we describe them successively.

* E-mail address for contacts: Podurets@albatross.md08.vniief.ru

EQUATION OF STATE

The main requirements for the equation of state are as follows:

(a) The equilibrium (in phase composition) cool equation of state must give a correct set of cool stellar configurations with two characteristic (Chandrasekhar and Oppenheimer–Volkov) maxima of the dependence of stellar mass on central density $M(\rho_0)$;

(b) The equation of state must be thermodynamically consistent and must satisfy the Nernst theorem to properly describe the heat capacity near zero temperature;

(c) The equation of state must be a multiphase one and must enable the natural introduction of neutronization kinetics.

A simple model of matter—a mixture of ideal gases of protons, electrons, and neutrons with equal number densities, as in the real matter composed of Fe⁵⁶ (as well as C¹², O¹⁶, and the so-called α -particle nuclei)—satisfies all these conditions. Condition (a) should be considered separately. The point is that the neutronization by the reaction $p + e \rightarrow n + \nu$ for an electron-proton gas begins in cold matter at too low a density, $\rho = 3.3 \times 10^7 \text{ g cm}^{-3}$, while in reality, the neutronization begins at $\rho \approx 10^9 \text{ g cm}^{-3}$. As a result, we obtain a noticeable displacement of the first maximum toward lower densities, which is undesirable, because this can affect the dynamics of collapse. We use the following artificial method to correct this defect. In the mixture of three gases, the proton component is least valuable (the pressure is determined by electrons at low densities and by neutrons at high densities). Therefore, we move the point of phase equilibrium from $\rho = 3.3 \times 10^7 \text{ g cm}^{-3}$ to $\rho = 10^9 \text{ g cm}^{-3}$ by artificially reducing the proton rest mass. To this end, it will suffice to assume that the modified proton rest mass accounts for 0.997 of the actual mass. Below, we assume the proton rest mass to be modified.

Each component is described by the equation of state for an ideal relativistic Fermi gas. For simplicity, we use not a quadrature form of the equation of state, but asymptotic expansions at low temperatures of the corresponding Fermi–Dirac integrals, retaining only the first temperature terms proportional to T^2 for the density, pressure, and internal energy and to T for the entropy. Recall that each term of the series is the product of a function of the chemical potential by the power of temperature. For example, we have for the particle number density

$$n(\mu, T) = n_0(\mu) + T^2 n_1(\mu). \quad (1)$$

However, this form is not convenient, because the equations of motion do not contain the chemical potentials, but contain the densities (along with the pressures and internal energy densities). We, therefore, reverse equations of the type (1) and write with the same accuracy in T

$$\mu(n, T) = \mu_0(n) + T^2 \mu_1(n), \quad (2)$$

where

$$\mu_0 = \sqrt{(3\pi^2 \hbar^3 c^3 n)^{2/3} + m^2 c^4}, \quad (3)$$

$$\mu_1 = -\frac{\pi^2}{6} \frac{2\mu_0^2 - m^2 c^4}{\mu_0(\mu_0^2 - m^2 c^4)}. \quad (4)$$

Substituting this expansion in other formulas, we can easily obtain an equation of state for each phase in the following form:

pressure

$$p = \frac{1}{12\pi^2 \hbar^3 c^3} \left[\mu_0 \sqrt{\mu_0^2 - m^2 c^4} \left(\mu_0^2 - \frac{5}{2} m^2 c^4 \right) + \frac{3}{2} m^4 c^8 \operatorname{arccosh} \frac{\mu_0}{m c^2} \right] + \frac{T^2}{18\hbar^3 c^3} \frac{(\mu_0^2 + m^2 c^4) \sqrt{\mu_0^2 - m^2 c^4}}{\mu_0}, \quad (5)$$

internal energy density

$$\varepsilon = \frac{1}{8\pi^2 \hbar^3 c^3} \left[\mu_0 \sqrt{\mu_0^2 - m^2 c^4} (2\mu_0^2 - m^2 c^4) - m^4 c^8 \operatorname{arccosh} \frac{\mu_0}{m c^2} \right] + \frac{T^2}{6\hbar^3 c^3} \mu_0 \sqrt{\mu_0^2 - m^2 c^4}, \quad (6)$$

entropy density

$$s = \frac{T}{3\hbar^3 c^3} \mu_0 \sqrt{\mu_0^2 - m^2 c^4}. \quad (7)$$

The entropy does not appear in the equation of state, but it is useful in interpreting the results.

Since, as was noted above, the system is a mixture of three noninteracting ideal gases, the pressure is additive: it is equal to the sum of partial pressures. In addition, the energy and entropy are also additive. We also assume that the volume and temperature are common to the three ideal gases under consideration. The former assumption is natural, and the latter assumption implies that the components are in thermal equilibrium with each other.

From the viewpoint of dynamics, the Gruneisen coefficient Γ —the ratio of thermal pressure to thermal energy—is an important parameter in the equation of state. In our case, based on relations (5) and (6), we have

$$\Gamma = \frac{1}{3} \left(1 + \frac{m^2 c^4}{\mu_0^2} \right). \quad (8)$$

Thus, the coefficient Γ does not depend on the temperature and varies with density in the range 1/3 to 2/3.

NEUTRONIZATION KINETICS

Before analyzing the kinetics proper, let us show how nonequilibrium heating proceeds in our open system. Previously, this kind of question was considered for different conditions (Bisnovatyĭ-Kogan and Seidov 1970; Imshennik and Chechetkin 1970).

Thus, let us specify a system with heat sinks whose power is dQ . For this system, the energy conservation law is

$$-dQ = dE + pdV. \quad (9)$$

We denote the quantities that refer to the entire volume by capital letters.

Since the system is a mixture of three noninteracting ideal gases, we write

$$S = S_p + S_e + S_n, \quad (10)$$

$$E = E_p + E_e + E_n, \quad (11)$$

$$p = p_p + p_e + p_n. \quad (12)$$

The following equality holds for each component:

$$TdS_k = dE_k + p_k dV - \mu_k dN_k.$$

Using relations (9)–(12), as well as the conditions for electrical neutrality, $N_e = N_p$, and for the conservation of the number of baryons, $N_p + N_n = \text{const}$, and denoting the number of neutrons by N , we obtain

$$TdS = -dQ + (\mu_p + \mu_e - \mu_n)dN. \quad (13)$$

The first and second terms are responsible for the loss and production of entropy, respectively, because $\mu_p + \mu_e > \mu_n$ in the nonequilibrium case and $dN > 0$ during the neutronization. Note that in the inverse process, the signs of the inequalities would be reversed, while the sign of the entropy production would be the same. The entropy production is seen to become zero in two extreme cases: when the reaction is either balanced ($\mu_p + \mu_e = \mu_n$) or frozen ($dN = 0$). Note also that if the sinks do not depend on the kinetics, then both the increase and decrease in entropy are possible.

In our instance, this is not the case. The heat sinks and the entropy production have a common nature, which enables us to estimate the right-hand part of Eq. (13). First note that the proportionality

$$dQ = \tilde{\epsilon} dN \quad (14)$$

takes place, where the mean energy lost by the system per single reaction event, i.e., the mean energy carried away by neutrinos, is denoted by $\tilde{\epsilon}$. Thus,

$$TdS = (\mu_p + \mu_e - \mu_n - \tilde{\epsilon})dN. \quad (15)$$

Let us consider strong degeneracy when the chemical potentials can be replaced by the corresponding Fermi energies. We then have

$$TdS = (\epsilon_{Fp} + \epsilon_{Fe} - \epsilon_{Fn} - \tilde{\epsilon})dN. \quad (16)$$

If the system is close to equilibrium, then only pairs (proton and neutron) with the Fermi energies can react; the newly produced neutron also has the Fermi energy, while the neutrino energy is zero. Since the energy is conserved in each unit event, i.e., $\epsilon_p + \epsilon_e = \epsilon_n + \epsilon_\nu$, the energy conservation law coincides in form with the chemical equilibrium condition. The increase in entropy is zero, as must be the case in equilibrium.

We have a different situation when the system is far from equilibrium, i.e., when

$$\epsilon_{Fp} + \epsilon_{Fe} > \epsilon_{Fn}. \quad (17)$$

In this case, the neutrino energy can change from minimum to maximum, with

$$\epsilon_{\nu\text{min}} = 0. \quad (18)$$

This case takes place when a pair for which $\epsilon_p + \epsilon_e = \epsilon_{Fn}$ interacts. If, however, particles with the Fermi energies react, then neutrinos are produced with the maximum energy

$$\epsilon_{\nu\text{max}} = \epsilon_{Fp} + \epsilon_{Fe} - \epsilon_{Fn}. \quad (19)$$

Thus, the mean energy carried away by neutrinos lies between its minimum and maximum, i.e.,

$$\tilde{\epsilon} = a(\epsilon_{Fp} + \epsilon_{Fe} - \epsilon_{Fn}),$$

where $0 < a < 1$. We then obtain for the sink power

$$dQ = a(\epsilon_{Fp} + \epsilon_{Fe} - \epsilon_{Fn})dN \quad (20)$$

and, according to Eq. (14), we have for the increase in entropy

$$TdS = (1 - a)(\epsilon_{Fp} + \epsilon_{Fe} - \epsilon_{Fn})dN. \quad (21)$$

Thus, for strong degeneracy of all three gases, we rigorously proved that the nonequilibrium heating accompanying the neutronization reaction was inevitable. Notice that both terms in the right-hand part of Eq. (13) are proportional to the same quantity dN . Therefore, possible errors in specifying the kinetics proper (time dependence of N) cannot affect in any way, at least the sign of the effect.

Let us now turn to the general case of incomplete degeneracy. Here, the situation is much more complex, and the mean neutrino energy is difficult to estimate, as we did for strong degeneracy. We will not do this now, because we pursue mainly methodological objectives, and the model simplicity should be preferred at the early stage.

On these grounds, we assume that the heat sinks and the total increase in entropy have the same form as those for strong degeneracy (20) and (21), but with the Fermi energies replaced by the chemical potentials:

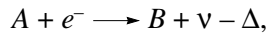
$$dQ = a(\mu_p + \mu_e - \mu_n)dN, \quad (22)$$

$$TdS = (1 - a)(\mu_p + \mu_e - \mu_n)dN. \quad (23)$$

Let us consider the kinetics in more detail; this will allow us to refine the parameter a . The neutronization

kinetics of stellar matter was first analyzed by Frank-Kamenetskiĭ (1962) for the gravitational collapse of a star. In a different formulation, as applied to the early stage of an expanding cold Universe, the problem was considered by Yakubov (1964). This problem is more complex. The reason is that the neutrino statistics has to be taken into account, because neutrinos cannot leave the system in a homogeneous Universe. By contrast, as we already noted above, the neutrino chemical potential in stars can be assumed to be zero. Subsequently, Frank-Kamenetskiĭ's result was used in a slightly simplified form by Zel'dovich and Guseĭnov (1965). We emphasize that, in essence, the above authors did not aimed at determining the effect of neutronization on the dynamics of matter motion. On the contrary, the motion of matter was assumed to be specified. In our case, however, it is also important to take into account the effect of neutronization on the dynamics of matter motion; therefore, apart from an expression for the kinetics, an expression for the energy carried away by neutrinos should be derived in the same approximation. Only in this way will we be able to derive the correct relation between entropy production and heat losses. Below, we follow Frank-Kamenetskiĭ's method.

Thus, we consider a neutronization reaction of the type



where A and B are the nuclei, and Δ is the energy difference.

Before continuing our discussion, let us make one fundamental remark. Since the kinetics is generally completely independent of the equation of state, we will consider the general case of nuclear composition of matter. As we pointed out above, our assumption of a neutron-proton composition is nothing more than a modeling equation of state. When analyzing the kinetics, we therefore have the right to take into account the nuclear composition of matter. Apart from the fact that this assumption is more realistic, it is also important that including sufficiently heavy nuclei in the analysis greatly simplifies the problem of determining the probability of elementary neutronization. More specifically, the presence of nuclei dispenses with the need for considering the momentum conservation law, while the energy conservation law can be used in a simplified form by taking into account only the energy transfer from electrons to neutrinos. Accordingly, the complex integration over multidimensional phase space reduces to the integration over the electron energy alone. In this case, Δ is simply a constant, the rest-energy difference between the corresponding nuclei. We also use the simplifying assumption of electron-gas degeneracy. For the probability differential, we have

$$dW \propto |\langle H \rangle|^2 n_e \rho_\nu d\varepsilon, \quad (24)$$

where n_ε and ρ_ε are, respectively, the densities of electron and neutrino states per electron energy interval ε ;

and $\langle H \rangle$ is the corresponding matrix element. Since the density of electron states is proportional to the volume of momentum space,

$$n_\varepsilon \propto p^2 dp = \frac{1}{c^3} \varepsilon \sqrt{\varepsilon^2 - m_e^2 c^4}. \quad (25)$$

For neutrinos, we have

$$\rho_\nu \propto p_\nu^2 dp_\nu = \frac{1}{c^3} \varepsilon_\nu^2 d\varepsilon_\nu = \frac{1}{c^3} (\varepsilon - \Delta)^2 d\varepsilon, \quad (26)$$

where the simplified energy conservation law discussed above was used in the last equality. The energies ε and Δ are measured in units of $m_e c^2$.

We may then write

$$dW = \text{const} \varepsilon \sqrt{\varepsilon^2 - 1} (\varepsilon - \Delta)^2 d\varepsilon. \quad (27)$$

Here, the product of all constants by the square of the modulus of the matrix element that does not depend on the electron energy is denoted by const . It is important to us that the differential probability of the inverse process (β decay) has exactly the same form. The only difference is that when the total reaction probability per unit time is calculated, the integration within different limits should be performed.

We have

$$W_\beta = \text{const} \int_1^\Delta \varepsilon \sqrt{\varepsilon^2 - 1} (\varepsilon - \Delta)^2 d\varepsilon, \quad (28)$$

for the probability of β decay and

$$W = \text{const} \int_\Delta^{\varepsilon_p} \varepsilon \sqrt{\varepsilon^2 - 1} (\varepsilon - \Delta)^2 d\varepsilon, \quad (29)$$

for the probability of neutronization.

The constant can now be expressed from relation (28) and substituted in Eq. (29). We introduce the following notation:

$$W_\beta = \frac{1}{t_\beta},$$

where t_β is the experimentally measured mean time per single reaction event, and

$$f = \int \varepsilon \sqrt{\varepsilon^2 - 1} (\varepsilon - \Delta)^2 d\varepsilon$$

is the Fermi statistical function. The neutronization probability can then be written as

$$W = \bar{W} \frac{1}{t_\beta f}, \quad (30)$$

where the dimensionless function is

$$\bar{W} = w(\varepsilon_F) - w(\Delta), \quad (31)$$

with

$$\begin{aligned}
 w(\varepsilon) &= \int_1^\varepsilon \varepsilon \sqrt{\varepsilon^2 - 1} (\varepsilon - \Delta)^2 d\varepsilon \\
 &= \frac{1}{60} \{ 12\varepsilon^4 - 30\varepsilon^3 \Delta + 4(5\Delta^2 - 1)\varepsilon^2 + 15\varepsilon \Delta \\
 &\quad - 4(5\Delta^2 + 2) \} \sqrt{\varepsilon^2 - 1} + \frac{1}{4} \Delta \ln(\varepsilon + \sqrt{\varepsilon^2 - 1}).
 \end{aligned} \quad (32)$$

The introduced time t_β is nothing but the time in which the number of particles decreases by a factor of e . This follows from the fact that the equation for the kinetics of β decay can be written as

$$\frac{dn}{dt} = -\frac{n}{t_\beta}.$$

The half-life $t_{1/2} = t_\beta \ln 2$ is commonly used.

The equation for the neutronization kinetics is written in the same form

$$\frac{dn_e}{dt} = -n_e \frac{\bar{W}}{t_\beta f}. \quad (33)$$

We now make a more general remark. In our approximation, ε_F is the Fermi electron energy (relative to the rest energy), and Δ is a constant reaction threshold. Below, we use the derived formula both for incomplete electron degeneracy and for an inconstant threshold. In this case, we change

$$\varepsilon_F \longrightarrow \frac{\mu_e}{m_e c^2} \quad \text{and} \quad \Delta \longrightarrow \frac{\mu_n - \mu_p}{m_e c^2}. \quad (34)$$

Now, having the neutronization kinetics, we may consider the energy loss through neutrino escape (heat sink) so as to compare it with the entropy production because of the nonequilibrium state, i.e., to compare the mean energy proportional to

$$\int_\Delta^{\varepsilon_F} (\varepsilon - \Delta) \frac{dw}{d\varepsilon} d\varepsilon, \quad (35)$$

with the maximum energy proportional with the same proportionality factor to

$$(\varepsilon_F - \Delta) \int_\Delta^{\varepsilon_F} \frac{dw}{d\varepsilon} d\varepsilon. \quad (36)$$

Having these values, we can calculate the important ratio a in Eqs. (22) and (23), which characterizes the total increase in entropy:

$$\begin{aligned}
 a &= \frac{\int_\Delta^{\varepsilon_F} (\varepsilon - \Delta) \frac{dw}{d\varepsilon} d\varepsilon}{(\varepsilon_F - \Delta) \int_\Delta^{\varepsilon_F} \frac{dw}{d\varepsilon} d\varepsilon}.
 \end{aligned} \quad (37)$$

The integral in the denominator was calculated above [see Eq. (32)]. Let us calculate the integral in the numerator. It is the sum of integrals; the second of them also reduces to the previously calculated integral. Denote

$$z(\varepsilon) = \int_1^\varepsilon \varepsilon^2 \sqrt{\varepsilon^2 - 1} (\varepsilon - \Delta)^2 d\varepsilon. \quad (38)$$

Then, we have

$$a = \frac{1}{\varepsilon_F - \Delta} \frac{z(\varepsilon_F) - z(\Delta)}{w(\varepsilon_F) - w(\Delta)} - \frac{\Delta}{\varepsilon_F - \Delta}. \quad (39)$$

The function $z(\varepsilon)$ is calculated in elementary functions and appears as follows:

$$\begin{aligned}
 z(\varepsilon) &= \frac{1}{240} \sqrt{\varepsilon^2 - 1} \{ (\varepsilon^2 - 1) [40\varepsilon^3 - 96\Delta\varepsilon^2 \\
 &\quad + 30(2\Delta^2 + 1) - 64\Delta] + 15\varepsilon(2\Delta^2 + 1) \} \\
 &\quad - \frac{2\Delta^2 + 1}{16} \ln(\varepsilon + \sqrt{\varepsilon^2 - 1}).
 \end{aligned} \quad (40)$$

As an illustration, let us calculate the functions $\alpha(\varepsilon_F)$ for various parameters Δ . Consider three parameters corresponding to three cases:

- (a) Nucleus A is a proton and nucleus B is a neutron;
- (b) Nucleus A is a proton with a modified mass (see Section 3) and nucleus B is a neutron;
- (c) Nucleus A is Fe^{56} and nucleus B is Mn^{55} .

In the first, second, and third cases, $\Delta = 2.75, 8.017,$ and 22.4 , respectively (Frank-Kamenetskii 1962).

Before performing our calculations, let us consider the limiting cases $\varepsilon_F = \Delta$ and $\varepsilon_F = \infty$. Calculating the second value is straightforward. Retaining the highest-degree terms in w and z , we easily find that, irrespective of Δ ,

$$a_\infty = \frac{5}{6}. \quad (41)$$

The second limiting case is also simple. If the non-zero factors in the integrands are replaced with their values at point $\varepsilon = \Delta$, then we obtain

$$\begin{aligned}
 a_\Delta &= \frac{\int_\Delta^{\varepsilon_F} (\varepsilon - \Delta)^3 d\varepsilon}{(\varepsilon_F - \Delta) \int_\Delta^{\varepsilon_F} (\varepsilon - \Delta)^2 d\varepsilon} = \frac{3}{4}.
 \end{aligned} \quad (42)$$

Table

ϵ_F/Δ	1	1.1	1.5	2	2.5	4	10	∞
$\Delta = 2.75$	0.75	0.7574	0.7773	0.7912	0.7997	0.8123	0.8255	0.8333
$\Delta = 8.017$	0.75	0.7570	0.7764	0.7904	0.7990	0.8120	0.8249	0.8333
$\Delta = 22.4$	0.75	0.7569	0.7763	0.7903	0.7989	0.8119	0.8249	0.8333

It would be natural to introduce a single variable, ϵ_F/Δ , and to examine the behavior of $a\left(\frac{\epsilon_F}{\Delta}, \Delta\right)$ for various parameters. The dependence on the parameter cannot be completely avoided, because the functions w and z are not homogeneous in ϵ and Δ . Nevertheless, numerical calculations show that the dependence on the parameter is very weak; virtually three significant digits of $a\left(\frac{\epsilon_F}{\Delta}\right)$ coincide for various parameters. The results of our calculations are given in the table. We see from this table that the essentially unified dependence $a(\epsilon_F/\Delta)$ is a monotonically increasing function within the limits

$$\frac{3}{4} \leq a \leq \frac{5}{6}. \quad (43)$$

Thus, we managed to considerably improve the previously obtained estimate ($0 \leq a \leq 1$). Accordingly, the fraction of the energy that goes into nonequilibrium heating lies in the range

$$\frac{1}{6} \leq 1 - a \leq \frac{1}{4}. \quad (44)$$

Our estimate yields a maximum fraction of the energy that goes into heating equal to 1/4. As Bisnovatyĭ-Kogan *et al.* (1974) showed, this value can be even larger ($1 - a = 0.4$) if the excitation of nuclei is taken into account.

Knowing the numerical value of a , we can specify the sink power in the form (20). We emphasize that this specification has an advantage over the direct calculation with our model. Recall that nonequilibrium heating results from the action of two opposite factors: entropy production and heat sinks. The formula for the production of entropy, $TdS = (\mu_e + \mu_p - \mu_n)dn$, is exact and depends neither on the equation of state nor on the kinetics model. By contrast, dQ is completely determined by models. As we have seen above, the net effect is a relatively small difference between the two quantities, and it may turn out that the sought-for effect will be appreciably distorted because of the mismatch between the equation of state and the kinetics. We therefore prefer to specify the sink power as a quantity proportional to the power of entropy production. In conclusion, we make one important addition. Equation (33) is valid only for stationary matter and describes the change in density via the neutronization reaction. In order to

derive the equation of kinetics that is also applicable to moving matter, we change from density to number density. Let us introduce the proton number density relative to the total number of baryons,

$$\lambda = \frac{n_p}{n_p + n_n}. \quad (45)$$

Then, since $n_p + n_n = \text{const}$ for stationary matter and since $n_e = n_p$ because of electrical neutrality, we obtain

$$\frac{d\lambda}{dt} = -\lambda \frac{\bar{W}}{t_{\beta f}}. \quad (46)$$

In this form, the equation of kinetics is valid along a streamline in stationary and moving matter. For a comoving frame, changing from the proper time to the coordinate time yields

$$\sqrt{S} \frac{\partial \lambda}{\partial \tau} = -\lambda \frac{\bar{W}}{t_{\beta f}}, \quad (47)$$

because the proper time t is related to the coordinate time τ by $dt = \frac{1}{\sqrt{S}} d\tau$, where $S = -g^{00}$ (the metric function S is not to be confused with entropy).

RESULTS OF CALCULATIONS

Below, we describe the solutions of two problems: problem no. 1 with an infinitely rapid kinetics and, consequently, with an equilibrium phase composition and problem no. 2 with a finite rate of kinetics and a non-equilibrium phase composition.

Problem No. 1

The equation of state for cold matter with an equilibrium phase composition can be derived from Eqs. (1)–(6) at $T = 0$ and with the constraint $\mu_p + \mu_e = \mu_n$. The composition was assumed to be equilibrium at $\rho \geq 10^9 \text{ g cm}^{-3}$. At lower densities, the number densities of all particles were assumed to be 1/3, as for Fe⁵⁶. The equation of state for cold matter was tabulated, with the number of points being of the order of 100 000, to achieve an accuracy of quadratic interpolation between tabulated points at a level of eight significant digits.

In our case, specifying a purely cold equation of state is admissible, because, as we will see below, no shock waves emerge here; i.e., there are absolutely no sources of heating. This problem was essentially solved

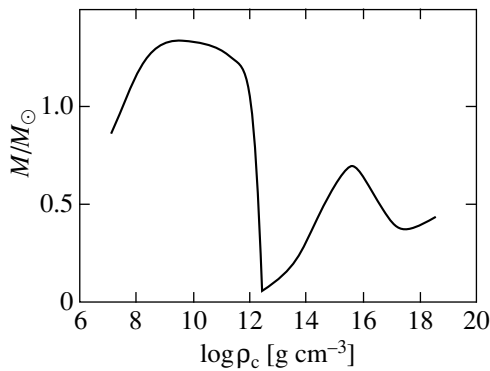


Fig. 1. Mass of equilibrium configurations versus central density.

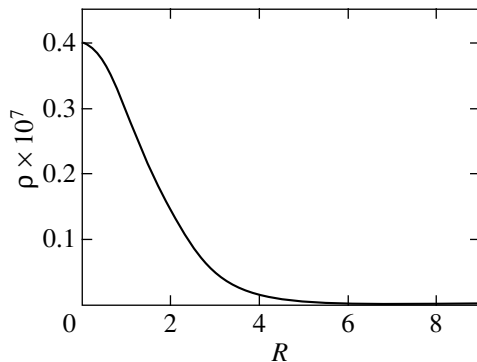


Fig. 2. The initially equilibrium pressure profile (stellar units).

previously (Voropinov and Podurets 1976), but with a slightly different equation of state taken from Harrison *et al.* (1967). Running ahead, note that the result of the problem with an equilibrium equation of state is qualitatively the same—relativistic collapse, while the details of the flow became different, mainly because the accuracy of our calculations is much higher. To specify the initial conditions, we computed a set of static solutions. In Fig. 1, stellar mass is plotted against central rest-mass density.

The first maximum corresponds to the initial conditions of the problem. Figure 2 shows the initial-state pressure profile, in stellar units (see below). In ordinary units, the central stellar density is $\rho_c = 1.079 \times 10^9 \text{ g cm}^{-3}$, and the stellar radius is $2.405 \times 10^8 \text{ cm}$. The system of field equations and equations of motion was integrated in a comoving coordinate system. We chose the observer's proper time at the stellar boundary as the coordinate time and the radius (the circumference length divided by 2π) of the initial static solution as the comoving (Lagrangian) radius. The number of computational points (zones) chosen uniformly in radius was 200.¹ We also performed calculations with a larger

¹ For a smaller number of points, some important features of the solution (for example, oscillations; see below) do not show up any longer. This is the reason why we overlooked them in our previous study (Voropinov and Podurets 1976), where the number of computational points was a mere 100.

number of points (up to 1000). It turned out that in this case, no new physical features of the solution emerged, while the computational time increased dramatically. We used an implicit difference scheme. The iteration accuracy was specified at 10^{-8} in pressure. The time step was chosen automatically. The selection criterion was the accuracy of the match between the results of a single step and the results of two successive computations of half-steps. The relative error in velocity was specified at 10^{-5} . In our stellar system of units, the speed of light and the gravitational constant are equal to unity, while the unit of time is 10^{-3} s . In this case, the unit of length is $2.99776 \times 10^7 \text{ cm}$, the unit of mass is $4.0382 \times 10^{35} \text{ g}$, and the unit of density is $1.499 \times 10^{13} \text{ g cm}^{-3}$.

The initially equilibrium star was disturbed from an equilibrium condition by the following artificial method. At the initial time, the centrally directed velocity was specified as

$$u = -0.1 \times 10^{-6} \left[3 \left(\frac{R}{R_0} \right)^2 - 2 \left(\frac{R}{R_0} \right)^3 \right],$$

where R_0 is the stellar radius.

The entire contraction of the star is clearly divided into four stages in time:

(1) The initial stage lasts from $\tau = 0$ to $\tau \approx 300 \text{ ms}$. The density (as well as pressure and energy) profiles become steeper, but generally retain their shapes, in particular, essentially preserve their monotonic behavior. This is the stage of comparatively slow contraction. Its rate and completion time depend to some extent on how the system is disturbed from an equilibrium condition.

(2) Starting from $\tau \approx 300 \text{ ms}$, after the density reaches $10^{10} \text{ g cm}^{-3}$ at the central points, the rapid contraction attributable to an abrupt decrease in Poisson adiabatic index begins. The separation of the entire star into a dense compact core and a considerably less dense, highly extended envelope begins at $\tau \approx 380 \text{ ms}$ and ends at $\tau \approx 450 \text{ ms}$. The core mass roughly corresponds to the first equilibrium minimum in the plot of equilibrium configurations (Fig. 1).

(3) The third stage appears as follows. Since the core was produced by a rapid process, its state is far from the state of rest; it oscillates about the equilibrium position corresponding to its mass. The core mass is not constant, and the envelope onflow on it continues, increasing its mass. Accordingly, the oscillation frequency increases. This regime takes place until the core mass becomes equal to the mass of the second maximum in Fig. 1 (Oppenheimer–Volkov maximum).

(4) The fourth stage, relativistic collapse, begins at $\tau \approx 710 \text{ ms}$.

The initial stages are conveniently illustrated by plots of central density ρ_c against time τ . In Fig. 3, central density is plotted against time in our stellar units for

the first two stages: the slow initial acceleration and the rapid stall completed with the core separation.

The third stage, the stage of oscillations with a slow increase in core mass, cannot be illustrated by a single plot because of the large number of (quasi-)periods. We therefore illustrate the situation by two figures. Figures 4 and 5 show central-density oscillations at the position of an equilibrium minimum mass and near an equilibrium maximum mass, respectively. The figures illustrate a smooth increase in density, with oscillations whose period decreases with time occurring against its background. Accordingly, the core radius oscillates in antiphase. The oscillation period decreases in accordance with the elementary theory of stellar pulsations with Newtonian gravitation. In this theory, the oscillation period is proportional to $\rho^{-1/2}$. An important point is that the period depends on the combination M/R^3 , i.e., on the density, rather than separately on the stellar radius R and mass M . We see from Figs. 4 and 5 that an increase in density by two orders of magnitude causes the period to decrease by almost an order of magnitude, in agreement with the pulsation theory.

Since the last, fourth stage is characterized by a rapid, catastrophic increase in central density, the $\rho_c(\tau)$ plot is not very informative here. The $R-\tau$ diagram in Fig. 6 illustrates this stage. At the stage of catastrophic contraction, streamlines' crossings of their gravitational radii are major events. A set of these events gives a line in the $R-\tau$ plane whose equation is $r = 2m$. Also shown here are $r = \text{const}$ lines and the start of the line of fall to the center ($r = 0$). We see that the crossings, as is usual for stars, do not take place simultaneously. The curve has a characteristic appearance with a minimum. Point no. 40 crosses most early, followed by adjacent points on both sides. The computation was interrupted at $\tau = 711.066278$, when the density at the central point became equal to $\rho_c = 0.61027 \times 10^{14}$, and the computation became impossible. By this time, point no. 70 had crossed its gravitational radius. The total rest mass enclosed within the sphere corresponding to this point accounts for $\approx 45\%$ of the star's total rest mass. For this reason, we do not worry that we had to interrupt the computation. The fate of the star has already been decided—the gravitational collapse of the entire star is inevitable.

Problem No. 2

In the problem under consideration, the neutronization rate is finite, and the equation of state is a three-phase equation with a nonzero temperature. The time constant in Eq. (47), $t_{\beta f}$, was set equal to 1200 s. The dimensionless parameter that characterizes the sink power (22) and (33) is set equal to $a = 0.75$, in accordance with the estimate (44).

The problem was also computed for three cases: with 200, 500, and 1000 points. No marked difference

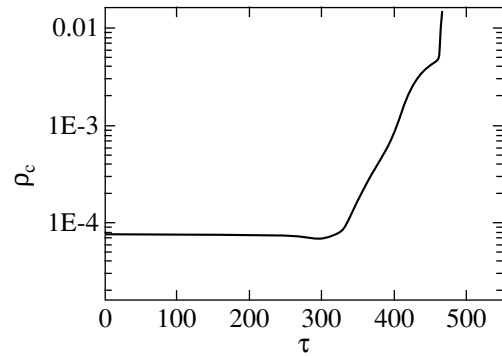


Fig. 3. Central density versus time for the first two stages (stellar units).

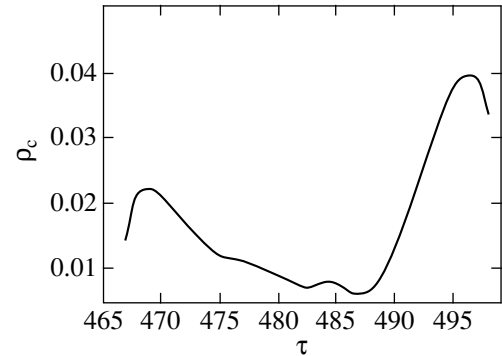


Fig. 4. Central density versus time at the beginning of the third stage (stellar units).

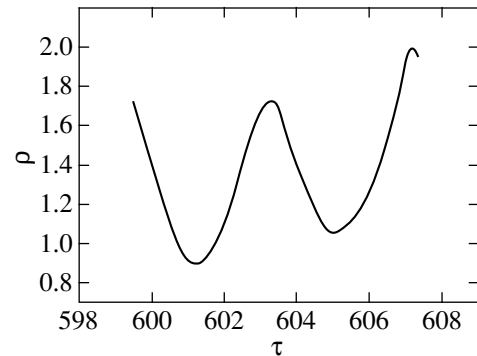


Fig. 5. Central density versus time at the end of the third stage (stellar units).

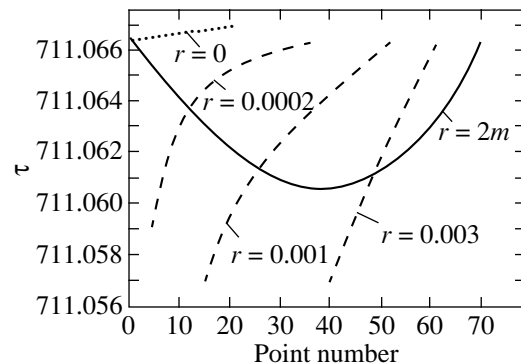


Fig. 6. The $R-\tau$ diagram near collapse (stellar units).

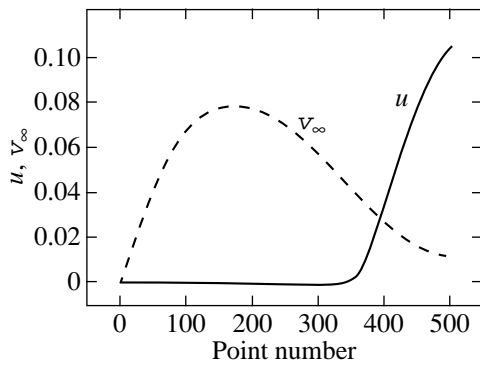


Fig. 7. The distributions of velocities u and v_∞ in points (stellar units).

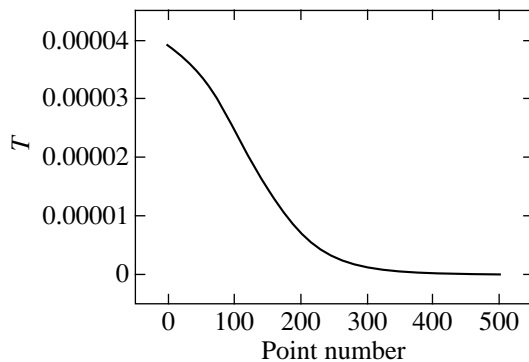


Fig. 9. The temperature distribution in points (the temperature is in units of $m_e c^2$).

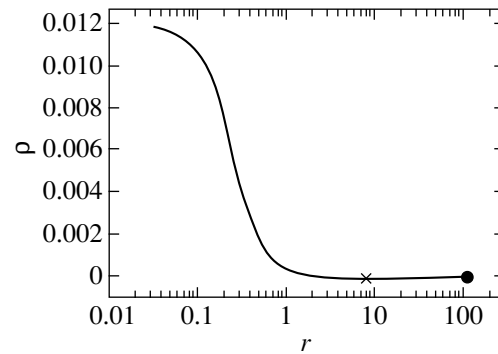


Fig. 8. Rest-mass density versus radius (stellar units). The circle marks the boundary point, and the cross marks the boundary point of the initial distribution.

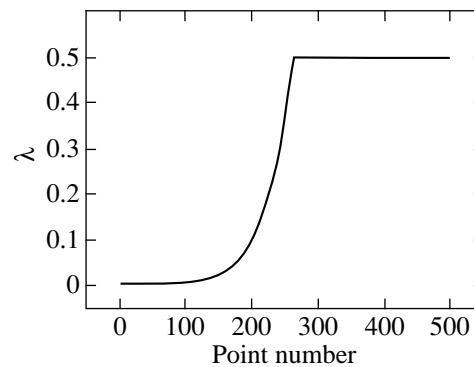


Fig. 10. The distribution of proton number density.

was found between them (particularly the last two). Qualitatively, the pattern of motion appears as follows.

The first two stages are similar to those described in problem no. 1: an almost equilibrium core breaks away, and the onflow of a highly rarefied envelope continues. However, there is also a marked difference. Since the equation of state lags behind the equilibrium state (the effective Poisson adiabatic index is larger than that in the previous case) and since the effective second viscosity attributable to the same factor is in action, the core breaks away in a much softer regime. In particular, the amplitude of the oscillations characteristic of the third stage in the preceding problem is considerably smaller, and they are damped out rapidly. However, the principle difference is that the onflow of matter on the core gives way to the inverse process—a collisionless, smooth envelope ejection takes place. This feature steadily shows up in all three computations with different numbers of points. At the same time, the core itself remains in static equilibrium; the central pressure, density, and other quantities remained constant in five significant digits for hundreds of milliseconds as long as the computation continued. The velocities in the envelope increase from the center out to the periphery, so the boundary velocity reaches ~ 0.10 – 0.12 of the speed of light by the end of our computation. It is of interest

to compare the gas velocities in the envelope with the parabolic velocity $v_\infty = \sqrt{\frac{2GM(r)}{r}}$ (we use the Newtonian formulas, because the general-relativity corrections in the envelope are small). Since the pressure in the envelope decreases with increasing distance from the center, the point at which the velocity becomes equal to v_∞ moves to the center as time passes. At the completion time of the computation ($t = 1250$ ms in the problem with 500 points), all points from no. 384 to no. 500 are bound to go to infinity. The mass carried away by them accounts for 6.2% of the total mass. However, this estimate is not accurate, but only a lower limit, because the matter at the inner points continues to accelerate, and its velocity can reach v_∞ . Note also that the mass of the envelope points with positive velocities accounts for 35% of the total stellar mass. An estimate of the ejected mass is required to predict the subsequent fate of the stellar remnant. As we saw above (see Fig. 1), the second mass maximum of cold configurations is considerably lower than the first maximum, so, for the stellar remnant to become an equilibrium one (both mechanically and thermodynamically) after cooling, no less than 48% of the mass must be ejected. Therefore, the above estimates most likely suggest that, in the long run, the remnant collapse is inevitable. It is impor-

tant to emphasize that this is valid only when the effect of baryon repulsion on the matter compressibility is ignored. Note also that we limited our computation to times of the order of 1000 ms not only because the computational time greatly increases, but also because the computation of an essentially nonrelativistic flow from the general-relativity equations becomes unreliable.

Thus, based on our computations, we established the very fact of envelope ejection. As regards the final fate of the stellar remnant, strictly speaking, the question is still largely an open question.

In conclusion, we provide parameter profiles that refer to the last computational time ($t = 1250$ ms for the computation with 500 points). Figure 7 shows the distributions of mass velocities $u = \dot{r}$ and escape velocities of free particle to infinity v_∞ in points.

Figure 8 shows the distribution of rest-mass density in radius r . We see that in the unsteady-state case, the stellar radius at the last time is more than an order of magnitude larger than the initial radius.

Figure 9 shows the temperature distribution. The temperature is given in energy units $m_e c^2$.

Figure 10 shows the distribution of λ : the proton number density relative to the total number of baryons. We see that the core at rest is a neutron star.

ACKNOWLEDGMENTS

We wish to thank V.S. Imshennik and D.K. Nadyozhin for helpful and stimulating discussions. This

study was supported in part by the International Scientific and Technical Center (project no. 370).

REFERENCES

1. G. S. Bisnovatyĭ-Kogan and Z. F. Seidov, *Astron. Zh.* **47**, 139 (1970) [*Sov. Astron.* **14**, 113 (1970)].
2. G. S. Bisnovatyĭ-Kogan, M. A. Rudzskiiĭ, and Z. F. Seidov, *Zh. Ėksp. Teor. Fiz.* **67** (5), 1621 (1974) [*Sov. Phys. JETP* **40**, 806 (1975)].
3. D. A. Frank-Kamenetskiĭ, *Zh. Ėksp. Teor. Fiz.* **42** (3), 875 (1962) [*Sov. Phys. JETP* **15**, 607 (1962)].
4. V. S. Imshennik and V. M. Chechetkin, *Astron. Zh.* **47** (5), 929 (1970) [*Sov. Astron.* **14**, 747 (1971)].
5. M. A. Podurets, Preprint No. 23-98, ITĖF (Inst. for Theoretical and Experimental Physics, Moscow, 1998).
6. A. I. Voropinov and M. A. Podurets, *Astron. Zh.* **53** (2), 349 (1976) [*Sov. Astron.* **20**, 198 (1976)].
7. B. K. Harrison, K. S. Thorne, M. Wakano, and J. A. Wheeler, *Gravitation Theory and Gravitational Collapse* (Chicago, Univ. of Chicago, 1965; Mir, Moscow, 1967).
8. V. B. Yakubov, *Astron. Zh.* **41** (5), 884 (1964) [*Sov. Astron.* **15**, 607 (1962)].
9. Ya. B. Zel'dovich and O. Kh. Guseĭnov, *Dokl. Akad. Nauk SSSR* **162** (4), 791 (1965) [*Sov. Phys. Dokl.* **10**, 524 (1965)].

Translated by V. Astakhov

Detection of Optical Circular Polarization in the Herbig Ae Star WW Vul

D. N. Shakhovskoi^{1*}, O. S. Shulov², and E. N. Kopatskaya²

¹ Crimean Astrophysical Observatory, p/o Nauchnyĭ, Crimea, 334413 Ukraine

² Astronomical Institute, St. Petersburg University, St. Petersburg, Russia

Received December 5, 2000

Abstract—*UBVRI* observations of circular polarization in WW Vul are presented. A positive polarization of $\sim 0.1\%$ was detected with a signal-to-noise ratio from 3 to 5 in each of the bands and more than 5 when averaged over all five bands. This observed polarization roughly corresponds to a 1% circular polarization of the radiation scattered in a circumstellar disk, which is most likely attributable to the significant alignment of scattering non-spherical dust grains. Since grain alignment is possible only in a magnetic field, this result provides circumstantial evidence for the existence of a magnetic field in the circumstellar disk of WW Vul. © 2001 MAIK “Nauka/Interperiodica”.

Key words: *young stars, polarization*

INTRODUCTION

Circular-polarization measurements for young stars are few in number. A statistically significant polarization of $\sim 0.05\%$ was first detected in T Tau, RY Tau, and SU Aur by Nadeau and Bastien (1986) and confirmed by observations with other instruments on other telescopes (Bastien *et al.* 1989). Hutchison *et al.* (1994) recorded a circular polarization exceeding 5σ in RU Lup, AK Sco, HD 144 669, and HD 97 048. For each of the stars, this result was obtained only on one of the nights and only in one band. Such a high polarization (0.07–0.5%) was observed in these stars neither on other nights nor in other filters on the same night. Of the 60 objects, a circular polarization exceeding 5σ was detected in separate series of measurements only in RY Lup and HD 163 296 (see the review article by Yudin and Evans 1998).

In UX Ori stars, which constitute a separate subclass of young stars with unusually high polarization activity (linear-polarization variability $\Delta P \sim 5\%$) (Grinin *et al.* 1991), circular polarization was detected only once. Observations of UX Ori at minimum light ($\Delta V \sim 2^m.5$) are given in Voshchinnikov *et al.* (1988). These authors observed a circular polarization of $\sim 1\%$ with an error of 0.3% on two successive nights. Averaging the results over these two nights yields $v = 1.1 \pm 0.2\%$. In the state of high brightness, the circular polarization in UX Ori does not exceed 0.3% and 0.1% as inferred from the data of the above authors and Hutchison *et al.* (1994), respectively.

WW Vul (A2e, $V = 10.3\text{--}12.7$) is one of the best-studied UX Ori stars. Its linear polarization at minimum light reaches 7% (Grinin *et al.* 1991). A peculiarity of WW Vul is the abnormal behavior of its linear polarization observed when the star was emerging from some of its minima (Grinin *et al.* 1988; Berdyugin *et al.* 1992), which cannot be explained in terms of the universally accepted model for this class of objects (Grinin 1988). According to this model, the variable linear polarization results solely from an increase in the contribution of the polarized radiation scattered in the circumstellar disk when the star is eclipsed by dust clouds. One of the probable causes of this behavior is the existence of an additional mechanism for the formation of linear polarization, absorption by aligned nonspherical particles (Berdyugin *et al.* 1992). Of particular interest in this connection is investigating circular polarization in WW Vul, because scattering by aligned nonspherical dust grains is an efficient formation mechanism of circular polarization (Dolginov *et al.* 1979).

OBSERVATIONS AND THEIR STATISTICAL ANALYSIS

We observed WW Vul at the Crimean Astrophysical Observatory on one night in 1996 and on five nights in 1997 using the 1.25-m telescope (AZT-11) equipped with the *UBVRI* photometer-polarimeter designed by Pirola (1975). A quarter-wave phase plate rotated discretely at steps of 90° every 20 s was placed in front of the polarization analyzer (a plane-parallel calcite plate). The intensities of the ordinary and extraordinary rays that emerged from the analyzer were measured quasi-simultaneously with a modulation frequency of

* E-mail address for contacts: dshakh@crao.crimea.ua

Table 1. Observations of circular polarization in WW Vul

Date	JD 245	m_V	N	$v_U, \%$	$v_B, \%$	$v_V, \%$	$v_R, \%$	$v_I, \%$	$P, \%$
June 18, 1996	0314	10.51	29	0.104 ± 0.089	0.099 ± 0.034	0.074 ± 0.038	0.031 ± 0.040	0.076 ± 0.040	–
July 3, 1997	0633	11.25	39	0.171 0.127	0.005 0.045	0.140 0.052	0.024 0.032	0.115 0.041	2.3
July 5, 1997	0635	11.45	60	0.305 0.130	0.150 0.041	0.210 0.056	0.110 0.027	0.120 0.034	–
July 6, 1997	0636	11.27	39	0.422 0.183	0.041 0.097	–0.067 0.083	0.099 0.062	0.089 0.064	–
July 11, 1997	0641	11.22	20	0.180 0.224	0.049 0.110	0.031 0.077	–0.007 0.044	0.014 0.057	1.2
July 12, 1997	0642	11.20	27	0.098 0.190	0.180 0.059	0.000 0.110	0.050 0.040	0.098 0.052	1.2

25 Hz. All measurements were made through a 15" aperture. The instrumental polarization was determined from observations of the unpolarized standard stars HD 18 803 and HD 144 287 and did not exceed 0.02% in all bands. Our observations are given in Table 1.

As we see from the table, a circular polarization exceeding 3σ was observed on JD 2450635 (July 5, 1997) in *BVRI* and on JD 2450642 (July 12, 1997) in *B*. On the remaining nights, the measurement accuracy was too low for a circular polarization to be detectable even at a 3σ level. To increase the accuracy, all the 1997 observations during which the star had virtually the same brightness, were combined into a single set and reprocessed. The results are presented in Table 2. The last two columns of this table list the measurement errors of circular polarization: σ is the error of the mean calculated from the actual scatter, and σ_0 is the expected error from the photon noise alone.

As we see from Table 2, the mean polarizations in different bands are similar and exceed 3σ in all bands, suggesting that the polarization is actually nonzero; moreover, its wavelength dependence is flat. In that case, it makes sense to average the polarization over all bands. This averaging with weights $w = \sigma^{-2}$ yields $\langle v \rangle = 0.086 \pm 0.015\%$.

In attempting to detect the lowest possible polarization, there is generally always a danger that the detected effect is attributable to one degree or another to disregarded instrumental errors. The entire observational procedure and our observational data were therefore critically analyzed at the St. Petersburg State University. As a result, we found the following: first, no possible instrumental errors could significantly affect the results of our observations, and, second, reprocessing our data by an independent method confirmed the results of Table 1 with insignificant (within the limits of observational error) discrepancies. In particular, the circular polarization averaged over all six observing nights and over all five bands was found to be $\langle v \rangle = +0.091 \pm 0.009\%$, while its value averaged over the five nights in 1997 is $\langle v \rangle = +0.090 \pm 0.018\%$, which is seen to be close to the above values.

In general, the results of this reprocessing match those given above. The circular polarization averaged over the five bands is $\langle v \rangle = 0.088 \pm 0.006\%$ for the

entire set of observations and $\langle v \rangle = 0.099 \pm 0.022\%$ for the 1997 observations.

DISCUSSION

Thus, we not only detected circular polarization in WW Vul, but also obtained information about its wavelength dependence (it is apparently flat) and about the pattern of its variability (it varies only slightly on a time scale of several days, because the signal-to-noise ratio improved considerably when the observations were averaged over eleven days).

Note that the circular polarization observed in UX Ori, an object of the same class as WW Vul, is an order of magnitude higher than that in WW Vul. This may be attributable to the fact that UX Ori was observed at minimum light ($\Delta V \sim 2^m.5$), while WW Vul was observed in an intermediate state ($\Delta V \sim 0^m.7$). For any of the possible formation mechanisms of circular polarization:

—transformation from linear polarization as light propagates in an anisotropic interstellar medium,

—multiple scattering by nonaligned dust grains, and
—scattering by aligned dust grains,

it would be natural to expect an increase in the observed polarization with increasing amount of dust on the line of sight and with increasing fraction of the scattered light in the observed radiation, which is the case at minimum brightness.

The high intrinsic circular polarization in WW Vul suggests scattering by aligned dust grains as the most plausible mechanism.

Indeed, the first mechanism can most likely be ignored, because the interstellar polarization is low, $P_{is} \sim 1.0\%$ for WW Vul (Grinin *et al.* 1988).

Table 2. Mean circular polarizations in WW Vul

Band	$v, \%$	$\sigma, \%$	$\sigma_0, \%$
<i>U</i>	0.245	0.049	0.067
<i>B</i>	0.090	0.022	0.025
<i>V</i>	0.102	0.025	0.031
<i>R</i>	0.063	0.015	0.016
<i>I</i>	0.099	0.019	0.021

If the source of circular polarization is the scattered disk radiation, then, knowing its intensity determined by analyzing observed color-magnitude diagrams for WW Vul, $I_{sc} \sim 0.05I_*$ (Grinin 1988), we obtain $I_{sc} = 0.1I_{obs}$ at the time of measurements ($V = 11.2$). Consequently, the intrinsic circular polarization of the scattered disk radiation is $v \sim 0.9\%$.

For multiple scattering by spherical particles in circumstellar disks, the circular polarization differs in sign during scattering in different disk quadrants (Bastien 1988), and the total circular polarization from the entire disk must be zero under axially symmetric conditions. Therefore, in the case of multiple scattering, one might expect circular polarization to emerge only when the disk shape deviates appreciably from axial symmetry. In principle, such deviations are possible under the effect of tidal perturbations in young binary systems. However, as an analysis of the above calculations by Bastien (1988) shows, the maximum circular polarization in such cases can hardly be comparable to the above estimate ($v \sim 0.9\%$).

For this reason, the third of the above mechanisms seems most plausible, because circular polarization in this case emerges even after a single scattering and can be high (Notni 1985). Note also that the emergence of circular polarization during scattering by aligned dust grains is well known for the solar zodiacal light, with its polarization ($\sim 0.5\%$; Dolginov and Mitrofanov 1975) being close to v for WW Vul and UX Ori.

CONCLUSION

We have concluded that the circular polarization in WW Vul is most likely attributable to scattering by aligned nonspherical particles. Since the alignment of nonspherical particles in most astrophysical situations is impossible without a magnetic field being involved (Dolginov and Mitrofanov 1975), this fact can be considered as circumstantial evidence for the existence of a magnetic field in the star's circumstellar disk.

Our estimates show that the circular polarization of the scattered radiation from the circumstellar disk of WW Vul is $\sim 0.9\%$. One might expect such a polarization at the deepest minima of WW Vul, when the star is completely obscured from the observer by a dust cloud, and the scattered radiation from circumstellar dust dominates.

In conclusion, note that our observations revealed a positive circular polarization in WW Vul. Circular

polarization of the same sign was observed in two of the three young objects of Bastien *et al.* (1989), in three of the four objects of Hutchison *et al.* (1994), in the two objects of Yudin and Evans (1998), and in UX Ori (Voshchinnikov *et al.* 1988); i.e., a positive polarization clearly dominates. This fact is of considerable interest and deserves a special study.

ACKNOWLEDGMENTS

We wish to thank V.P. Grinin for initiating this study and for helpful discussions. This work was supported by the Russian Foundation for Basic Research (project no. 99-02-18520).

REFERENCES

1. P. Bastien, in *Polarized Radiation of Circumstellar Origin*, Ed. by Coyne *et al.* (Vatican Observatory, Vatican City State, 1988), p. 303.
2. P. Bastien, C. Robert, and R. Nadeau, *Astrophys. J.* **339**, 1089 (1989).
3. A. V. Berdyugin, V. P. Grinin, and N. Kh. Minikulov, *Izv. Krym. Astrofiz. Obs.* **86**, 69 (1992).
4. A. Z. Dolginov and I. G. Mitrofanov, *Pis'ma Astron. Zh.* **1**, 38 (1975) [*Sov. Astron. Lett.* **1**, 246 (1975)].
5. A. Z. Dolginov, Yu. N. Gnedin, and N. A. Silant'ev, *The Propagation and Polarization of Emission in Space* (Nauka, Moscow, 1979).
6. V. P. Grinin, *Pis'ma Astron. Zh.* **14**, 65 (1988) [*Sov. Astron. Lett.* **14**, 27 (1988)].
7. V. P. Grinin, N. N. Kiselev, N. Kh. Minikulov, and G. P. Chernova, *Pis'ma Astron. Zh.* **14**, 514 (1988) [*Sov. Astron. Lett.* **14**, 219 (1988)].
8. V. P. Grinin, N. N. Kiselev, N. Kh. Minikulov, *et al.*, *Astrophys. Space Sci.* **186**, 283 (1991).
9. M. G. Hutchison, J. S. Albinson, and P. Barret, *Astron. Astrophys.* **285**, 883 (1994).
10. R. Nadeau and P. Bastien, *Astrophys. J. Lett.* **307**, L5 (1986).
11. P. Notni, *Astron. Nachr.* **306**, 265 (1985).
12. V. Pirola, *Ann. Acad. Sci., Ser. A*, No. 418, 61 (1975).
13. N. V. Voshchinnikov, V. P. Grinin, N. N. Kiselev, and N. Kh. Minikulov, *Astrofizika* **28**, 311 (1988).
14. R. V. Yudin and A. Evans, *Astron. Astrophys., Supl. Ser.* **131**, 401 (1998).

Translated by V. Astakhov

Close Binary Systems in Star-Forming Regions: EQ Ori in the Ori I Association

M. M. Zakirov*

Astronomical Institute, Academy of Sciences of Uzbekistan, Astronomicheskaya ul. 33, Tashkent, 700052 Uzbekistan

Received April 5, 1999; in final form, November 21, 2000

Abstract—Photoelectric (*UBVR*) observations of the eclipsing variable EQ Ori are presented. The ephemerides of primary minima are refined, and the range of the star's light variations is determined. All light curves are solved by Lavrov's direct method, and highly accurate photometric orbital elements are obtained for the system. The magnitudes and colors of each component are calculated and analyzed in two-color (*U–B*)–(*B–V*) and (*U–B*)–(*V–R*) diagrams. The system's primary component is classified as a metallic-line Am star. The absolute parameters of the components are estimated, and the binary is classified as a detached system with a subgiant: A0 V and K2 IV. EQ Ori has a faint physical companion, which causes the epochs of primary minimum to be systematically displaced with a period of about 30 years. The expected parameters of the distant companion are estimated. The system's components are at a pre-ZAMS evolutionary stage, with their age being 2×10^6 years. EQ Ori is thought to be a member of the Ori I association. © 2001 MAIK "Nauka/Interperiodica".

Key words: *stars—variable and peculiar*

INTRODUCTION

The variable EQ Ori (= BD $-3^{\circ}945 = 43.1929$, $m = 10.2$ – 13.3 pg; Sp: A0:) was discovered by Hoffmeister (1929), who established its variability type and determined the range of its light variations. Subsequent visual and photographic observations of the variable provided information about the binary's light curve and light elements. The General Catalog of Variable Stars (GCVS) gives the following ephemeris:

$$\text{Min I} = \text{JDH } 2\,431\,438.743 + 1^{\text{d}}.746057E.$$

The eclipse at primary minimum lasts for $0^{\text{p}}.12$, and a significant fading ($3^{\text{m}}.1$) takes place. Whitney (1957) noted that the period of EQ Ori was variable.

A spectrum of EQ Ori was taken with a resolution of 2.5 \AA on the ascending branch of its primary minimum using the 2.1-m Kitt Peak Observatory telescope, and a search for emission in the spectral range between H_{β} and H_{γ} was made (Kařtchuk and Honeycutt 1982; Kařtchuk *et al.* 1985). The search yielded no positive results. There are two observations of the variable at maximum light in Strömgren's four-color photometric system. These observations were carried out with the 40- and 90-cm Kitt Peak Observatory telescopes (Hilditch and Hill 1975) in an effort to determine its color.

Approximate photometric and absolute parameters of the close binary were determined by Gaposhkin (1953), Brancewicz and Dworak (1980), and Svechnikov and Kuznetsova (1990). The authors used unsolved

photographic light curves and relations between fundamental stellar parameters, including statistical relations.

OBSERVATIONS

We performed observations of EQ Ori as part of our program of research on close binaries in star-forming regions in the Ori I association (Zakirov 1996). Photoelectric (Johnson's *UBVR*) measurements of EQ Ori were obtained with the 1-m Maidanak Observatory telescope from September through November 1998. The observations were reduced by a standard method using monthly mean atmospheric extinction coefficients at Mount Maidanak (Zheleznyakova 1984). On clear nights and for a sufficient number of measurements of the standard star, the extinction coefficients were estimated by Bouguer's method. The magnitudes and colors of the comparison stars were determined relative to a photometric standard in Kapteyn's square area SA 95 (Landolt 1983). The coefficients of transformation from the instrumental photometric system to Johnson's system were calculated by the method of Hardy (1967). BD $-3^{\circ}953$ ($V = 6^{\text{m}}.983 \pm 0^{\text{m}}.001$, $U-B = -0^{\text{m}}.018 \pm 0^{\text{m}}.008$, $B-V = 0^{\text{m}}.475 \pm 0^{\text{m}}.002$, $V-R = 0^{\text{m}}.481 \pm 0^{\text{m}}.017$; Sp: F5) and BD $-3^{\circ}948$ were chosen as the comparison and check stars, respectively. Our observations of the close binary are summarized in Table 1.¹ A total of 445, 443, 445, and 440 measurements were obtained in *U*, *B*, *V*, and *R*, respectively. The light

¹ Table 1 is published in electronic form only and is accessible via ftp at [cdsarc.u-strasbg.fr/pub/cats/J](ftp://cdsarc.u-strasbg.fr/pub/cats/J) (130.79.128.5) or <http://cdsweb.u-strasbg.fr/pub/cats/J>.

* E-mail address for contacts: mamnun@astrin.uzsci.net

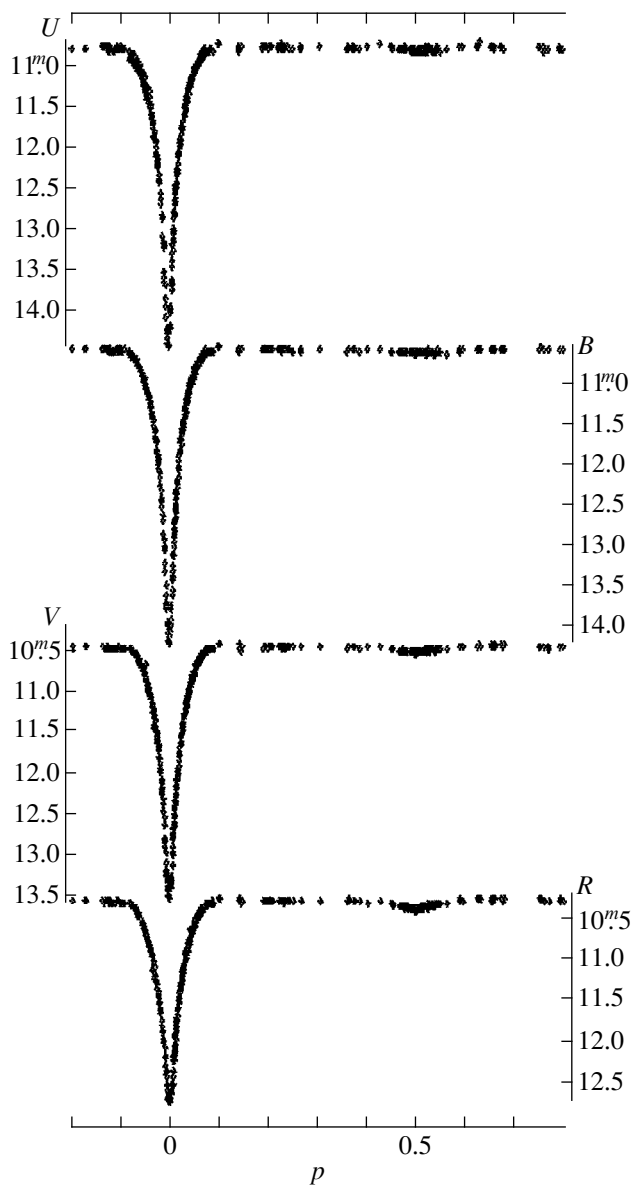


Fig. 1. Light curve of EQ Ori.

curves of EQ Ori are shown in Fig. 1. The magnitudes and colors of the variable at maximum and minimum are given in Table 2.

ORBITAL PERIOD

Whitney (1957) pointed to variability of the period of EQ Ori, but he failed to establish its pattern. Instability of the variable's orbital period is also noted in the

Table 2. Photometric parameters of the light curve for EQ Ori

Phase	V	U-B	B-V	V-R
Max	10.43	0.16	0.15	0.17
Min I	13.53	0.10	0.64	0.83
Min II	10.49	0.16	0.12	0.14

GCVS. We collected all the available observations of the close binary's minima and improved their ephemerides by least squares. The epochs of observed minima for EQ Ori were mostly published by Döppner (1962) and Dworak (1977); there are also numerous amateur observations of the variable in the BBSAG (Bedeckungsveränderlichen Beobachter der Schweizerischen Astronomischen Gesellschaft. Bulletin). We managed to find 110 epochs of minima, including our three determinations (JDH 2451 127.272, 2451 132.514, and 2451 134.259), in the interval of observations JD 2451 087–2451 134. We fitted the epochs of minima for EQ Ori by linear and parabolic laws and analyzed the $O-C$ residuals with a harmonic function. If the sum of $(O-C)^2$ obtained with a linear law is taken as 100%, then this sum obtained with a parabolic law is 80% and, given the harmonic term, 53%. Based on the least sum of $(O-C)^2$, we chose a linear law with a sinusoidal term:

$$\begin{aligned} \text{Min I} = & \text{JDH } 2445344.328 + 1^{\text{d}}7460579E \\ & - 0^{\text{d}}022\sin(338^{\circ}.5 + 0^{\circ}.058E), \\ & \pm 0.003 \pm 0.0000005 \pm 0.008. \end{aligned}$$

Deviations of the observed minima from the linear part of this ephemeris are shown in Fig. 2. There is a harmonic term with a period of about 30 years in the variable's light elements. Some points in the plot deviate greatly from this sinusoid. In the overwhelming majority of cases, the epochs of minima of the variable were determined from photographic and amateur visual observations. The exact epoch of maximum fading in eclipsing systems with sharp, deep minima lasting for no more than several tens of minutes is difficult to establish photographically, because the exposure time (typically 30–40 min) "smears" the accuracy of fixing minima (Zakirov 1993). For EQ Ori, the photoelectric duration of the eclipse at primary minimum is longer than its photographic duration by $0^{\text{m}}04$, and the fading is $0^{\text{m}}5B$ in B . During amateur visual observations with small instruments, EQ Ori can be completely unseen at primary minimum ($V = 13^{\text{m}}.5$). Of course, observers can interpolate their observations to the epoch of maximum fading from the ascending and descending branches of minima, but it is not known how accurately this is done.

Thus, we managed to establish that the variability of the orbital period of EQ Ori previously noted by other authors was attributable to the close binary's rotation about a common center of mass of the triple system.

LIGHT CURVE AND ITS SOLUTION

The light curve of EQ Ori is typical of Algols with an indistinct phase effect and a deep, sharp primary minimum. A secondary minimum is clearly seen only in the V and R light curves. The surprising thing is that the secondary minimum ($0^{\text{m}}1$ pg) was revealed by photographic observations. The shallow secondary mini-

mum suggests that the system's faint component is a late-type star. The eclipse duration at primary (DI) and secondary (DII) minima is approximately the same, $0^p.16$. Our observations yielded a slightly larger DI than did photographic data ($0^p.12$).

We solved all light curves by the direct method of Lavrov (1993), which is based on Russell-Merrill's rectifiable model. Limb darkening coefficients were taken from Rubashevskii (1985), who calculated them in Johnson's photometric system. Fourier decomposition of the light curves outside eclipse revealed a noticeable reflection effect in the V ($A_1 = -0.0114 \pm 0.0025$) and R ($A_1 = -0.0172 \pm 0.0033$) light curves. The light curves of EQ Ori were solved for circular and elliptical orbits. Minimizing the sum of the squares of deviations $(O-C)^2$ of normal points from a theoretical light curve is a major significance criterion for the data in solving the light curves of eclipsing variables. Minimization of the sum of $(O-C)^2$ gave rise to a large orbital eccentricity. Because of the shallow secondary minimum, the eccentricity e and the longitude of periastron ω can be determined only by solving the V - and R -light curves. We obtained $\omega = 86^\circ \pm 1^\circ$, i.e., an angle close to 90° , and $e = 0.37$. The duration ratio of secondary and primary minima can be easily estimated from the following simple relation at $i \approx 90^\circ$ (Martynov 1971):

$$\frac{DII}{DI} = \frac{1 + e \sin \omega}{1 - e \sin \omega}.$$

We found this ratio to be ~ 2 , which is not confirmed by observations. Applying the χ^2 test to the deviations of normal points at secondary minimum from a theoretical R light curve, which clearly exhibits this minimum, shows that this parameter for a circular orbit is a factor of 5 smaller than that for an elliptical orbit. Thus, we assumed the orbit of EQ Ori to be circular and derived its photometric orbital elements.

At primary minimum, a total eclipse of the brighter, but smaller (in radius) component takes place (the $G \rightarrow S$ hypothesis). Solving all light curves of EQ Ori indicates that the photometric phase in the middle of its primary minimum is $\alpha = 1.000$. We, therefore, assume that a total eclipse occurs at minimum, although this is not evident from the binary's light curve. The duration

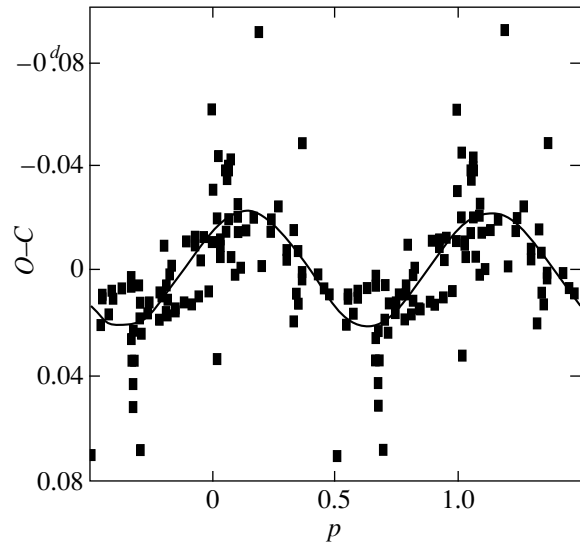


Fig. 2. Deviations of the epochs of primary minima for EQ Ori from a linear law.

of the total eclipse at primary minimum is short ($dI = 0^p.009 \pm 0^p.001$ or about 13 ± 1 min). The results of light-curve solution for EQ Ori are given in Table 3, where the last row lists the weighted mean deviations of normal points from a theoretical light curve. The quantities that refer to the cool and hot components are marked by the subscripts "c" and "h," respectively. The relative radii of the components are given in units of the orbital radius. Since the derived geometric elements of the close binary in all bands are similar, the sixth column gives their means. The last column lists the parameters obtained by Svechnikov and Kuznetsova (1990) from an analysis of the photographic light curve. A comparison of our photometric orbital elements with those of these authors shows that they differ by no more than 7%.

DISCUSSION

Table 4 gives the photometric parameters of each component calculated from the data of Tables 2 and 3. These values refer to the far, unlit sides of the components and thus reflect the true quantities. The necessary corrections can be determined by using the program of

Table 3. Photometric orbital elements for EQ Ori

Parameter	U	B	V	R	$\langle UBVR \rangle$	Svechnikov and Kuznetsova (1990)
r_c	0.264	0.260	0.256	0.259	0.260 ± 0.002	0.261
r_h	0.242	0.230	0.231	0.234	0.234 ± 0.003	0.249
x_c	0.95	0.90	0.70	0.60		
x_h	0.50	0.51	0.42	0.35		
i°	90.0	89.9	90.0	89.7	89.9 ± 0.1	90
L_c	0.046 ± 0.001	0.050 ± 0.001	0.074 ± 0.001	0.110 ± 0.001		0.09
σ^m	0.027	0.024	0.026	0.021		

Table 4. Photometric quantities for the components of EQ Ori

Component	V	$U-B$	$B-V$	$V-R$
Hot	10.51	0.16	0.12	0.13
Cool	13.25 ± 0.01	0.24 ± 0.02	0.59 ± 0.02	0.60 ± 0.02

Lavrov (1993), and the method of calculation is simple (Martynov 1971). The photometric quantities of the hot component were calculated with an accuracy higher than $0^m.01$. For an independent spectral classification of the components, we plotted their positions on two-color ($U-B$)–($B-V$) and ($U-B$)–($V-R$) diagrams (Fig. 3). The hot component of EQ Ori lies below the standard color curve for main-sequence (MS) stars and does not cross it when moving along the reddening line. This behavior is typical of metal-rich stars whose absorption lines produce an additional absorption of energy—the blanketing effect (Hack and Struve 1970; Straižys 1977; Wolff 1983). We will return to the components' spectra below after discussing their nature.

We estimated the expected absolute parameters of the components of EQ Ori by our method outlined in Zakirov (1996). The main point in this method is establishing the fundamental parameters of the primary star, which the hot component of the close binary is in our

case. The hot component mainly contributes to the close binary's light (see Table 4), and this star is characterized by the spectral type A0. Assigning the tabulated parameters of an A0 V star (Straizys 1982) to it, we calculated the same quantities for the cool component. The temperature of the cool component as inferred from Planck's formula in U is almost 10% higher than that in the remaining bands. We took into account the mean temperature of this component derived from the photometric orbital elements in BVR . Our search for the best correspondence of the cool component's parameters with allowance for the cosmic dispersion of these quantities to the same spectral type, radius, mass, and luminosity showed that the hot and cool components were A0 V and K2 IV stars (Table 5), respectively. For comparison, the table gives the absolute parameters of the components of EQ Ori estimated by other authors. The discrepancy in mass estimates for the cool component is largest: the value of Svechnikov and Kuznetsova (1990) is a factor of 3 smaller than that of other authors.

Our mass ratio of the close binary's components is $q = 0.82$, and their critical radii are $r_{h, \text{crit}} = 0.393$ and $r_{c, \text{crit}} = 0.356$ (Plavec and Kratochvil 1964). Both stars are deeply embedded in their Roche lobes. There is no

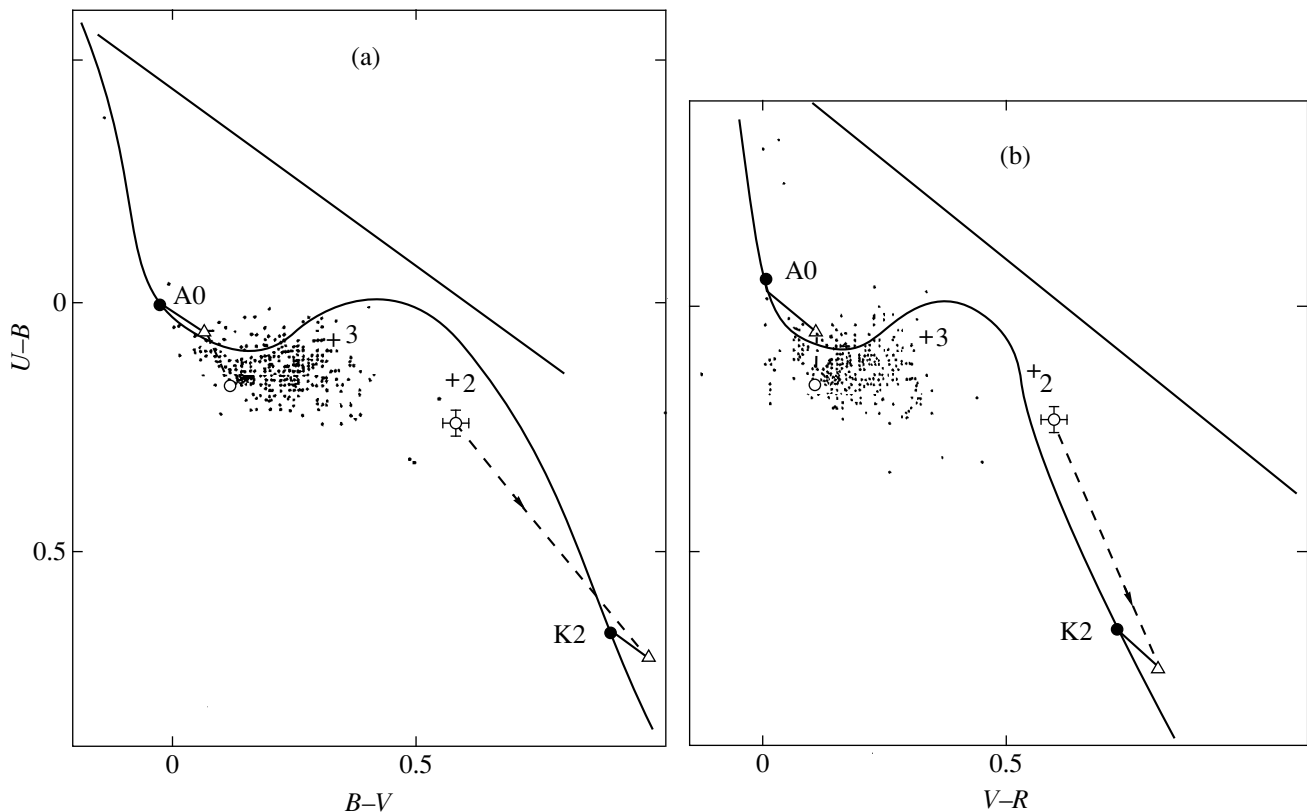


Fig. 3. Two-color diagrams: (a) ($U-B$)–($B-V$) and (b) ($U-B$)–($V-R$). Open circles are the components of EQ Ori (Table 4), filled circles are the components on the standard curves, triangles are the expected positions of the close binary's components, crosses are stars near the variable, and dots are Am stars.

Table 5. Expected absolute parameters of EQ Ori

Parameter	Hot component			Cool component		
	this paper	Brancewicz and Dworak (1980)	Svechnikov and Kuznetsova (1990)	this paper	Brancewicz and Dworak (1980)	Svechnikov and Kuznetsova (1990)
M/M_{\odot}	2.24	2.87	2.4	1.83	1.90	0.62
R/R_{\odot}	2.29	1.88	2.2	2.53	2.14	2.3
M_V	0.72		0.85	3.46		3.0
T, K	9600	9640		4860	5550	
Spectral type	A0 V	A0	A0	K2 IV		G2 IV

mass transfer in the system, and the orbital period has been constant for six decades. EQ Ori belongs to detached systems, which consist of a MS star and a subgiant.

In two-color diagrams, the hot component of EQ Ori exhibits an ultraviolet deficit, $\delta(U-B) = 0^m.10$ (Fig. 3), characteristic of metallic-line Am stars (Straizys 1977; Wolff 1983). On the same color diagrams, we plotted the positions of Am stars determined photometrically (Jaschek and Jaschek 1957; Mendoza *et al.* 1978). The blanketing effect on $B-V$ causes this color to decrease, on the average, by $0^m.07$ (Hack and Struve 1970). In the $B-V$ range $0^m.1-0^m.2$, the mean ratio $\delta(U-V)/\delta(B-V) = 2.4 \pm 0.4$ (Gomez *et al.* 1981) [the differences $\delta(U-V) = (U-V)-(U-V)_0$ and $\delta(B-V) = (B-V)-(B-V)_0$ if the star undergoes no interstellar extinction]. Allowance for blanketing of the close binary's hot component yields the correction $\delta(U-B) = -0^m.10 \pm 0^m.03$; its corrected $U-B = 0^m.06 \pm 0^m.03$ and $B-V = 0^m.05 \pm 0^m.03$ (we took a formal error of $\pm 0^m.03$ for $B-V$). The new position of the hot component is marked in Fig. 3 by a triangle. When moving along the reddening line, the star crosses the standard curves at points near A0, in complete agreement with its spectral classification. The color excess of the hot component is $E_{B-V} = 0^m.07$, and the visual absorption is $A_V = 0^m.23$ for $R = 3.36$ (Straizys 1977). The distance modulus for the close binary is $9^m.3$. Our estimate of the distance to the variable matches that of Brancewicz and Dworak (1980).

The position of the cool component in the two-color diagrams does not correspond to its expected spectral type K2 IV (the notation for the cool component in Fig. 3 is the same as that for the hot component). This may be attributable to the star's unusual spectral energy distribution. The star's spectrum at primary minimum, when only the cool component is seen, would be informative in interpreting the nature of the faint component.

The fact that one of the components of EQ Ori belongs to subgiants suggests that the star is either at a pre-MS or post-MS evolutionary stage. We studied the positions of the close binary's components in the Hertzsprung–Russell diagram constructed for moderate-mass single stars evolving toward and away from the MS (Maeder 1976; Palla and Stahler 1993). Having

analyzed these diagrams, we managed to establish that the close binary's components evolve toward the ZAMS (Fig. 4). The system's age is estimated to be 2×10^6 years. We estimated the gravitational contraction time for pre-ZAMS moderate-mass ($M_* < 8M_{\odot}$) stars by using the formula (Masevitch and Tutukov 1988)

$$\tau \approx 5 \times 10^7 (M_{\odot}/M_*)^{2.5} \text{ years.}$$

The hot and cool components of EQ Ori will reach the ZAMS in 7×10^6 and 1.1×10^7 years, respectively. The massive component of EQ Ori was classified as an Am star. Stars of this class have previously been discovered in several OB associations and in open clusters with ages $\geq 10^6$ years (Hack and Struve 1970; Abt 1979).

As was shown above, EQ Ori is a triple system that rotates about a common center of mass with a period of

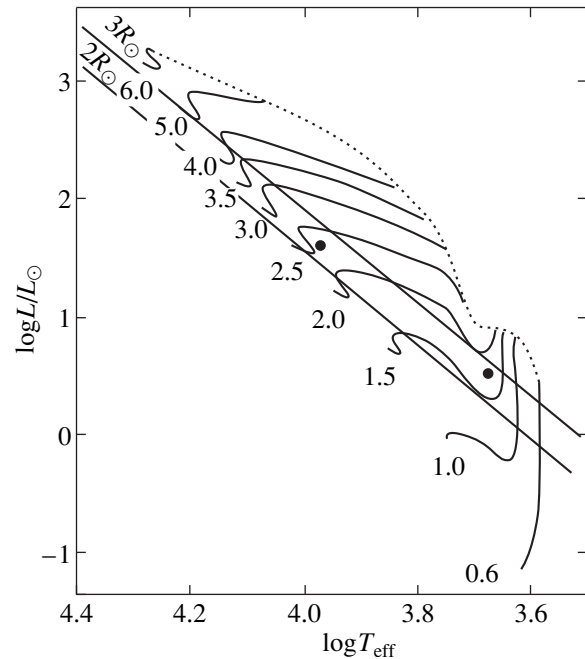


Fig. 4. Positions of the components of EQ Ori in the Hertzsprung–Russell diagram constructed for single stars from the calculations of Palla and Stahler (1993). The numbers near tracks are stellar masses (in units of the solar mass); the circles mark the positions of the hot (upper) and cool (lower) components in the Hertzsprung–Russell diagram.

Table 6. Photometry of stars in the vicinity of EQ Ori

Star	BD	V	U-B	B-V	V-R	n	Q method*	E_{B-V}	$m-M$
1		$11^m.484 \pm 0.003$	$1^m.003 \pm 0.022$	$1^m.069 \pm 0.005$	$0^m.859 \pm 0.004$	12	K4	$0^m.02$	$4^m.5$
2		11.223 ± 0.002	0.158 ± 0.006	0.608 ± 0.003	0.565 ± 0.005	12	B8	0.71	8.8
3	-3°948	11.067 ± 0.003	0.074 ± 0.004	0.316 ± 0.002	0.302 ± 0.003	14	B9	0.39	9.3

* The Q method is the method of determining the spectral type of a star from its measured U-B and B-V color indices (Straizys 1977).

29.5 years. Let us estimate basic parameters of the distant component by using the so-called mass function (Martyunov 1947; Kopal 1959):

$$\frac{M^3 \sin^3 i'}{(M_h + M_e + M)^2} = \frac{a' \sin^3 i'}{P^2},$$

where M is the mass of the third body, i' is the orbital inclination of the triple system, a' is the semimajor axis of its orbit (in AU), and P is the orbital period of the entire system (in sidereal years). Suppose that the orbital planes in the triple system are coplanar, i.e., $i = i'$. Recall that i is the orbital inclination of the close pair. Assuming the orbit be circular, we can easily determine its radius from the amplitude of the light equation, (3.7 ± 1.5) AU. We find the companion's mass from the mass function to be $M/M_\odot = 1.2 \pm 0.5$. Taking the age of the distant companion to be equal to the age of the binary system, we find the star's radius and temperature from the Hertzsprung-Russell diagram constructed by Palla and Stahler (1993): $R/R_\odot = 2.2 \pm 0.5$ and $T = 4500 \pm 600$ K, respectively. We also calculated the apparent magnitude of this companion, $V = 14^m.0 \pm 1^m.5$. The error in the parameters of the distant companion proved to be large because of inaccurate determination of the amplitude of the light equation (signal-to-noise ratio = 2.8). The distant companion apparently does not contribute

appreciably to the total brightness, as it is even undetectable when searching for a third light with the program of Lavrov (1993). Interestingly, although a total eclipse takes place in the close binary, the brightness in the middle of its primary minimum is lower than the brightness of the cool component in all bands except for R.

There is a small group of stars of approximately the same brightness near the variable, which clearly stands out against a poor stellar background (Fig. 5). We performed photometry of these stars in an effort to find out whether this stellar grouping is real (Table 6). Star no. 3 served as the check star during the variable's observations. In the two-color diagrams, we plotted only two stars (Fig. 3), while the third star (no. 1) was a late-type star without any appreciable absorption. When moving along the reddening line, the stars cross the standard curves twice. If we chose earlier spectral types for these stars and estimated their distance moduli, then they would lie at approximately the same distance as the variable (Table 6).

As was pointed out above, EQ Ori is located in the large Ori I association, whose distance is 450 pc ($m - M = 8^m.4$). Given the cosmic dispersion of the star's absolute parameters, this distance modulus for the variable ($m - M = 9^m.3$) can be assumed to suggest that it lies in the association. The proper motions of EQ Ori are very low (Rözer and Bastian 1993), like those for physical members of the association (Parenago 1954). Taking into account the system's youth and the aforesaid, we expect EQ Ori to be at a pre-ZAMS evolutionary stage and is a physical member of the Ori I association.

CONCLUSION

The first photoelectric (UBVR) observations have been obtained for the eclipsing variable EQ Ori in the Ori I association. We refined the ephemeris of minima and found its periodicity with an amplitude of $0^d.022$ and a period of about 30 years. We determined basic photometric parameters of the close binary's light curve and solved all its light curves by Lavrov's direct method. Highly accurate photometric orbital elements were derived for EQ Ori. The absolute parameters of the components were estimated; the system consists of A0 V and K2 IV stars. The hot component was classified as an Am star, and the system's age is 2×10^6 years. There is no correspondence between the color indices

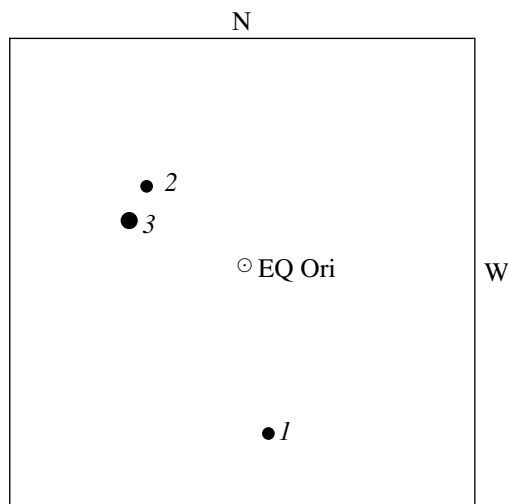


Fig. 5. Finding chart for EQ Ori. The field is $12' \times 12'$.

of the cool component and its estimated spectral type. We discovered a third, distant component in the system and estimated its parameters. The variable is expected to be a member of the association and is at a pre-ZAMS evolutionary stage.

ACKNOWLEDGMENTS

I wish to thank R.A. Fakhriddinov for help with the observations and the referees for constructive remarks, which improved the paper, and for the supplied epoch of minima of the variable. I am also grateful to S.Yu. Mel'nikov for help with the literature.

REFERENCES

1. H. A. Abt, *Astrophys. J.* **230**, 485 (1979).
2. H. K. Brancewicz and T. Z. Dworak, *Acta Astron.* **30**, 501 (1980).
3. M. Döppner, *Mitt. Veränder. Sterne*, No. 686 (1962).
4. T. Z. Dworak, *Acta Astron.* **27**, 151 (1977).
5. S. Gaposhkin, *Harv. Annals* **113** (2) (1953).
6. *The General Catalog of Variable Stars*, Ed. by P. N. Kholopov (Nauka, Moscow, 1985), Vol. II.
7. A. E. Gomez, S. Grenier, M. Jaschek, *et al.*, *Astron. Astrophys.* **93**, 155 (1981).
8. M. Hack and O. Struve, *Stellar Spectroscopy. Peculiar Stars* (Osservatorio Astronomico, Trieste, 1970).
9. R. W. Hilditch and G. Hill, *Mem. R. Astron. Soc.* **79**, 101 (1975).
10. H. Hardy, in *Astronomical Techniques*, Ed. by W. A. Hiltner (Univ. of Chicago Press, Chicago, 1962; Mir, Moscow, 1967), p. 157.
11. C. Hoffmeister, *Astron. Nachr.* **236**, 234 (1929).
12. M. Jaschek and M. Jaschek, *Astron. J.* **62**, 343 (1957).
13. R. M. Kaitchuk and R. K. Honeycutt, *Publ. Astron. Soc. Pac.* **94**, 532 (1982).
14. R. M. Kaitchuk, R. K. Honeycutt, and E. M. Schleger, *Publ. Astron. Soc. Pac.* **97**, 1178 (1985).
15. Z. Kopal, *Close Binary Systems* (Chapman and Hall, London, 1959).
16. A. U. Landolt, *Astron. J.* **88**, 439 (1983).
17. M. I. Lavrov, *Tr. Kazan. Gor. Astron. Obs.* **53**, 34 (1993).
18. A. U. Maeder, *Astron. Astrophys.* **47**, 389 (1976).
19. D. Ya. Martynov, *Variable Stars. Methods of Studying Variable Stars* (Gostekhizdat, Moscow, 1947), Vol. 3, p. 464.
20. D. Ya. Martynov, in *Eclipsing Variable Stars*, Ed. by V. P. Tsesevich (Nauka, Moscow, 1971), p. 155.
21. A. G. Masevich and A. V. Tutukov, *Stellar Evolution: Theory and Observation* (Nauka, Moscow, 1988).
22. V. E. E. Mendoza, T. Gómez, and S. González, *Astron. J.* **83**, 606 (1978).
23. F. Palla and S. W. Stahler, *Astrophys. J.* **418**, 414 (1993).
24. P. P. Parenago, *Tr. Gos. Astron. Inst., Mosk. Gos. Univ.* **25**, 3 (1954).
25. M. Plavec and P. Kratochvil, *Bull. Astron. Inst. Czech.* **15** (5), 171 (1964).
26. S. Rözer and U. Bastian, *PPM Star Catalogue: Position and Proper Motions* (Astron. Rechen. Inst., Heidelberg, 1993), Vol. 3, p. 1.
27. A. A. Rubashevskii, *Byul. Akad. Nauk Gruz. SSR, Abastumskaya Astrofiz. Obs.* **58**, 389 (1985).
28. V. Straizys, *Multicolor Stellar Photometry* (Mokslas, Vilnius, 1977).
29. V. Straizys, *Metal-Poor Stars* (Mokslas, Vilnius, 1982).
30. M. A. Svechnikov and É. F. Kuznetsova, *A Catalog of Approximate Photometric and Absolute Elements for Eclipsing Variable Stars* (Ural'skiĭ Gos. Univ., Sverdlovsk, 1990).
31. B. S. Whitney, *Astron. J.* **62**, 371 (1957).
32. S. C. Wolff, *The A-Type Stars: Problems and Perspectives* (NASA, Washington, DC, 1983).
33. M. M. Zakirov, *Kinematika Fiz. Nebesnykh Tel* **9** (1), 42 (1993).
34. M. M. Zakirov, *Pis'ma Astron. Zh.* **22**, 664 (1996) [*Astron. Lett.* **22**, 593 (1996)].
35. A. I. Zheleznyakova, *Astroclimate and the Efficiency of Telescopes* (Nauka, Leningrad, 1984), p. 55.

Translated by V. Astakhov

Hipparcos Trigonometric Parallaxes and the Distance Scale for Open Star Clusters

A. V. Loktin* and G. V. Beshenov

Astronomical Observatory, Ural State University, pr. Lenina 51, Yekaterinburg, 620083 Russia

Received April 3, 2000; in final form, September 29, 2000

Abstract—Hipparcos trigonometric parallaxes are used to estimate the distances to the maximum possible number of open star clusters (OSC); distance moduli are estimated for 45 clusters with maximum heliocentric distances of about 1000 pc. The latter value can serve as an estimate of the limit to which it still makes sense to use Hipparcos trigonometric parallaxes to determine the distances to small groups composed of 6–10 sufficiently bright stars. A systematic correction to the distance moduli of clusters from the homogeneous catalog of OSC parameters (Loktin *et al.* 1997, 2000) is estimated, which turns out to be independent of the cluster age. © 2001 MAIK “Nauka/Interperiodica”.

Key words: *open star clusters—distance determination*

INTRODUCTION

The determination of trigonometric parallaxes for a large number of relatively faint stars from the Hipparcos satellite radically changed the situation with establishing a reliable distance scale for open star clusters (OSCs), which provides a basis for the Galactic distance scale. Until recently, the OSC distance scale has been essentially based on the Hyades distance estimated by using various modifications of the moving-cluster method. However, because of a metal overabundance in the Hyades stars, the complex problem of allowing for the effect of deviations in chemical composition on the location of the Hyades main sequence arises. Hipparcos data allowed the distances to about twenty OSCs of different ages to be estimated [see, e.g., Robichon *et al.* (1999) and references therein] by using a method that required no allowance for the deviation of the chemical composition of cluster stars from the solar one. The wide age range of clusters with measured parallaxes makes it possible to directly investigate the reliability of the distance scale without resorting to ZAMS construction by cluster main-sequence fitting.

In the summer of 1999, a group of researchers from the Astronomical Observatory of the Ural State University completed their work on the second version of the Homogeneous Catalog of Open Star Cluster Parameters (Loktin *et al.* 1997, 2000). This paper appeared, because it was necessary to check the reliability of the distance scale of this catalog. We set the following objectives:

1. Determining the distances to the maximum possible number of OSCs with different ages by using Hipparcos trigonometric parallaxes.
2. Estimating the errors in the ZAMS location over the widest possible ranges of absolute magnitude, particularly in the range $M_V \leq -1^m.0$, which is critical for determining the distance moduli and ages of young OSCs.
3. Determining the corrections to the OSC distance scale of the “Homogeneous Catalog.”
4. Estimating the limit to which Hipparcos parallaxes can still be used to determine the distances to small (6 to 10 objects) groups of stars.

ANALYSIS OF THE TRIGONOMETRIC PARALLAXES OF OSC STARS

To achieve the above objectives, we used a sample that included all clusters from the “Homogeneous Catalog” with distance moduli less than $10^m.1$ and containing at least ten stars brighter than $V = 11^m.0$ in the color-magnitude diagram (below referred to as the HR diagram) while exhibiting a well-defined main sequence. Hipparcos proper motions and a photometric criterion based on Hipparcos B and V magnitudes (star positions relative to the main sequence and the giant branch in the HR diagram) were used as the membership criterion to separate cluster members. To distinguish the maximum possible number of cluster members, we analyzed wide regions with diameters from $5^\circ.5$ for the Hyades to $2^\circ.5$ for the most distant clusters of the sample.

The cluster distances were estimated as follows. For each cluster, we constructed the frequency distribution of trigonometric parallaxes for its probable members,

* E-mail address for contacts: Alexander.Loktin@usu.ru

and the position of the maximum of this distribution (mode) served as an estimate of the cluster trigonometric parallax. In our case, the mode of the distribution was chosen to estimate the parallax of the cluster as a whole, because the distribution of trigonometric parallaxes for cluster stars is generally asymmetric. The latter stems from the fact that the trigonometric parallax is nonlinearly related to the object distance.

To estimate the error of the mode, for clusters with more than 30 members, we broke down the sample into three equal parts and determined the positions of the maxima for the three distributions. An estimate of the variance of these three positions of the maxima was used as the error in the mode of the entire distribution. Alternatively, for clusters with less than 30 members, an estimate of the sample variance of the mean over the distribution was used as the error in the cluster trigonometric parallax. If the parallax distribution of cluster members exhibited no distinct maximum, then the cluster was excluded from the sample.

Figure 1 shows the frequency distributions of trigonometric parallaxes for probable members of three OSCs. The third cluster (Cr 70) is shown to illustrate the possibility of determining the distances to distant clusters from Hipparcos data: the parallax distribution for this cluster exhibits a distinct maximum. In principle, the cluster distances can be estimated from the modes of distance distributions, but it is better to use the distributions of parallaxes, because they are determined directly.

Note that the frequency distribution of trigonometric parallaxes for Hyades stars is slightly asymmetric, in contrast to the distance distribution for these stars shown in Fig. 2. The asymmetry of the parallax distribution is probably caused by selection: the number of more distant stars is underestimated, because the catalog completeness falls rapidly with distance for stars with V magnitudes fainter than 9^m . The second cause of the possible asymmetry is an increase in the mean errors of distance estimates with the increasing distance to objects itself. These effects necessitate abandoning the calculation of the sample mean (of both the distance and the parallax) when estimating the Hyades distance modulus. The mode of the distribution is also slightly affected by the asymmetry, but to a considerably lesser extent. In any case, it should be noted that the Hyades distance estimated from our data might be slightly underestimated.

The Pleiades cluster is of particular interest. The trigonometric parallaxes for this cluster yield a distance modulus that is appreciably smaller than its value obtained photometrically (Robichon *et al.* 1999). Note that the trigonometric-parallax distribution for the Pleiades stars (Fig. 1) clearly exhibits a secondary maximum, which gives a distance estimate that is in considerably better agreement with the photometric distance modulus (see the table). Narayanan (1999) found spatial correlations between the errors of Hipparcos trigo-

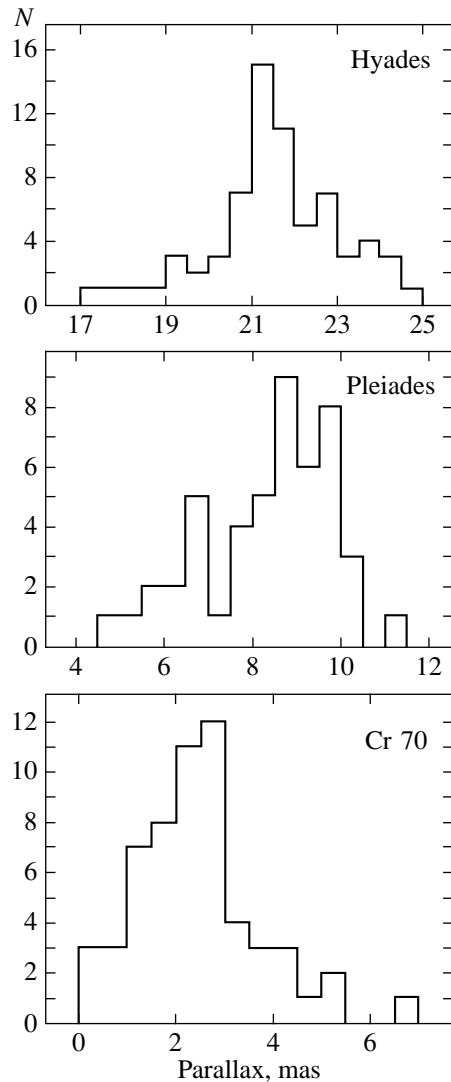


Fig. 1. The frequency distributions of trigonometric parallaxes for probable members of three open clusters.

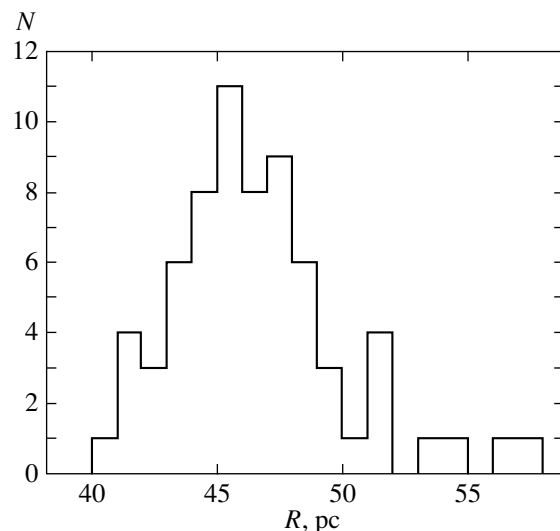


Fig. 2. The frequency distribution of distance estimates (R) for probable members of the Hyades cluster.

OSC distance moduli

No.	Cluster	$(V_0 - M_V)_\pi$	σ_π	$(V_0 - M_V)_{ph}$	σ_{ph}	$\log t$	N
1	Hyades	3.357	0.015	3.420	0.052	8.896	33
2	Pleiades	5.284	0.094	6.035	0.200	8.131	20
	Pleiades	5.874	0.094	6.035	0.200	8.131	9
3	Coma	4.737	0.042	5.063	0.050	8.652	13
4	α Per	6.209	0.061	6.504	0.047	7.854	25
5	Praesepe	6.202	0.114	6.507	0.141	8.863	16
6	IC 2391	5.827	0.076	6.340	0.049	7.661	12
	IC 2391	7.089	0.165	6.340	0.049	7.661	7
7	IC 2602	5.797	0.023	6.179	0.020	7.507	14
8	NGC 7092	7.258	0.007	7.721	0.079	8.445	14
9	Cr 135	7.204	0.091	7.649	0.200	7.407	12
10	NGC 2232	7.803	0.104	7.987	0.200	7.727	9
11	NGC 6475	7.287	0.143	7.549	0.109	8.475	21
12	NGC 6633	8.174	0.167	8.032	0.200	8.629	22
13	Cr 359	7.188	0.184	7.136	0.200	7.506	5
14	NGC 752	8.493	0.232	8.450	0.140	9.050	6
15	Cr 69	8.150	0.190	8.377	0.200	7.050	11
16	NGC 2516	7.879	0.018	8.213	0.129	8.052	16
17	Cr 140	7.706	0.110	8.183	0.072	7.548	16
18	Cr 173	7.773	0.386	8.277	0.200	7.142	13
19	Ros 5	8.785	0.275	8.100	0.200	7.832	13
20	Tr 10	7.828	0.033	8.173	0.185	7.542	16
21	Cr 70	8.080	0.142	8.091	0.200	6.980	35
22	Ru 98	9.710	0.310	8.622	0.200	8.508	11
23	NGC 2422	8.570	0.160	8.604	0.060	7.861	12
24	NGC 2547	8.395	0.158	8.399	0.014	7.557	18
25	Cr 132	8.460	0.250	8.330	0.200	7.080	16
26	δ Lyr	7.311	0.126	8.110	0.200	7.731	15
27	NGC 2451	7.884	0.287	7.562	0.412	7.648	15
28	NGC 3532	9.910	0.370	8.587	0.130	8.492	17
29	Bo 14	9.883	0.452	8.964	0.200	6.996	11
30	NGC 2395	8.908	0.323	8.701	0.200	9.070	8
31	IC 2395	9.344	0.133	9.360	0.200	7.220	9
32	NGC 7160	9.830	0.290	9.630	0.020	7.280	15
33	Cr 121	8.810	0.200	9.040	0.200	7.050	27
34	NGC 2169	9.270	0.240	10.260	0.080	7.070	10
35	NGC 2168	10.086	0.389	9.720	0.180	7.980	9
36	NGC 2264	8.120	0.120	9.180	0.130	6.950	8
37	NGC 2301	9.440	0.330	9.860	0.030	8.220	12
	NGC 2301	9.560	0.360	9.860	0.030	8.220	10
38	NGC 6281	9.580	0.292	8.707	0.243	8.497	6
39	NGC 3114	9.445	0.296	9.950	0.200	8.090	9
40	NGC 6530	9.005	0.255	10.740	0.200	6.870	7
41	NGC 1960	8.854	0.311	10.660	0.200	7.470	8
42	IC 348	8.303	0.092	8.080	0.257	7.641	6
43	NGC 2323	8.961	0.205	9.990	0.350	8.100	11
44	NGC 6025	10.736	0.209	9.550	0.090	7.890	4
45	NGC 6087	9.375	0.377	9.910	0.080	7.980	6

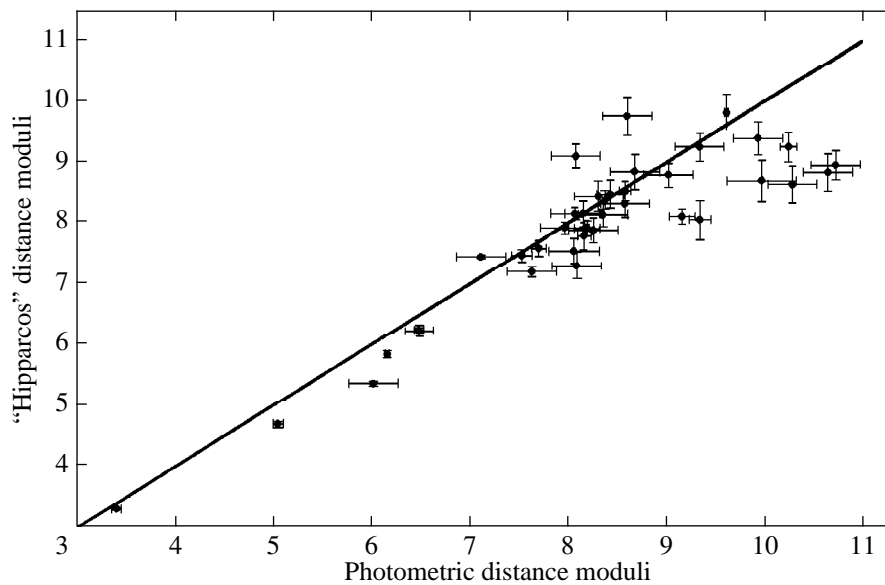


Fig. 3. Comparison of the OSC distance moduli calculated by using trigonometric parallaxes and by the photometric method.

nometric parallaxes and gave a new estimate of the Pleiades distance modulus: $5.^m58 \pm 0.18$. However, this estimate is also far from the photometric distance modulus (see the table). The possible causes of the Pleiades discrepancy should probably be sought more thoroughly in Hipparcos measurements. This was pointed out by Pinsonneault *et al.* (1998), who concluded that the Hipparcos trigonometric parallaxes contained small systematic errors on scales of the order of 1° .

There are two more clusters, IC 2391 and NGC 2301, with two maxima in the parallax distributions of their members, so the primary maximum is difficult to choose. The summary table of results for the Pleiades and for the two clusters mentioned above gives two estimates of the distance modulus for each of them, and these three clusters were included in the subsequent analysis twice with half the weight in each case.

The columns of the table provide the following data: cluster numbers and names; distance moduli, as estimated from trigonometric parallaxes, and the corresponding errors; photometric estimates from the ‘‘Homogeneous Catalog’’ and the corresponding errors; logarithms of the cluster age and the number of stars used to determine the distances based on trigonometric parallaxes.

CLUSTER DISTANCE MODULI

Figure 3 compares the distance moduli estimated from Hipparcos trigonometric parallaxes with the photometric distance moduli from the ‘‘Homogeneous Catalog’’ (Loktin *et al.* 1997). To determine the corrections to the distance moduli from the ‘‘Homogeneous Catalog’’ and to reveal a possible dependence of these corrections on the age (which is related to the absolute

magnitudes of the brightest main-sequence stars), we consider the regression model

$$(V_0 - M_V)_\pi = a + b(V_0 - M_V)_{\text{ph}} + c \log t. \quad (1)$$

Here, $(V_0 - M_V)_\pi$ is the distance modulus estimated from Hipparcos parallaxes, and $(V_0 - M_V)_{\text{ph}}$ is the distance modulus from the ‘‘Homogeneous Catalog’’; the logarithms of ages $\log t$ were also taken from this catalog. A regression analysis of this relation is difficult to perform directly, because the standard least-squares method yields unbiased estimates for the regression model coefficients only in the case of zero errors in the factors [see, e.g., Vuchkov *et al.* (1987) for more details]. The methods of determining the corresponding corrections to the coefficient estimates have been well developed for two-factor models and errors in the factor that do not depend on the factor values. In our case, however, the errors in the factors and responses generally increase with distance modulus (see Fig. 3). It is difficult to use numerical simulations to model the behavior of the errors because of the difficulty involved in determining the parameters of the distribution of distance errors calculated from trigonometric parallaxes of unequal accuracy. We therefore applied the following, perhaps artificial method. We first estimated the coefficients of model (1) for the entire sample: $a = -1.96 \pm 0.69$; $b = 0.991 \pm 0.026$, and $c = 0.23 \pm 0.07$ with the residual dispersion $\sigma = 0.^m55$, and then we gradually removed clusters with the largest residuals (one to three clusters) while solving the regression problem by least squares at each step. In this way, we artificially reduced the dispersions of the responses and factors, which gives hope for an insignificant bias of the final coefficient estimates. After removing the fifteen clusters with the largest deviation from the cluster relation, we obtained the following estimated for the coef-

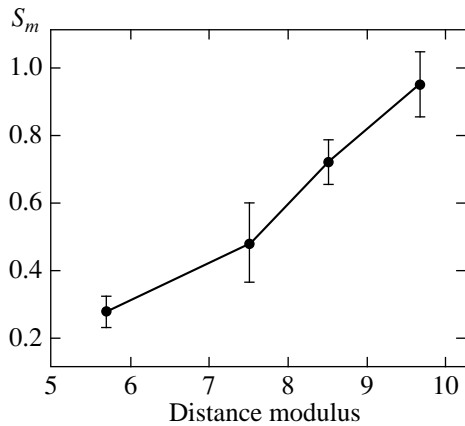


Fig. 4. Mean error in the distance modulus of a single star (S) as inferred from Hipparcos trigonometric parallaxes versus distance modulus.

ficients of model (1): $a = -0.58 \pm 0.31$; $b = 1.013 \pm 0.012$, and $c = 0.032 \pm 0.033$ with the residual dispersion $\sigma = 0''.28$ for the conditional equations. As the rms error of the coefficient of the age logarithm shows, the factor containing the age in model (1) proves to be statistically insignificant; i.e., the distance scale is generally the same for clusters of various ages. The statistical insignificance of this coefficient and the insignificant deviation of the coefficient b from unity allows us to use the same (for all clusters) weighted mean difference between the two series of distance-modulus estimates, $\langle (V_0 - M_V)_\pi - (V_0 - M_V)_{\text{ph}} \rangle = -0''.153 \pm 0''.072$, to determine the correction to the distances scale of the “Homogeneous Catalog.” To test the age independence of our OSC distance scale more reliably, we broke down our cluster sample into two parts. The first (young) group included all the clusters with $\log t < 8.0$ (29 objects), and the second (old) group included the remaining clusters (19 objects). The unequal division into groups stems from the fact that the old group contains such nearby clusters as the Hyades, the Coma, and the Praesepe with the most reliable distances. The mean distance-modulus difference is $-0''.13 \pm 0''.10$ and $-0''.20 \pm 0''.10$ for young and old clusters, respectively. As the derived errors of the mean show, the corrections differ insignificantly, so we may actually use the same correction of $-0''.153$ to the distance moduli of the clusters of all ages.

In Fig. 4, the mean error in the distance modulus (for a single star) is plotted against object distance. As we see from the figure, the error for a group of ten stars located at a distance of 1000 pc is, on the average, $\sim 0''.3$, which is close to the typical accuracy of the photometric distance moduli for poor OSCc. We can probably consider 1 kpc to be the limit for using Hipparcos trigonometric parallaxes for groups of stars, while this distance for single stars must be reduced by several times, depending on the required distance accuracy.

CONCLUSION

We have determined the distances to 45 OSCs by using Hipparcos trigonometric parallaxes. Data on the clusters for which more or less reliable distance estimates were obtained here will be included in the next version of the “Homogeneous Catalog” and will be used to estimate the mean OSC distance moduli. Note that Narayanan and Gould (1999) have recently estimated the Hyades distance modulus by the geometric method, $3''.34 \pm 0''.02$. This value virtually matches our distance modulus, $3''.357 \pm 0''.015$, so the agreement between the moving-cluster and trigonometric-parallax methods is excellent.

To construct an accurate distance scale, an age-independent correction of $-0''.153$ should be applied to the distance moduli from the “Homogeneous Catalog” (Loktin 1997, 2000). The OSC distance scale is apparently uniform, because no age dependence of the correction to the distance scale was found. Currently, this conclusion is being tested by determining the absolute magnitudes of O and B field stars using Hipparcos trigonometric parallaxes.

Hipparcos parallaxes can be used to determine the mean distances for groups of several tens of stars up to distances of 1 kpc. The plot shown in Fig. 4 can help estimate the number of stars needed to achieve the required distance accuracy or to estimate the accuracy of determining the mean distance, which might be expected for the available number of stars.

ACKNOWLEDGMENTS

This work was supported by the State Science and Technology Program “Astronomy.”

REFERENCES

1. The Hipparcos and Tycho Catalogues, ESA-SP1200, 1997.
2. A. V. Loktin, P. Zakharova, T. Gerasimenko, and L. Malisheva, *Baltic Astron.* **6**, 316 (1997).
3. A. V. Loktin, T. P. Gerasimenko, and L. K. Malysheva, *Astron. Astrophys. Trans.*, 2000 (in press).
4. V. K. Narayanan, *Astrophys. J.*, 1999 (in press).
5. V. K. Narayanan and A. Gould, *Astrophys. J.* **515**, 256 (1999).
6. M. H. Pinsonneault, J. Stauffer, D. V. Soderblom, *et al.*, *Astrophys. J.* **504**, 170 (1998).
7. N. Robichon, F. Arenou, J.-C. Mermilliod, and C. Turon, *Astron. Astrophys.* **345**, 471 (1999).
8. I. Vuchkov, L. Boyadzhieva, and E. Solakov, *Applied Linear Regression Analysis* (Finansy i Statistika, Moscow, 1987).

Translated by A. Dambis

An Astrometric Study of the Triple Star ADS 48

O. V. Kiyayeva*, A. A. Kiselev, E. V. Polyakov, and V. B. Rafal'skiĭ

Pulkovo Astronomical Observatory, Russian Academy of Sciences, Pulkovskoe sh. 65, St. Petersburg, 196140 Russia

Received February 14, 2000; in final form, January 9, 2001

Abstract—We analyze the series of relative positions of the hierarchical triple system ADS 48 ABF ($AB = 6''$, $AF = 327''$) obtained with the 26-inch Pulkovo refractor during 1961–1995 and measured with the Fantazia automated measuring system. A new relative orbit of pair AB is determined by the method of apparent-motion parameters using new observations and all the available astrometric and astrophysical data on this star, including its Hipparcos parallax. The new orbit for pair AB is reliably reconciled with all the new and previous observations of this star for the sum of the components' masses equal to $1.4M_{\odot}$. The Pulkovo observations (1961–1995) revealed a perturbation with a period of 15 years and an amplitude $\rho \sim 0''.01$, suggesting the presence of an unseen companion with a mass as large as $0.05M_{\odot}$. Since the oscillation amplitude is at a noise level, the orbit of the suspected companion cannot be determined. Assuming that stars A and B have the same mass, which corresponds to astrophysical data, we computed the parameters of apparent motion of component F relative to the center of mass of system AB and determined the family of orbits that satisfied the Pulkovo observations. All the computed orbits are steeply (more than 55°) inclined to the orbital plane of AB. The orbital motion of star F has been investigated for the first time. © 2001 MAIK “Nauka/Interperiodica”.

Key words: *multiple systems, orbit improvement, component motion parameter calculation*

INTRODUCTION

The visual binary ADS 48 AB has a long observational history. According to the WDS1996 catalog (Worley and Douglass 1996), the AB pair has been observed since 1876. In the 1960s two highly discrepant orbits have been computed for this pair by Guntzel-Lingner (1955)— $a = 6''.2$, $P = 362$ yr and Hoppmann (1964)— $a = 11''.7$, $P = 1507$ yr. If combined with the Hipparcos parallax ($0''.085$), the first orbit yields a total mass of $M_{A+B} = 3.0M_{\odot}$ for the two components, which is too high given the spectral type of the star. The second orbit yields $M_{A+B} = 1.1M_{\odot}$. Both orbits are significantly at variance with post-1975 observations. The third component (in terms of brightness) was observed in 1887, and it has never been measured ever since.

Table 1 gives basic data for the components of the system.

We took the coordinates, proper motions, spectral types, and magnitudes from the catalog of Gliese (1969); the parallax p_i , from the Hipparcos catalog, and radial velocities, from Tokovinin's (1990) catalog. We determined bolometric corrections (B.C.) according to Kulikovskii (1985), and we computed the component masses in the solar units from the mass-luminosity relation using the following formulas:

$$M_{\text{bol}} = 6.76 - 3.80 \log \mathcal{M}$$

for $M_{\text{bol}} > +7.5$ (components A and F),

$$M_{\text{bol}} = 4.62 - 10.03 \log \mathcal{M}$$

for $M_{\text{bol}} < +7.5$ (component B).

Anosova *et al.* (1987) compared the spectra of stars A, B, and F obtained with the 6-meter telescope of the Special Astrophysical Observatory of the Russian Academy of Sciences and found both A and B stars to have the same spectral type of dM0, implying a mass of $M_A = 0.53M_{\odot}$ for star A. It can therefore be concluded that stars A and B are of the same origin and nature.

The visual binary ADS 48 AB has been observed with the 26-inch Pulkovo refractor since 1961, and we, have published many papers dedicated to this object. Distant component F can also be seen in many plates taken under good observing conditions. The results of our relative-position measurements of all three components allowed us to include this stellar system into the list of stars with suspected unseen companions.

The AB pair proved to be a very promising object for the application of the technique of apparent-motion parameters (hereafter AMP), which was designed for computing binary orbits from short-arc observations (Kiselev 1989). This pair was therefore used as a prototype for most of the simulations performed to test the technique, and its orbit was computed several times (Kiselev and Kiyayeva 1980; 1988; Kiyayeva 1994).

Recall that to compute an orbit with the AMP technique, one must know five parameters of the apparent

* E-mail address for contacts: kiyayeva@gao.spb.ru

Table 1. Parameters of the star ADS 48

Component	α_{1950} δ_{1950}	SP	V	μ_x μ_y	p_t	V_r , km s $^{-1}$	B.C.	$\mathcal{M}/\mathcal{M}_\odot$
A	0 ^h 0.3 ^m 0.2 ^s	dK6	8.93	+0 [″] .877	0 [″] .0851	+0.8	−0.7	0.50
	+45°32′.2			−0.127	±27	±0.2		
B	0 03 02	dM0	8.97	+0.877	0.0851	−2.2	−1.2	0.53
	+45 32.1			−0.189	±27	±0.2		
F	0 02 32	dM2	9.89	+0.86	0.0870	−1.0	−1.5	0.47
	+45 30.6			−0.14	±14	±0.3		

relative component motion. These parameters include position (ρ , θ), relative velocity μ and its position angle Ψ , curvature radius ρ_c , relative radial velocity $V_r = (V_{rB} - V_{rA})/4.74$, and the trigonometric parallax p_t .

Here ρ and ρ_c are in arcsec; μ , in arcsec yr $^{-1}$; V_{rA} and V_{rB} , in km s $^{-1}$, and V_r , in AU yr $^{-1}$.

The following formula is used to compute the separation of the components (in AU) independently of V_r and p_t :

$$r^3 = k^2 \frac{\rho \rho_c}{\mu^2} |\sin(\Psi - \theta)|. \quad (1)$$

Here $k^2 = 4\pi^2 \mathcal{M}_{A+B}$ [AU 3 yr $^{-2}$] is the dynamical constant of astrocetric motion.

The projection condition and the energy integral for the physical pair imply that:

$$\rho/p_t \leq r \leq 2k^2/V^2, \quad (2)$$

where $V^2 = (\mu/p_t)^2 + V_r^2$.

Two uncertainties remain, the unknown parameters being (1) the total mass of the two components \mathcal{M}_{A+B} and (2) the sign of the inclination (angle β) of the radius-vector of the star with respect to the sky plane (the point is that only $\cos\beta$ can be confidently determined):

$$\cos\beta = \frac{\rho}{p_t r}, \quad \sin\beta = \pm\sqrt{1 - \cos^2\beta}. \quad (3)$$

Both uncertainties are easily resolvable if the old observations are available providing long enough time baseline. We select from our family of orbits the trajectory that fits the old observations best (Kiyaeva 1983), thereby constraining the total mass of the two components.

This work resulted from long-term observations and research. The necessity and topicality of this study stem from the fact that the new data allow a much more accurate orbit of the AB pair to be objectively computed. The Hipparcos catalog has been released giving for the

AB and F stars the parallaxes that differ appreciably from those hitherto adopted (0[″].094). In addition, the arc covered by homogeneous Pulkovo photographic observations, all of them made with the same telescope, has grown in length and now spans a time baseline of 34 years. We measured all 137 plates with the automatic Fantazia measuring complex using our original algorithms, which ensure minimum equipment error. The size of the arc and the accuracy of measurements proved to be sufficient to allow confident determination of the curvature radius at the center of the apparent orbit at epoch 1980.0. All procedures described by Kiyaeva (1985) and which we later refined yielded the same values for the curvature radius in what is by all means an extremely rare result. According to Tokovinin (1990), the relative radial velocity is equal to -3.0 ± 0.3 km s $^{-1}$.

DETERMINATION OF THE ORBIT OF THE AB PAIR

We used the Fantazia automatic complex to measure a total of 137 plates bearing images of stars A, B, and F. Our measurements thus yielded a total of 137 positions (ρ , θ) of star B relative to star A, 128 positions of star F relative to A, and 124 positions of star F relative to B. The annually-averaged positions are shown in Tables 2, 3, and 4,¹ which are presented in electronic form.

We performed astrometric reduction of our measurements using the so-called trail/scale method, which is detailed in the Introduction to the catalog of 200 visual double stars (Kiselev *et al.* 1988). No reference stars are required for this method, which uses diurnal-trail based orientation, a preset geometric scale, and allows for differential refraction. We measured 6 to 20 positions per plate. The mean single plate position errors, which are equal to 0[″].030, 0[″].053, and 0[″].054 for the AB, AF, and BF pairs, respectively, provide objective estimates of the mean observing conditions in Pulkovo

¹ Tables 2–4 are published in electronic form only and are available at ftp cdsarc.u-strasbg.fr/pub/cats/J (130.79.128.5) or at http://cdsweb.u-strasbg.fr/pub/cats/J.

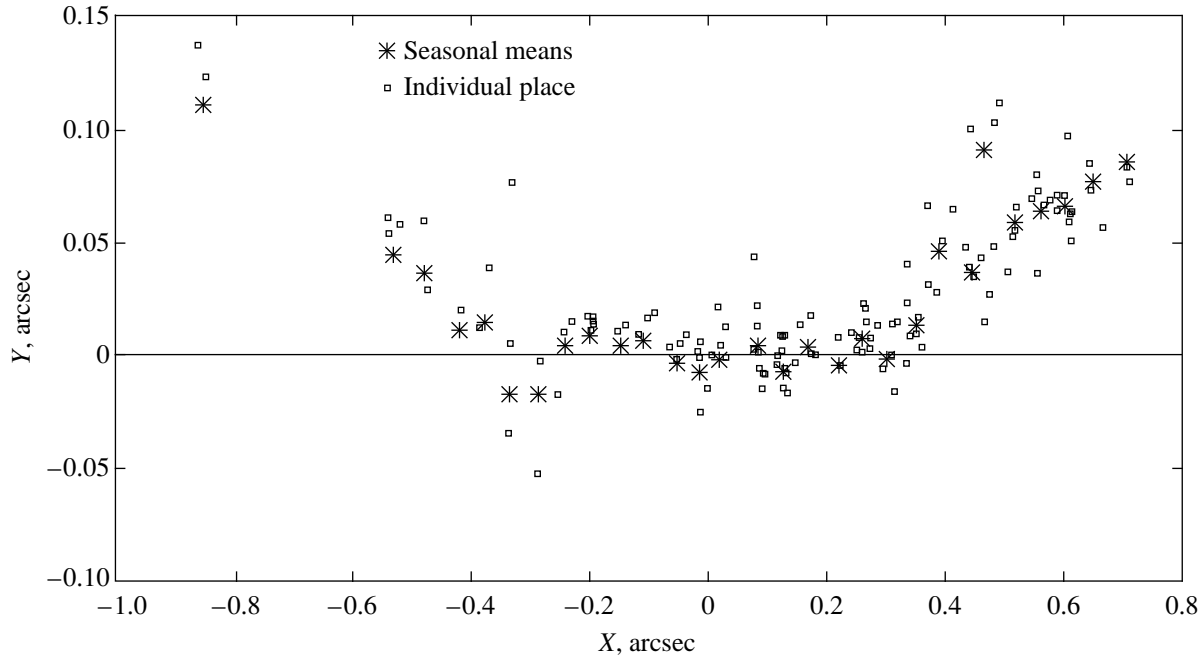


Fig. 1. Cartesian coordinates of star B in the rectangular reference frame. Here origin 0 determines the position at epoch 1980.0 and the X- and Y-axes are directed tangentially and normally to the star’s motion, respectively.

(the state of the atmosphere and tracking mechanism) for 15–20 min single-plate exposures. Naturally, residual refraction was stronger in the case of large separations (327") than in that of a close pair (6"). Thus, the single plate measurement error, as inferred from internal agreement, is 0".007 for AB pair and 0".012 for AF and BF pairs. The parameters of the apparent relative motion and the corresponding single-plate rms errors based on the external consistency checks of the entire data set are summarized in Table 5.

Here μ , Ψ , and ρ_c are computed using the following formulas:

$$\begin{aligned} \mu &= \sqrt{(\rho')^2 + (\rho\theta')^2}, \\ \Psi &= \theta + \pi/2 - \arcsin(\rho'/\mu), \\ \rho_c &= |\mu^3 / (\theta'(\mu^2 + \rho'^2) + \rho(\rho'\theta'' - \rho''\theta'))|. \end{aligned} \quad (4)$$

As is evident from Table 5, the inferred relative-motion parameters for the AB pair are very precise (in particular, our relative component motion is one order of magnitude more accurate compared to that listed in the Hipparcos catalog), thus testifying to the high quality of the computed orbit.

We now consider in more detail the determination of the curvature radius ρ_c of the apparent orbital arc of the AB pair. The point is that in the AMP method, ρ_c is one of the key parameters for computing the orbit and determining the total mass of the two stars. Figure 1 shows coordinates of star B in the tangent-normal reference frame whose origin coincides with the position of star B relative to star A at epoch 1980.0; the X and

Y axes are aligned tangentially and normally to the orbital motion, respectively. The deviations from the X-axis characterize the curvature of the observed orbital arc. As is evident from the figure, the observed arc is curved conspicuously and its curvature can be confidently inferred. We computed the curvature radius in three ways: (1) according to exact formula (4); (2) using iterations; and (3) fitting a circle to the observed arc. Plate measurements and annually-averaged positions yielded the following ρ_c values:

Table 5. Relative-motion parameters for epoch 1980.0

Pair	BA	FA	FB	FC
ρ	5".957 ±2	327".821 ±3	326".877 ±2	327".336 ±3
θ	173°.42 ±1	253°.782 ±2	254°.811 ±2	254°.296 ±2
μ	0".0459 yr ⁻¹ ±1	0".0174 yr ⁻¹ ±4	0".0283 yr ⁻¹ ±4	0".0055 yr ⁻¹ ±18
Ψ	250°.69 ±25	252°.6 ±6.7	67°.6 ±4.0	59°.7 ±18.2
ρ_c	2".9 ±2	–	–	–
$\sigma_1(\rho)$	0".021	0".040	0".040	–
$\sigma_1(\theta)$	0°.136 (0".014)	0°.04 (0".22)	0°.04 (0".23)	–

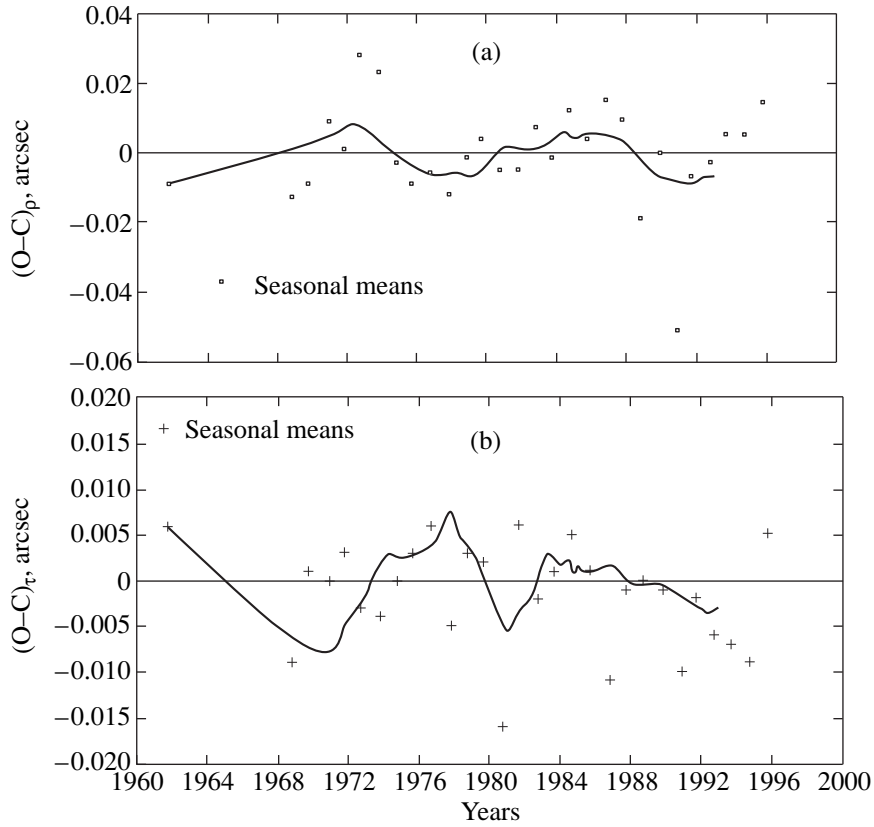


Fig. 2. The orbit of the AB pair compared to the observations made from 1961 through 1995 with the 26-inch Pulkovo refractor: (a) ρ and (b) τ . Here $\Delta\tau = \rho\Delta\theta/57.3$. The line shows the smoothed behavior of residuals.

annually-averaged positions of plates

	Plates Annually	Averaged positions
1	$2''.76 \pm 0''.14$	$2''.94 \pm 0''.16$
2	2.84 ± 0.20	2.99 ± 0.23
3	2.60 ± 0.18	2.79 ± 0.18

We finally adopted the mean value of $\rho_c = 2''.9 \pm 0''.1$ based on normal (annually-averaged) places, which we considered to be the most accurate.

We then used the above initial data and previously-determined component masses to compute the AMP orbit of the AB pair. We adopted for our binary the Hipparcos parallax of the F component ($0''.087$), which we consider to be more accurate than those of the other two components. Old observations fit well the orbits computed for $\mathcal{M}_{A+B} \geq 1.4\mathcal{M}_\odot$ without imposing any reasonable upper mass limit: increasing the mass to $5\mathcal{M}_\odot$, which looks unrealistic in the case considered, changes the resulting ephemeris insignificantly. The inferred lower limit $\mathcal{M}_{A+B} = 1.4\mathcal{M}_\odot$ somewhat exceeds the luminosity-based total mass of $1.1\mathcal{M}_\odot$. Astrometric and astrophysical data can, therefore, be best reconciled by adopting the minimum allowed total mass of $1.4\mathcal{M}_\odot$ that is still consistent with observations. Below, we give

the AMP orbital elements of the AB pair (Table 5) for the adopted $\mathcal{M}_{A+B} = 1.4\mathcal{M}_\odot$, $\beta = +26^\circ$, $p_t = 0.087''$, and $\Delta V_r = -3.0 \text{ km s}^{-1}$

a	P	e	ω	i	Ω	T_p
$6''.21$	$509''.65$	0.22	$267^\circ.2$	$54^\circ.9$	$13^\circ.5$	$2115''.80$
$\pm.77$	± 96.99	$\pm.04$	± 27.4	± 2.4	± 2.3	± 123.47

Here, the ascending node and the longitude of periastron are determined unambiguously, whereas the orbital inclination is based on the usual convention. The errors of the orbital elements are based on those of the initial data. The rms residuals for a single Pulkovo observation (plate) are equal to $\pm 0''.018$ and $\pm 0''.014$ in the radial and tangential directions, respectively. As is evident from a comparison of these errors with those of the polynomial fit (Table 5), the orbit fits the Pulkvo data somewhat better than the second-order polynomial.

In Fig. 2 we compare the orbital ephemeris against the Pulkovo observations (normal places) in ρ and τ ($\Delta\tau = \rho\Delta\theta/57.3$). The rms residuals of normal places are equal to $0''.014$ and $0''.006$ in the radial and tangential directions, respectively. The continuous line shows the smoothed behavior of five-year sliding average residuals.

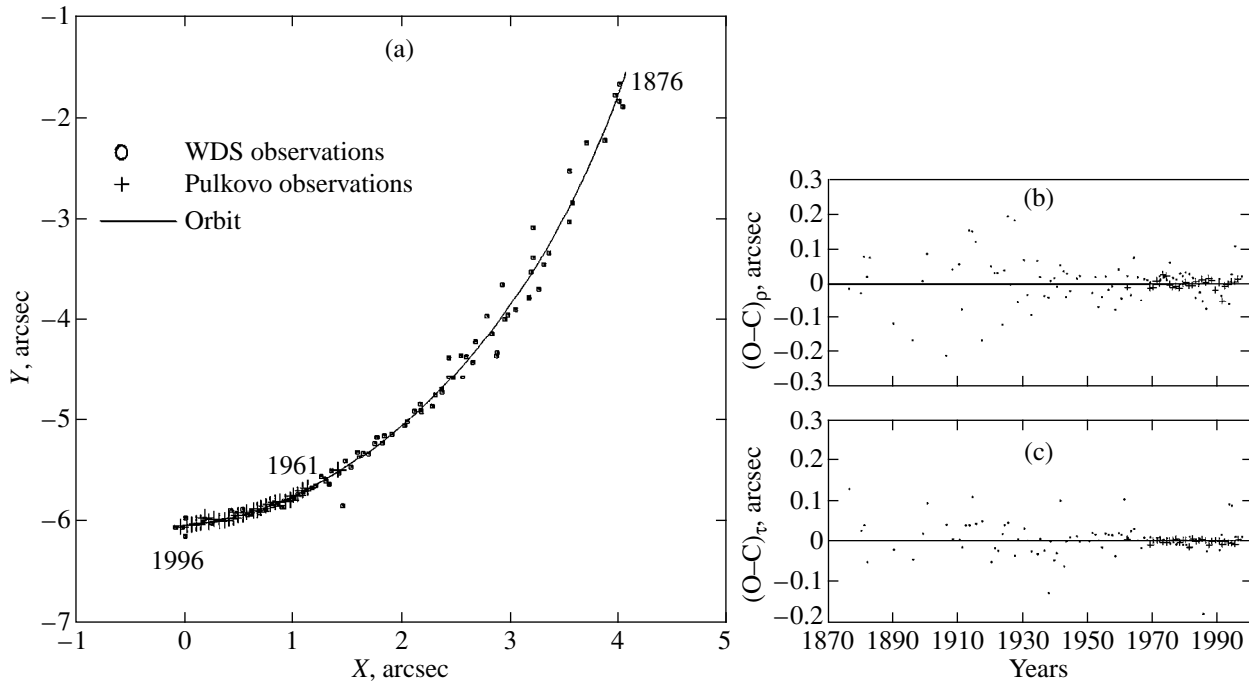


Fig. 3. The orbit of the AB pair compared to the sky-plane observations from 1876–1996: (a) ρ and (b) τ . Here $\Delta\tau = \rho\Delta\theta/57.3$.

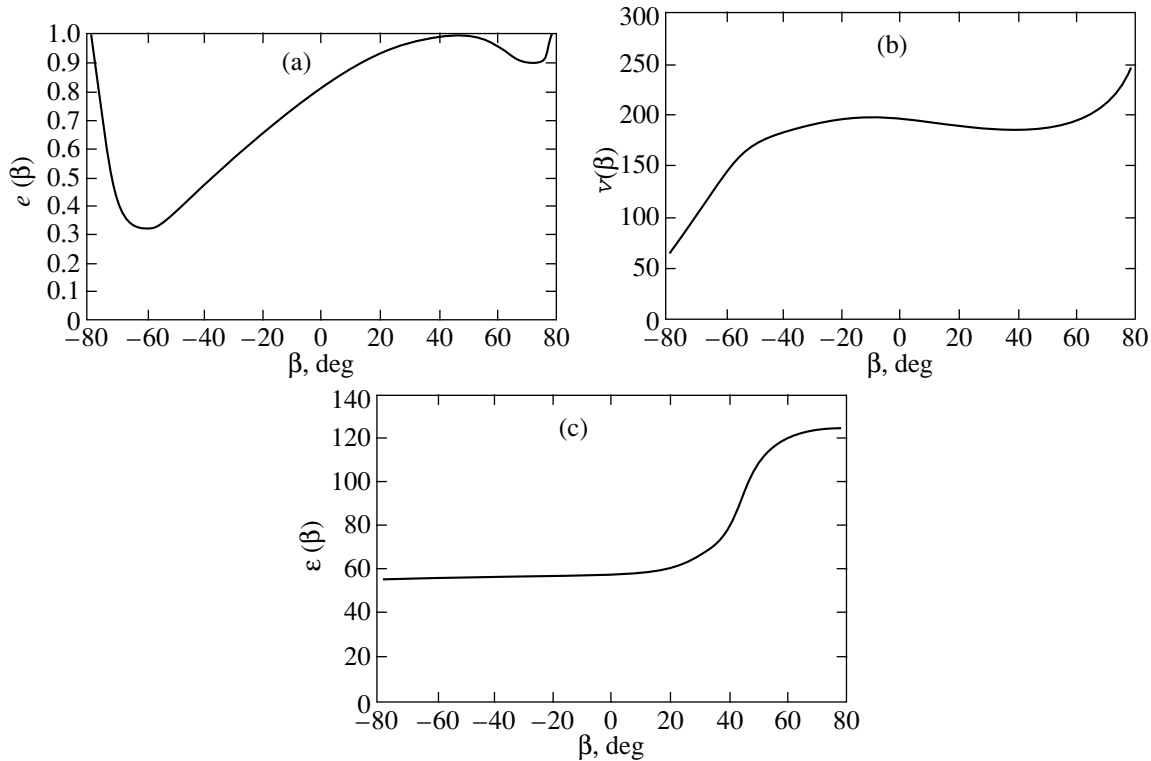


Fig. 4. The parameters of the family of orbits of the (AB)F pair. Eccentricity (a), true anomaly (b), and the angle between the (AB)F and AB orbital planes (c) plotted as functions of parameter β .

In Fig. 3, we compare the orbital ephemeris against all available observations, which are shown as annually-average positions separately for those based on WDS catalog observations and those based on Pulkovo measurements.

It is evident from the figure that, on the whole, the orbit fits all observations satisfactorily. Pulkovo observations show well-defined oscillations in ρ with a period and amplitude of 15 years and $0''.01$, respectively. If due to an unseen companion, these oscillations

Table 6. Family of orbits of star F relative to the AB pair

β	a	P , year	e	ω	i	Ω	T_p , year	ϵ
$-78^\circ 3$	–	–	1.00	$191^\circ 4$	$87^\circ 6$	$62^\circ 2$	–	$55^\circ 6$
-38.2	$280'' 3$	132 683	.49	32.5	81.9	67.8	62 548	56.4
.0	205.1	83 037	.81	345.6	75.9	74.3	26 357	58.1
38.2	280.3	132 683	.98	300.3	50.6	114.6	28 090	75.9
78.3	–	–	1.00	191.2	86.3	236.0	–	124.3

yield for the latter a mass on the order of 0.02–0.05 in the solar units. However, the insufficient accuracy of our data prevents the determination of the orbit of the unseen body.

DETERMINATION OF THE FAMILY OF ORBITS OF STAR F RELATIVE TO THE AB PAIR

The hierarchical system (AB)F can be considered as a wide double star and hence the motion of star F can be determined with respect to the center of mass of the AB pair, which we hereafter refer to as component C.

Consider vectors $\boldsymbol{\rho}$ and $\boldsymbol{\mu}$ of the apparent relative positions and motions:

$$\boldsymbol{\rho}_{(F-C)} = \boldsymbol{\rho}_{(A-C)} + \boldsymbol{\rho}_{(F-A)} = \boldsymbol{\rho}_{(B-C)} + \boldsymbol{\rho}_{(F-B)},$$

$$\boldsymbol{\mu}_{(F-C)} = \boldsymbol{\mu}_{(A-C)} + \boldsymbol{\mu}_{(F-A)} = \boldsymbol{\mu}_{(B-C)} + \boldsymbol{\mu}_{(F-B)}.$$

Stars A and B can be treated as twin companions of equal mass. We then have

$$\boldsymbol{\rho}_{(F-C)} = \frac{1}{2}(\boldsymbol{\rho}_{(F-A)} + \boldsymbol{\rho}_{(F-B)}),$$

$$\boldsymbol{\mu}_{(F-C)} = \frac{1}{2}(\boldsymbol{\mu}_{(F-A)} + \boldsymbol{\mu}_{(F-B)}).$$

The inferred apparent-motion parameters are listed in the last column of Table 5. The relative radial velocity is equal to

$$\begin{aligned} \Delta V_{r(F-C)} &= V_{rF} - (V_{rA} + V_{rB})/2 \\ &= -0.3 \pm 0.4 \text{ km s}^{-1}. \end{aligned}$$

No radius of curvature was inferred and we therefore can only compute a family of possible orbits that depend on the adopted total mass \mathcal{M}_{A+B+F} and inclination β of the radius vector of star F to the sky plane. We now assume that $\mathcal{M}_{A+B+F} = 1.9\mathcal{M}_\odot$ and find, according to formula (2):

$$3762.5 \leq r \leq 9803.7\mathcal{M}_{A+B+F} = 18\,627.0 \text{ AU}.$$

This implies that the angle β should be constrained to the $-78^\circ 3 \leq \beta \leq +78^\circ 3$ interval.

Table 6 gives the elements of selected orbits of the family constricted corresponding to the extreme β values and to $\beta = \pm 38^\circ 2$, which, according to Kleiber's theorem, correspond to the average statistical positions.

The last column gives angle ϵ between the orbital momenta of pairs AB and (AB)F. If both orbits are coplanar, $\epsilon = 0^\circ \pm 180^\circ$.

Figure 4 shows eccentricity e , angle ϵ , and true anomaly ν plotted as functions of β . As is evident from the figure, the overwhelming majority of orbits are highly eccentric and have star F is at their apostra. Angle $\epsilon \geq 55^\circ$ for all orbits of the family. The orbit of star F cannot be made coplanar to that of the AB pair even by varying the apparent-motion parameters and radial velocity within their quoted errors.

CONCLUSION

Our main results are as follows:

(1) The orbit for the relatively close pair AB ($\mathcal{M}_{A+B} = 1.4\mathcal{M}_\odot$) was computed by using the apparent-motion parameters deduced from the 35-year-long series of Pulkovo observations and currently available data on the components' parallaxes and radial velocities. This orbit is consistent with previous observations and can be considered best under the conditions in question.

However, some uncertainty remains in the sum of the pair's masses. For example, the conditions (1) and (2) imply that the minimum sum of the masses of components A and B is

$$\mathcal{M}_{\min} = 1.05 \pm 0.08\mathcal{M}_\odot.$$

This result agrees better with the mass-luminosity relation, but the orbit computed with this mass appreciably and systematically deviates from previous observations. To satisfy them, we must significantly change the initial parameters ρ_c , V_r , and p_t , which is unacceptable.

On the other hand, even for masses greater than $1.4\mathcal{M}_\odot$, the orbit can be reconciled, without changing the initial AMP, with old observations. However, this must be done at the expense of the mass-luminosity relation, which implies that the total mass of the two components is approximately equal to $1.1\mathcal{M}_\odot$. Our final decision was to adopt $\mathcal{M}_{A+B} = 1.4\mathcal{M}_\odot$, which is the minimum mass that allows an orbit to be computed that is consistent with observations for the given AMP, V_r , and p_t . We thus allow the existence of a hidden mass (possibly, an unseen companion) in the AB system.

(2) The Pulkovo residuals exhibit a wavelike behavior in ρ with a period and amplitude of 15 years $0''.01$, respectively, possibly indicative of a $\sim 0.05 M_{\odot}$ companion.

(3) We have obtained for the first time an extensive set of relative-position measurements of star F. Assuming that stars A and B have equal masses, as indicated by their spectral types and luminosities, we computed a family of orbits for the distant component F relative to the AB pair. A comparison of the orbit of the AB pair with that of (AB)F leads us to conclude that:

(a) The orbit of the close pair AB has a small eccentricity, whereas the family of orbits of star F is dominated by highly eccentric trajectories;

(b) The orbits are not coplanar. The angle between the orbital planes exceeds 55° .

ACKNOWLEDGMENTS

We are grateful to all observers of the 26-inch refractor. This work was supported by the Russian Foundation for Basic Research (project no. 98-02-16757) and the Ministry of Science of the Russian Federation (project no. 57-01).

REFERENCES

1. Zh. P. Anosova, E. V. Berdnik, and L. G. Romanenko, *Astron. Tsirk.*, No. 1517, 1 (1987).
2. W. Gliese, Veroff. *Astron. Rechen Inst.*, No. 22, 3 (1969).
3. U. Guntzel-Lingner, *Mitt. Astrophys. Obs. Potsdam* **41**, 183 (1955).
4. J. Hoppmann, *Ann. Sternw. Wien* **26**, 7 (1964).
5. A. A. Kiselev, *Theoretical Foundations of Photographic Astrometry* (Nauka, Moscow, 1989), p. 236.
6. A. A. Kiselev and O. V. Kiyeva, *Astron. Zh.* **57**, 1227 (1980) [*Sov. Astron.* **24**, 708 (1980)].
7. A. A. Kiselev and O. V. Kiyeva, *Astrophys. Space Sci.* **142**, 181 (1988).
8. A. A. Kiselev and L. G. Romanenko, *Astron. Zh.* **73**, 875 (1996) [*Astron. Rep.* **40**, 795 (1996)].
9. A. A. Kiselev, O. A. Kalinichenko, G. A. Plyugin, *et al.*, in *Catalog of Relative Positions and Motions of 200 Visual Binary Stars from Pulkovo Observations with the 26-inch Refractor in 1960–1986* (Nauka, Leningrad, 1988), p. 3.
10. O. V. Kiyeva, *Astron. Zh.* **60**, 1208 (1983) [*Sov. Astron.* **27**, 701 (1983)].
11. O. V. Kiyeva, *Izv. Glavn. Astron. Obs. Akad. Nauk SSSR*, No. 201, 44 (1985).
12. O. V. Kiyeva, *Izv. Glavn. Astron. Obs. Akad. Nauk*, No. 208, 17 (1994).
13. P. G. Kulikovskii, *Stellar Astronomy* (Nauka, Moscow, 1985), p. 246.
14. A. A. Tokovinin, *Radial Velocities of Dwarfs in the Solar Neighborhood* (Mosk. Gos. Univ., Moscow, 1990), p. 4.
15. C. E. Worley and G. G. Douglass, *The Washington Visual Double Star Catalog, 1996.0* (US Naval Observatory, 1996).

Translated by A. Dambis

Preliminary Results of the Alignment and Hartmann Tests of the AZT-22 Telescope

Z. Aslan¹, I. F. Bikmaev², É. A. Vitrichenko^{3*}, R. I. Gumerov², L. A. Dembo⁴, S. F. Kamus⁴, V. Keskin⁵, U. Kiziloglu⁶, M. N. Pavlinsky³, L. N. Pantelev⁴, N. A. Sakhbullin², S. O. Selam⁷, R. A. Sunyaev³, I. Khamitov^{1, 8}, and A. L. Yaskovich³

¹ TUBITAK National Observatory, Antalia, Turkey

² Kazan State University, Kremlevskaya ul. 18, Kazan, 420008 Tatarstan, Russia

³ Space Research Institute, Russian Academy of Sciences, Profsoyuznaya ul. 84/32, Moscow, 117810 Russia

⁴ LOMO Joint-Stock Company, St. Petersburg, Russia

⁵ Aegean University, Izmir, Turkey

⁶ Middle East Technical University, Ankara, 06531 Turkey

⁷ Ankara University, Ankara, Turkey

⁸ Astronomical Institute, Academy of Sciences of Uzbekistan, Astronomicheskaya ul. 33, Tashkent, 700052 Uzbekistan

Received October 6, 2000; in final form, November 27, 2000

Abstract—The AZT-22 telescope installed in Turkey (Antalia) was aligned and tested on stars by the Hartmann method. The rms normal deviation of an equivalent optical system is $0.040 \pm 0.016 \mu\text{m}$. The circle of confusion is 0.40 ± 0.04 arcsec in diameter at a 50% energy level. © 2001 MAIK “Nauka/Interperiodica”.

Key words: *astronomical observing techniques, instrumentation*

INTRODUCTION

The assembly of a new Russian telescope (AZT-22), which was installed at the TUBITAK (Scientific and Technical Council of Turkey) National Observatory 50 km from Antalia at Mount Bakyrlytepe (2550 m, $2^{\text{h}}01^{\text{m}}20^{\text{s}}$ E, $36^{\circ}49'30''$ N), was completed in 1999. The telescope was installed in the context of an international project between Russia and Turkey. The main scientific objective is to provide ground-based support for observations carried out onboard the Spectrum–X-Gamma Orbiting Astrophysical Observatory. The AZT-22 observing time was allocated to the project participants: the Kazan State University, the Space Research Institute, and the TUBITAK National Observatory.

The telescope was produced by the LOMO Joint-Stock Company (St. Petersburg). The primary mirror is 1.5 m in diameter. The optical system is based on the Ritchey–Chretien scheme (Gruzdeva *et al.* 1987; Artamonov and Tertitskiĭ 1987). The telescope is supplied with three replaceable secondary mirrors and three lens correctors, allowing observations to be performed with various aperture ratios (1 : 3c, 1 : 7.7, 1 : 7.8c, 1 : 16, 1 : 17c, and 1 : 48). The optical system with aperture ratio 1 : 48 is used in Coude observations.

A similar telescope was installed at Mount Maidanak in Uzbekistan. It was tested under factory condi-

tions, and its optics proved to be of excellent quality: the circle of confusion at an 80% energy level is 0.2–0.4 arcsec in diameter for all optical systems (Artamonov *et al.* 1990; Artamonov 1997). Test observations at the Observatory yielded an estimate of ~ 0.5 arcsec for the circle-of-confusion diameter at a 50% energy level. Since the atmospheric effect was not eliminated, this value is an upper limit on the optics quality. No Hartmann tests were conducted.

After the AZT-22 assembly was completed in Turkey (November 1999), the telescope was aligned (August 2000), and the system with aperture ratio 1 : 77 without corrector (below, 1 : 8) was certified by the Hartmann method. Here, we present the results of this work.

HARTMANN DIAPHRAGM

The Hartmann diaphragm was designed by the Russian side and produced at the TUBITAK National Observatory. The arrangement of holes, their diameters, and separations between them were taken from the recommendations described in Vitrichenko *et al.* (1990). The diaphragm characteristics are

—The arrangement of holes in the nodes of a square grid;

—The total number of holes is 256, but 231 holes were not vignettted;

—The hole diameter is 35 mm;

—The separation between hole centers is 75 mm.

* E-mail address for contacts: vitrich@nserv.iki.rssi.ru

Yet another hole, 20 mm in diameter, was made near the end of the middle horizontal row between ordinary holes in an effort to uniquely reference the processed Hartmann images to coordinates on the primary-mirror surface.

The diaphragms were made with accuracy $\sigma_1 < 0.2$ mm. By this accuracy, we mean the rms deviation of the coordinates of hole centers from the node coordinates of the square grid that describes the Hartmann diaphragm. This deviation was estimated by measuring the coordinates of the centers of several holes located in the horizontal, vertical and diagonal directions.

The required accuracy can be estimated from the formula (Vitrichenko *et al.* 1990)

$$\sigma_2 = f'\delta/z = 2 \text{ mm}, \quad (1)$$

where $f' = 11\,600$ mm is the equivalent focal length, $z = 50$ mm is the distance from the focus to the Hartmann image plane, and $\delta \sim 0.01$ mm = 0.18 arcsec is the measured rms transverse aberration. Formula (1) yields an estimate for the rms error of the Hartmann diaphragm in the case where this error introduces (fictitiously) the same transverse aberration as the actually measured rms transverse aberration of the telescope optics itself. In order that the diaphragm error affected the optics measurement accuracy only slightly, it will suffice to take a factor of 2 smaller error with which the diaphragm is made: $\sigma_2 = 1$ mm. A comparison of σ_1 and σ_2 shows that the diaphragm was made with a sufficient accuracy.

OBTAINING, MEASURING, AND PROCESSING HARTMANN IMAGES

Since the diaphragm was made with a high accuracy, we obtained only post-focal Hartmann images. Obtaining pre-focal images is technically difficult. For imaging, we mounted the CCD array in such a way that the distance from the focus to the image plane was ~ 50 mm. For this arrangement, the Hartmann pattern completely fits into the CCD array, and the image scale is large enough to provide a high accuracy of measuring the coordinates of spot centers.

We used a SBIG ST-8E 1530×1020 CCD array with a pixel size of 9×9 μm . The telescope was pointed at stars near zenith with magnitudes $V \sim 4^m$.

The zenith angle was $< 20^\circ$. Series of images were taken to eliminate atmospheric seeing. The exposure time of each image was ~ 40 s. The best-quality images were used for the processing.

The Hartmann image quality is significantly affected by diffraction, which gives rise to a complex pattern between spots, making it difficult to measure the spots. Imaging practice shows that a satisfactory image quality can be obtained by choosing a filter and a distance from the focus to the CCD array.

A good image was most commonly obtained in *B*. In this band, the contribution of atmospheric seeing is large compared to Johnson's *VRI*, but the diffraction pattern in other bands was bright, making it difficult to measure the images.

Images were measured twice by various techniques. We measured the coordinates of spot centers, first, by using a set of astronomical procedures from the IDL software package and, second, by manually pointing the cursor at the spot center using the CCDOPS code from the CCD software. The two measurements yielded similar results. Three images were obtained for the final telescope certification. The transverse aberrations were determined on each of them and then averaged; the optics parameters were calculated with these average aberrations. When averaging, we estimated the error of a single measurement of the transverse aberration, $\sigma_3 = 1.5$ μm , and the error of the mean for three measurements, $\sigma_4 = 1$ μm . A comparison of σ_4 with the rms transverse aberration of the telescope optics, $\delta \sim 10$ μm , shows that the measurement error has virtually no effect on the optics quality estimates.

The Hartmann images were processed by using a slightly modified HART5 code (Vitrichenko *et al.* 1990).

MIRROR MAP

Figure 1 shows a map of normal deviations for the AZT-22 optical system with aperture ratio 1 : 8. Below, we attribute all errors to the primary mirror for convenience while bearing in mind that the secondary-mirror and telescope-alignment errors contribute to the normal deviations as well.

An examination of Fig. 1 leads us to the following conclusions:

—The largest (in amplitude) errors are located in the northeast and southwest (bumps), as well as in the southeast and northwest (pits);

—These errors are similar in nature to astigmatism, but their values are so small that they have virtually no effect on the star image quality;

—The coma is unnoticeable.

The rms normal deviation is $\sigma_5 = 0.040$ μm , and the mapping error is $\sigma_6 = 0.016$ μm . By comparing the squares of these errors, it is easy to estimate the accuracy of measuring the mirror map by the Hartmann method, $\sim 10\%$.

This accuracy is high enough for the locations and amplitudes of the largest optics defects to be determined.

The map of normal deviations in Fig. 1 was fitted by a function that allowed the primary aberrations to be estimated. The equation is (Born and Wolf 1973)

$$h(x, y) = a_1 + a_2x + a_3y + a_4r^4 + a_5r^3 \cos(\Theta - a_7) + a_6r^2 \cos^2(\Theta - a_8), \quad (2)$$

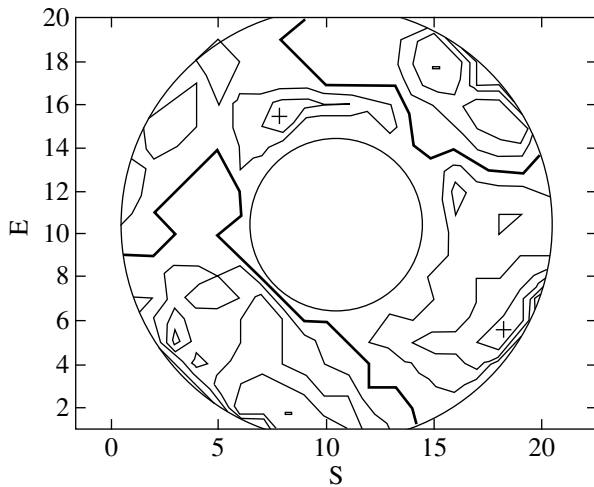


Fig. 1. The map of normal deviations in the form of isolines. The heavy line represents a zero level. The isoline step is $0.02 \mu\text{m}$. The plus and the minus mark the largest and smallest normal deviations, respectively.

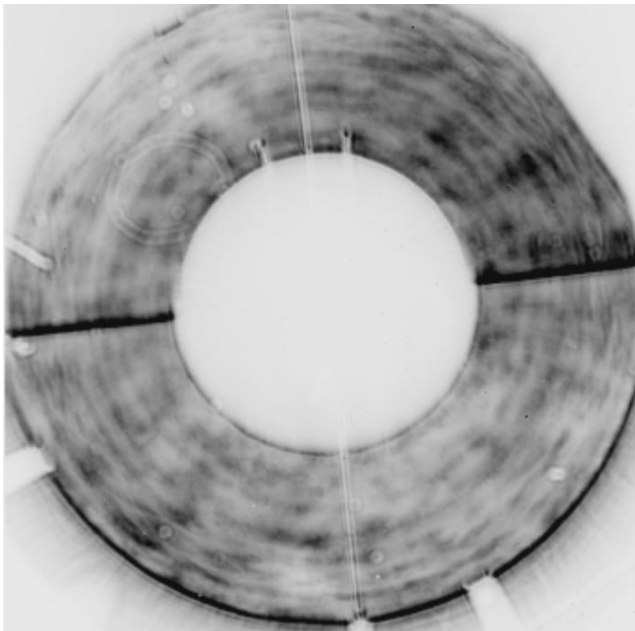


Fig. 2. The shadow pattern of an F/8 equivalent optical system. North is at the top (in the spider direction), and east is to the left. The knife was introduced from north; the colors were reversed.

where $h(x, y)$ are the normal deviations of the mirror map, which is given in units of $0.01 \mu\text{m}$ in our case; the first three terms were introduced to reselect the comparison sphere, the fourth term describes spherical

aberration, and the last two terms describe coma and astigmatism, respectively; x , y , and r are the current coordinates and radius on the primary-mirror surface normalized to the mirror radius; and Θ is the position angle.

The coefficients a_i calculated by least squares are listed in the table. The errors in the coefficients are given in parentheses, in units of the last digit.

For the even-degree expansion terms (a_1, a_4, a_6), the coefficients represent the total amplitude of the error, in units of $0.01 \mu\text{m}$; for the odd-degree coefficients, they represent half the amplitude, in the same units. The coefficients a_7 and a_8 are the coma and astigmatism orientation angles, in radians.

An examination of the table leads us to conclude that astigmatism is the largest aberration. This aberration cannot be removed by alignment.

Astigmatism is extremely difficult to remove by retouching the mirror. However, it is interesting to note that, if astigmatism were removed, the rms error of the optics would be $0.016 \mu\text{m}$, i.e., better than the Marechal limit ($0.02 \mu\text{m}$), which characterizes an upper limit on the error for a virtually ideal mirror.

Figure 2 shows an example of the shadow pattern. An examination of the shadow pattern leads us to conclude that it qualitatively confirms the results obtained by the Hartmann method. It should be kept in mind that the shadow pattern shows a map of derivatives of the optical surface, from south to north in our case; therefore, the map of normal deviations is difficult to directly compare with the shadow pattern. However, the shadow pattern has an order of magnitude higher spatial resolution than the Hartmann method, revealing the fine structure of the mirror surface. In our case, circular furrows are noticeable on the mirror, which are the traces of finishing by a small instrument.

The amplitude of these errors is not large, so they do not deteriorate the star image. However, local defects are dangerous for the Hartmann method, because they displace the spot in the Hartmann image to produce spurious transverse aberrations. As a result, the circle of confusion calculated by the Hartmann method proves to be slightly worse than in reality (Vitrichenko *et al.* 1990).

THE ENERGY CONCENTRATION FUNCTION

The Hartmann total constant with the transverse aberrations along the x and y axes was computed by using the HART5 code, $T = 0.22(2)$ arcsec. By this

The coefficients of expansion of the map of normal deviations in primary aberrations. a_1 – a_6 are in units of $0.01 \mu\text{m}$, while a_7 and a_8 are in radians

i	1	2	3	4	5	6	7	8
a_i	2.36(2)	2.22(3)	4.14(3)	2.73(3)	3.86(3)	–12.08(3)	–2.05(2)	0.54(1)

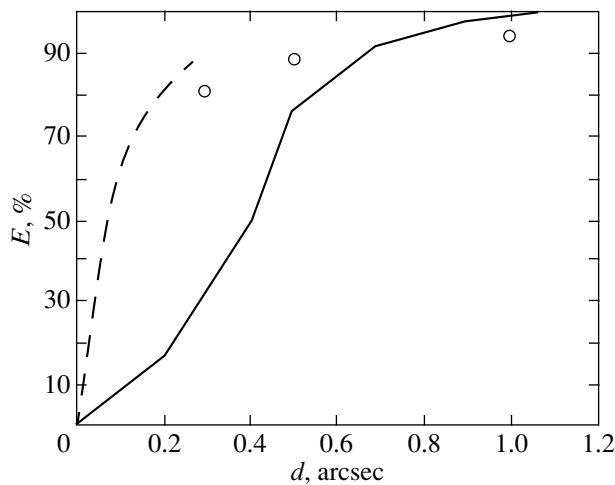


Fig. 3. The energy concentration function calculated by the Hartmann method (solid line) and constructed from factory tests (circles) and a theoretical function for an ideal optical system (dashed line).

parameter, the telescope belongs to the class of high-quality instruments (Vitrichenko *et al.* 1990).

Figure 3 shows the energy concentration function calculated by the Hartmann method. We see from the figure that 80% of the energy is contained in a circle of diameter 0.55 arcsec. By this parameter, the telescope belongs to highly rated instruments.

The results of the factory tests are indicated in Fig. 3 by circles. There is a statistically significant discrepancy for a diameter of 0.3 arcsec. However, it should be kept in mind that the factory tests were performed under different mirror support conditions, and that the factory and Observatory tests were made by the interferometric and Hartmann methods, respectively.

The former and the latter are the wave and geometric methods, respectively. The results obtained by these two methods can differ by several times. This by no means implies that one method yields correct results, while the other yields incorrect results. In the interferometric method, a laser that produces monochromatic light with a large coherence length (hundreds of meters) is used as the source of light. The light from a real star is not monochromatic, and the coherence length is a few tens of a millimeter. Therefore, the data on the circle of confusion obtained in terms of geometrical optics yield results that are closer to the actual star image. This issue remains the subject of debate; it is detailed in Vitrichenko *et al.* (1990).

The dashed line in Fig. 3 indicates the energy concentration function for ideal optics with central screening. At an 80% energy level, the deviation of the circle-of-confusion diameter from that measured with the telescope and at the factory is a factor of 2.8 and a mere 1.5, respectively. These data suggest that the optics quality is comparable to the theoretical limit.

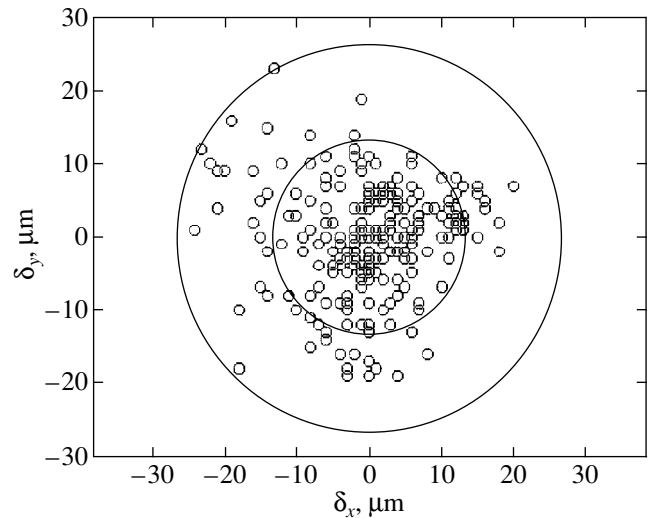


Fig. 4. A point diagram. The transverse aberrations calculated by the Hartmann method are plotted along the axes. The circle diameters are 0.5 and 1.0 arcsec, respectively.

Figure 4 shows a point diagram. We see from this diagram that most points fall within a circle of diameter 0.5 arcsec. The density of points with large aberrations is considerably lower. For this reason, a faint halo visible only on overexposed images will be observed around star images.

A direct image of the star field near zenith was obtained with the same CCD array that was used to obtain the Hartmann image in Johnson's *I* band. The effect of atmospheric seeing in this band is weakest compared to the other bands of this photometric system. The exposure time was 40 s. Figure 5 shows a three-dimensional star image. The Gaussian parameters (in arcsec) calculated by fitting the observed star profile with a bivariate Gaussian are given in the right corner of the figure. The image was obtained on one of the nights with the best seeing in the alignment period.

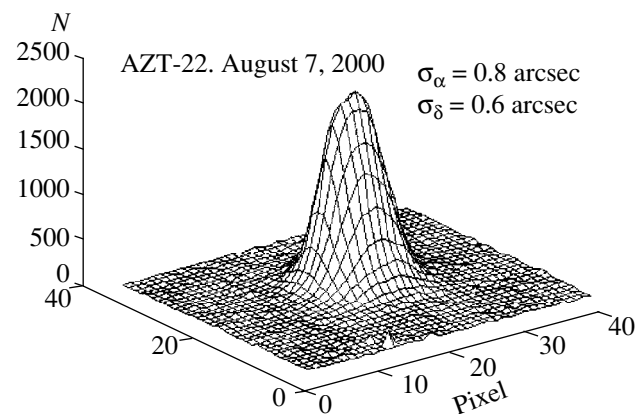


Fig. 5. A three-dimensional image of a field star. Arbitrary pixel numbers are plotted along the coordinate axes. The ordinate is the number of CCD counts.

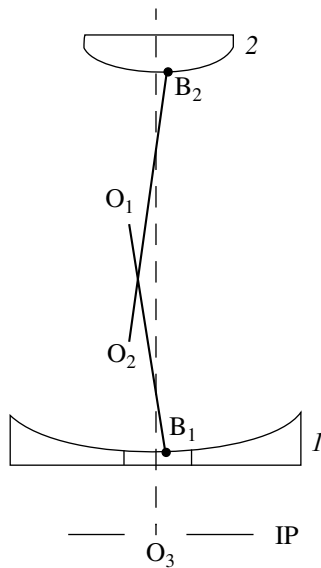


Fig. 6. The scheme of a two-mirror telescope. 1, 2 are the primary and secondary mirrors; O_1 , O_2 are the mirror optical axes; B_1 , B_2 are the mirror vertices; O_3 is the telescope geometric axis; and IP is the image plane.

We see from Fig. 5 that the seeing-disk diameter at half maximum along the declination axis is ~ 1 arcsec, which is a factor of 2.5 larger than the same parameter that characterizes the telescope optics (Aslan *et al.* 1989). Thus, atmospheric seeing rather than the telescope optics limits the resolution even on nights with good seeing.

The seeing-disk diameter along the right ascension axis is slightly larger than that along the declination axis, which is the result of telescope tracking errors. Special tests show that the clock drive has a periodic error with a period of ~ 3 min and semi-amplitude of ~ 1 arcsec. At present, steps are taken to remove this effect. The CCD software contains the Track and Accumulate mode. Observations in this mode allow the telescope tracking error to be eliminated.

It is of interest to compare the AZT-22 optics quality with the optics quality of other world telescopes, which are listed in Vitrichenko *et al.* (1990). The circle of confusion at an 80% energy level is 0.55 arcsec in diameter. A comparison of this parameter for AZT-22 with that for other telescopes indicates that AZT-22 ranks 12th among all the studied telescopes. For example, the circle of confusion for the best 2.7-m telescope at the McDonald Observatory (USA) is 0.12 arcsec in diameter, while the circle of confusion for the worst 2.1-m telescope installed at the same Observatory is 2.7 arcsec in diameter (Kuiper and Middlehurst 1963).

TELESCOPE ALIGNMENT

In the previous sections, we presented the results of the telescope certification. This certification was made

after the telescope alignment. In this section, we describe the basic principles of alignment. Figure 6 schematically shows a two-mirror telescope. This scheme is clear from the caption to the figure. Note, however, that, according to this scheme, the vertices of the mirrors generally do not coincide with their geometric centers.

The coma was removed as follows. A Hartmann image was obtained and processed by the above method. We analyzed the constructed map of normal deviations by using Eq. (2) and obtained data on the primary aberrations similar to those in table. The coefficients a_5 and a_7 were used for the alignment. The former and the latter are the coma amplitude and direction, respectively (a_7 specifies the direction in which the secondary mirror should be displaced relative to the cardinal points).

The displacement Δ and tilt α of the secondary mirror were determined from the relation

$$h = \Delta(r/R_0) + \frac{\Delta(r/R_0)^3(1-e^2)}{2}, \quad (3)$$

hence

$$\Delta = \frac{2a_5}{(r/R_0)^3(1-e^2)}, \quad \alpha = \Delta/R_0. \quad (4)$$

Equation (3) was derived by differentiating the equation of a conic section. In this equation, $r = 501$ mm is the light diameter of the secondary mirror for an on-axis beam, $R_0 = 4840$ mm is its radius of curvature at the vertex, and $e^2 = 7.8$ is the square of the eccentricity (Gruzdeva *et al.* 1987); h are the normal deviations of an equivalent optical system along the coma axis. In this case, we attribute the errors of the optical system to the secondary mirror, but analyze the coma alone, because the coma is assumed to be produced by the decentering of the primary and secondary mirrors.

Model calculations show that the required displacement accuracy of the secondary mirror is ~ 0.02 mm. Unfortunately, the alignment mechanisms were used in such a way that this accuracy could not be achieved. For this reason, the alignment was ceased when the displacement was unfeasible ($\Delta = 0.08$ mm).

CONCLUSION

The tests of the AZT-22 optics have led us to the following conclusions:

—By the errors of the optical surface and by the energy concentration function, the telescope is rated highly in quality, allowing it to be used to solve a wide range of scientific problems;

—The optics errors are of a local nature resembling astigmatism, but the errors of the telescope optics have virtually no effect on star images even on nights with good seeing;

—One of the immediate problems is to eliminate the error of the telescope clock drive, which prevents high-quality imaging of stars.

ACKNOWLEDGMENTS

We wish to thank the management of the TUBITAK National Observatory and its staff for help with this work and I.M. Varvarkina for the participation. We are also grateful to G.A. Avanesov, B.P. Artamonov, V.S. Bychkova, O.N. Bugaenko, B.S. Dunaev, and Yu.M. Chesnokov for helpful discussions.

REFERENCES

1. B. P. Artamonov, Proc. SPIE **2871**, 737 (1997).
2. B. P. Artamonov and M. I. Tertitskiĭ, *Methods for Increasing the Efficiency of Optical Telescopes* (Mosk. Gos. Univ., Moscow, 1987), p. 132.
3. B. P. Artamonov, V. V. Bruevich, O. N. Bugaenko, *et al.*, Preprint No. 16, GAISh (Sternberg Astronomical Institute, Moscow, 1990).
4. Z. Aslan, C. Aydin, Z. Tunca, *et al.*, *Astron. Astrophys.* **208**, 385 (1989).
5. M. Born and E. Wolf, *Principles of Optics* (Pergamon, Oxford, 1969; Nauka, Moscow, 1973).
6. K. M. Gruzdeva, M. V. Lobachev, B. A. Chernaya, and L. E. Yakhuntova, *Methods of Effectiveness Rise of Optical Telescopes* (Mosk. Gos. Univ., Moscow, 1987), p. 160.
7. *Telescopes*, Ed. by G. P. Kuiper and B. M. Middlehurst (Univ. of Chicago Press, Chicago, 1960; Inostrannaya Literatura, Moscow, 1963).
8. É. A. Vitrichenko, V. P. Lukin, L. A. Pushnoiĭ, and V. A. Tartakovskii, *Problems of Optical Tests* (Nauka, Novosibirsk, 1990).

Translated by V. Astakhov

Orbital Evolution of Uranus's New Outer Satellites

M. A. Vashkov'yak*

Keldysh Institute of Applied Mathematics, Russian Academy of Sciences, Miusskaya pl. 4, Moscow, 125047 Russia

Received November 18, 2000

Abstract—Data on three recently discovered satellites of Uranus are used to determine basic evolutionary parameters of their orbits: the extreme eccentricities and inclinations, as well as the circulation periods of the pericenter arguments and of the longitudes of the ascending nodes. The evolution is mainly investigated by analytically solving Hill's double-averaged problem for the Uranus–Sun-satellite system, in which Uranus's orbital eccentricity e_U and inclination i_U to the ecliptic are assumed to be zero. For the real model of Uranus's evolving orbit with $e_U \neq 0$ and $i_U \neq 0$, we refine the evolutionary parameters of the satellite orbits by numerically integrating the averaged system. Having analyzed the configuration and dynamics of the orbits of Uranus's five outer satellites, we have revealed the possibility of their mutual crossings and obtained approximate temporal estimates. © 2001 MAIK "Nauka/Interperiodica".

Keywords: *Uranus's outer satellites, orbital evolution*

INTRODUCTION. INPUT DATA

The discovery of three new celestial objects, probable satellites of Uranus, was first reported in August 1999. Two of them were found by Kavelaar, Gladman, Holman, Petit, and Scholl (Marsden 1999a), and the third was found by Gladman, Nicholson, and Burns (Marsden 1999b). It was initially assumed that the Uranus-centric orbits of all three probable satellites had an eccentricity of about 0.4, while the satellites themselves executed direct motion. In March 2000, three systems of elements were obtained for these satellites of Uranus, designated as S/1999 U 1, 2, and 3 (Marsden 2000a, 2000b). In these systems, only one of the new satellites had direct motion, while the orbits of the other

two had inclinations to the ecliptic larger than 90° . Finally, in July–August 2000, refined orbital elements were calculated for the new satellites (Marsden 2000c–2000e), while the satellites themselves received official names:

Uranus XVIII = S/1999 U 3 (Prospero),

Uranus XIX = S/1999 U 1 (Setebos),

Uranus XX = S/1999 U 2 (Stephano) (Green 2000).

Table 1 gives the orbital elements for these satellites taken from Marsden (2000c–2000e). In this table, t_0 is the initial epoch, T is the time of pericenter passage, e is the eccentricity, q is the pericenter distance, a is the semimajor axis, n is the mean motion, and P is the orbital period. The angular elements ω —the argument of the pericenter latitude, Ω —the longitude of the

Table 1. Orbital elements for Setebos, Stephano, and Prospero

Elements	Setebos	Stephano	Prospero
t_0	2000 September 13.0	2000 September 13.0	2000 September 13.0
T	2003 March 31.3912	2000 July 17.8212	2001 September 17.7268
e	0.494329	0.145863	0.327449
q , AU	0.061537	0.045348	0.072442
a , AU	0.121694	0.053092	0.107712
n , deg/day	0.1535250	0.5327706	0.1843682
P , year	6.420	1.850	5.346
ω , deg	2.1890	29.8432	173.5689
Ω , deg	249.8452	189.4991	320.1468
i , deg	148.8285	141.5385	146.3403

* E-mail address for contacts: vashkov@spp.keldysh.ru

ascending node, and i —the inclination refer to the ecliptic plane and equinox 2000.0.

The discovery of Setebos, Stephano, and Prospero considerably supplemented the family of Uranus's outer satellites. Together with Caliban and Sycorax discovered in 1997, they formed a distinctive system of distant satellites with retrograde motion. The semimajor axes of the system's highly eccentric orbits take on values from 0.045 to 0.12 AU (or from 7.2 to 18.2 million km), so the solar attraction has a major perturbing effect on the motion of all these satellites. Below, we therefore use a general solution of Hill's double-averaged problem to analyze the orbital evolution of Setebos, Stephano, and Prospero. Of course, this evolutionary model can serve only as the initial approximation of the real model and can give nothing but crude estimates of the parameters that characterize variations in the elements of satellite orbits with the longest periods. These estimates can be obtained by qualitatively analyzing an integrable satellite version of the double-averaged circular restricted three-body problem (Lidov 1961) and its general solution (Vashkov'yak 1999), which has already been used to study the orbital evolution of Caliban and Sycorax. Jacobson (1999) numerically integrated the strict (nonaveraged) equations of motion for these satellites by taking into account perturbations from the Sun, Jupiter, Saturn, and Neptune. A comparison of the results shows that the analytic solution of the evolutionary problem yields mean eccentricities, inclinations, and circulation periods of the pericenter arguments and of the longitudes of the ascending nodes that differ approximately by 10% from their values obtained by numerical integration. This gives grounds to use the proposed analytic solution as the zero approximation (intermediate orbit) when constructing a comprehensive theory of the motion of Uranus's distant satellites.

ORBITAL EVOLUTION OF SETEBOS, STEPHANO, AND PROSPERO

The basic characteristic evolutionary parameters of satellite orbits can be obtained by solving Hill's averaged problem. For each of the three satellites, Table 2 gives the first integrals of the problem,

$$c_1 = (1 - e^2)\cos^2 i, \quad c_2 = e^2(2/5 - \sin^2 i \sin^2 \omega),$$

the extreme eccentricity e and inclination i , as well as the circulation periods of the pericenter argument ω and of the longitude of the ascending node Ω .

The orbital evolution of the three satellites in question is qualitatively the same as that of Caliban and Sycorax. The variations in eccentricities and inclinations are oscillatory in pattern with twice the frequency of variations in pericenter argument (Figs. 1a, 1b, 2a, 2b, 3a, 3b). The elements ω and Ω increase while changing mainly in a secular fashion with small periodic variations (Figs. 1c, 1d, 2c, 2d, 3c, 3d). There is a clear quantitative difference in the evolutionary parame-

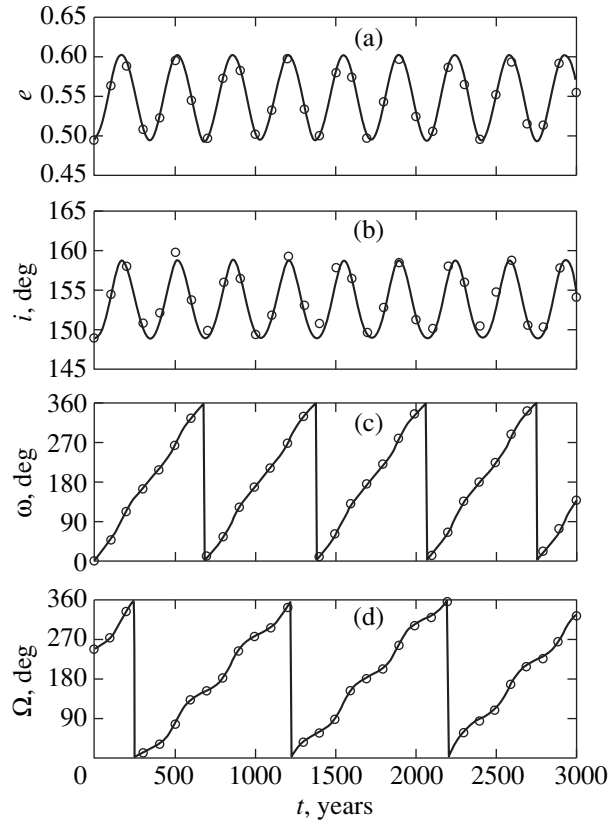


Fig. 1. Setebos's orbital elements versus time for $e_U = i_U = 0$: (a) eccentricity, (b) inclination, (c) pericenter argument, and (d) longitude of the ascending node.

ters of the farthest (and most perturbed by the Sun) satellite Setebos; the circulation periods of ω and Ω for its orbit are shortest among all five outer satellites of Uranus and do not exceed a few thousand years.

The solid lines in Figs. 1–3 correspond to the analytic solution of Hill's double-average problem with $e_U = i_U = 0$. The values obtained by numerically integrating a fuller evolutionary system that includes small variations in i_U and e_U with time [to be more precise, long-period variations in $e_U \cos(\omega_U + \Omega_U)$, $e_U \sin(\omega_U + \Omega_U)$, $\sin i_U \cos \Omega_U$, and $\sin i_U \sin \Omega_U$, according to the

Table 2. Characteristic evolutionary parameters for Setebos, Stephano, and Prospero

Parameters	Setebos	Stephano	Prospero
c_1	0.5532	0.6001	0.6185
c_2	0.09765	0.00647	0.04247
e_{\min}	0.494	0.127	0.326
e_{\max}	0.603	0.314	0.469
i_{\min} , deg	149	141	146
i_{\max} , deg	159	145	153
T_ω , year	691	5148	1035
T_Ω , year	944	5300	1407

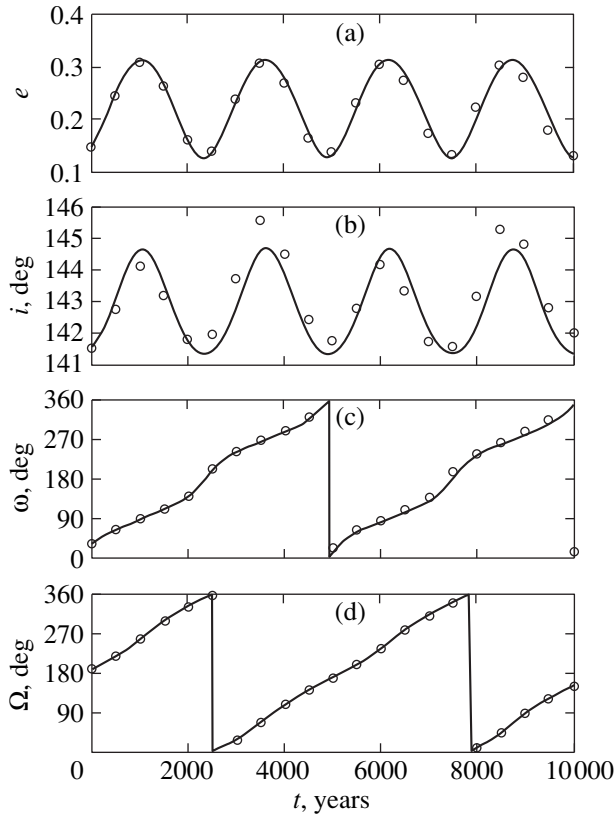


Fig. 2. Stephano's orbital elements versus time for $e_U = i_U = 0$: (a) eccentricity, (b) inclination, (c) pericenter argument, and (d) longitude of the ascending node.

Lagrange–Brower–Wurkom theory (Sharaf and Budnikova 1967)] are marked by circles. Here, ω_U and Ω_U denote the argument of the perihelion latitude and the longitude of the ascending node of Uranus's orbit, respectively. This evolutionary system in elements is obtained by using an expression for the normed perturbing function W of Hill's double-averaged problem (at $e_U = i_U = 0$) supplemented by terms $\sim \sin i_U$ (Vashkov'yak and Teslenko 1998), $\sim e_U^2$, and $\sim ae_U/a_U$ (a_U is the semimajor axis of Uranus's orbit):

$$\begin{aligned}
 W = & \{2e^2 + (5e^2 \cos 2\omega - 3e^2 - 2)[\sin^2 i \\
 & - 0.5 \sin 2i_U \sin 2i \cos(\Omega_U - \Omega) - 0.5 \sin^2 i_U \sin^2 i (3 \\
 & + \cos 2(\Omega_U - \Omega))] - 5e^2 \sin 2i_U \sin 2\omega \sin i \sin(\Omega_U - \Omega) \\
 & - e^2 \sin^2 i_U [3 - 5(\cos 2\omega \cos 2(\Omega_U - \Omega) \\
 & + \sin 2\omega \sin 2(\Omega_U - \Omega) \cos i)]\} (1 - e_U^2)^{-3/2} \\
 & + Be \{ (4 + 3e^2) [(5 \sin^2 i - 4) \cos \omega \cos(\Omega - g_U) \\
 & + (4 - 15 \sin^2 i) \cos i \sin \omega \sin(\Omega - g_U)] \\
 & + 35e^2 \sin^2 i [\cos i \sin 3\omega \sin(\Omega - g_U) \\
 & - \cos 3\omega \cos(\Omega - g_U)] \},
 \end{aligned}$$

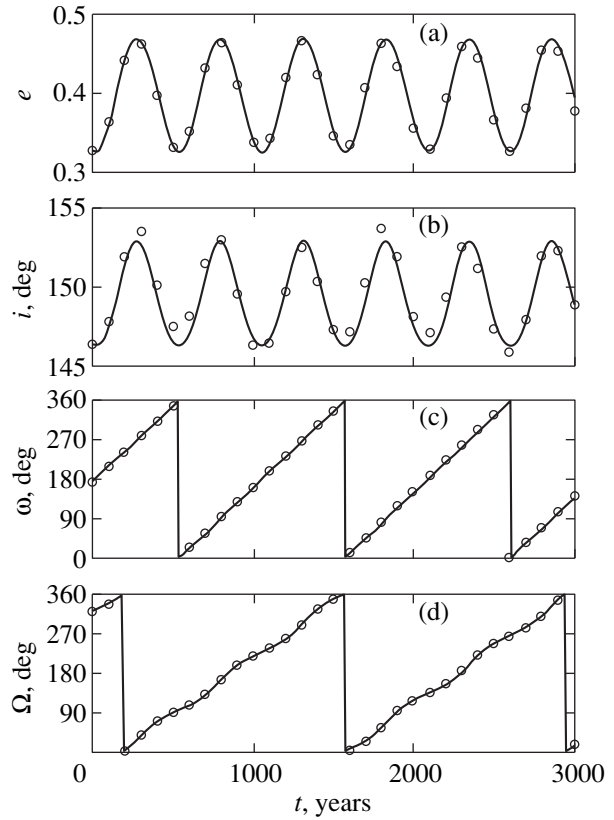


Fig. 3. Prospero's orbital elements versus time for $e_U = i_U = 0$: (a) eccentricity, (b) inclination, (c) pericenter argument, and (d) longitude of the ascending node.

where $B = \frac{5ae_U}{16a_U(1 - e_U^2)}$, $g_U = \omega_U + \Omega_U + 180^\circ$ is the Uranus-centric longitude of the Sun's orbital pericenter.

In the parallaxic terms of $W(\sim B)$, we discarded terms $\sim ae_U \sin i_U / a_U$.

Allowing for Uranus's orbital evolution results only in insignificant quantitative changes (compared to Hill's problem) in the time dependences of satellite orbital elements. These changes show up most clearly in the dependences $i(t)$ (Figs. 1b, 2b, 3b). For Stephano's orbit, they are most pronounced, because i_{\min} and i_{\max} are close (Fig. 2b).

If a time interval much longer than the circulation periods of ω and Ω is considered, then the effect of Uranus's orbital inclination may cause a significant deviation from the analytic solution of the integrable problem, because $0^\circ.5 \leq i_U \leq 2^\circ.5$. Note that, although Uranus's orbital eccentricity is also nonzero ($0.012 \leq e_U \leq 0.07$), its effect shows up only in terms $\sim e_U^2$ and $\sim ae_U/a_U$ and is marginal for the satellites under consideration.

Figures 4–6 show projections of the numerical solution of the fuller evolutionary system with variations in e_U , i_U , ω_U , and Ω_U in the interval 400 000 years (an

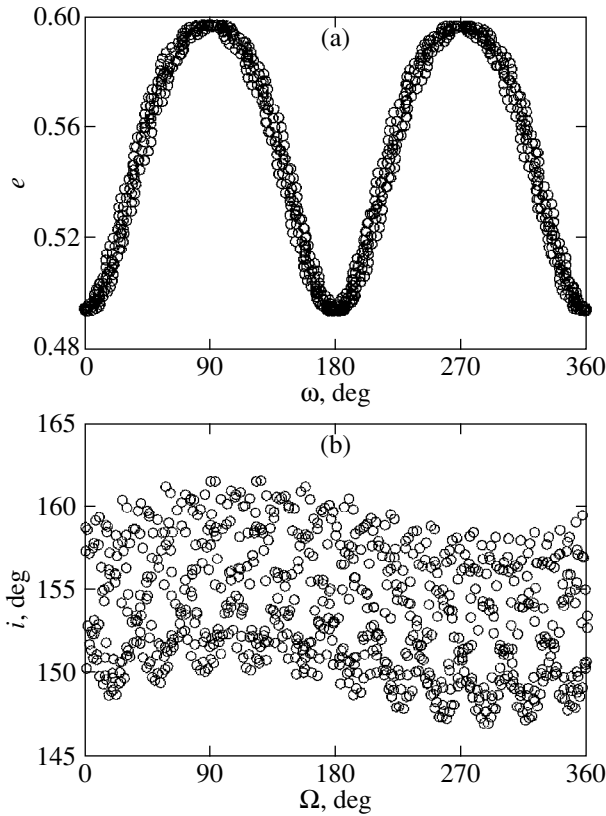


Fig. 4. Variations in Setebos's orbital elements for $e_U \neq 0$, $i_U \neq 0$ in the interval 400 000 years: (a) projection onto the (ω, e) plane; (b) projection onto the (Ω, i) plane.

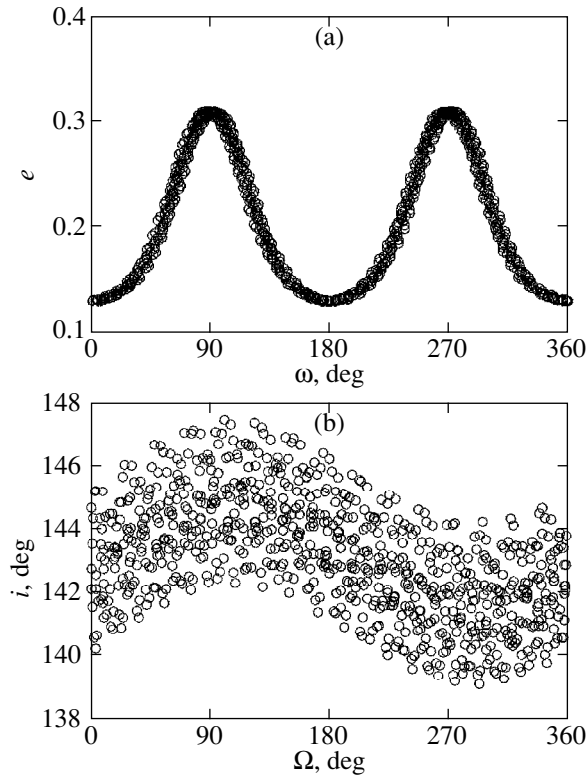


Fig. 5. Variations in Stephano's orbital elements for $e_U \neq 0$ and $i_U \neq 0$ in the interval 400 000 years: (a) projection onto the (ω, e) plane; (b) projection onto the (Ω, i) plane.

approximate libration period of Ω_U) onto the (ω, e) and (Ω, i) planes. The circles in these figures correspond to times separated by 500 years. We see from Figs. 4a, 5a, and 6a that the elements e and ω change virtually along the integral curve of the integrable problem ($e_U = i_U = 0$), while the extreme e differ from those in Table 2 by no more than 0.01. At the same time, the ranges of variations in satellite orbital inclinations can differ from analytic estimates approximately by 2:5 (this is the maximum of i_U).

MUTUAL CROSSINGS OF THE ORBITS OF URANUS'S OUTER SATELLITES

The configuration and evolution of the orbits of Uranus's satellites under consideration are such that their mutual crossings can occur (and actually occur) in the course of time. The significant variations in orbital eccentricities and, as a result, the corresponding variations in pericenter and apocenter distances are a peculiarity of the system of Uranus's outer satellites. Table 3 gives the ranges of these variations for all five outer satellites with the constraint $a = \text{const}$ (this is the integral of the averaged problem).

Figure 7 serves as a graphical illustration of this table. For each of the five semimajor axes a , this figure shows the bars that correspond to the variations in r_π (below the dashed line) and r_α (above the dashed line).

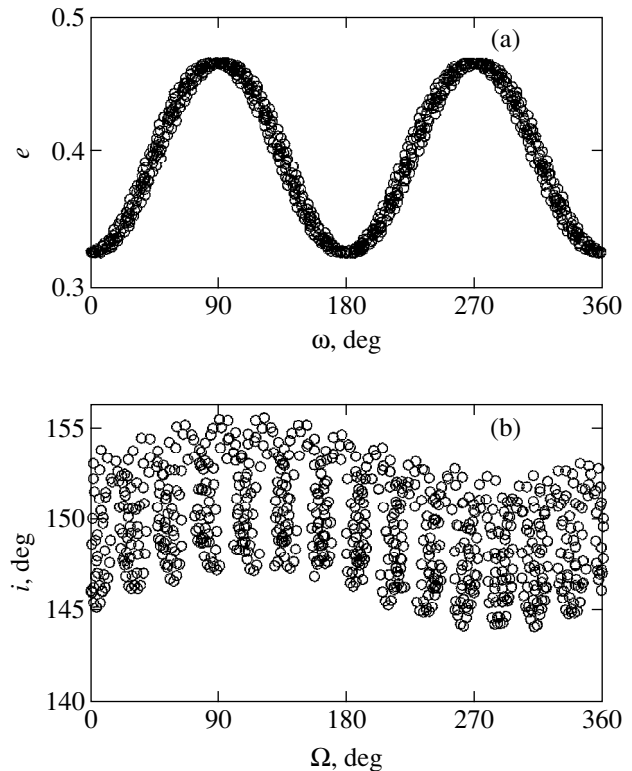


Fig. 6. Variations in Prospero's orbital elements for $e_U \neq 0$ and $i_U \neq 0$ in the interval 400 000 years: (a) projection onto the (ω, e) plane; (b) projection onto the (Ω, i) plane.

Table 3. Ranges of variations in pericenter (r_π) and apocenter (r_α) distances of the orbits of Uranus's outer satellites

Satellite	a , million km	$r_{\pi \min}$, million km	$r_{\pi \max}$, million km	$r_{\alpha \min}$, million km	$r_{\alpha \max}$, million km
Caliban	7.17	5.12	6.62	7.72	9.22
Stephano	7.94	5.45	6.93	8.95	10.43
Sycorax	12.21	5.07	6.15	18.27	19.35
Prospero	16.11	8.55	10.86	21.36	23.67
Setebos	18.21	7.23	9.21	27.21	29.18

Table 4. Approximate times of mutual crossings of the orbits of Uranus's outer satellites in the recent past (in years)

Satellite	Caliban	Stephano	Sycorax	Prospero	Setebos
Caliban	0	385	135	>400000	491
Stephano	385	0	15	744	468
Sycorax	135	15	0	134	44
Prospero	>400000	744	134	0	17
Setebos	491	468	44	17	0

The apsidal points of each orbit can lie within the spherical layers

$$r_{\pi \min} \leq r_\pi \leq r_{\pi \max}, \quad r_{\alpha \min} \leq r_\alpha \leq r_{\alpha \max}.$$

If the condition

$$r_{\alpha \max}(j) < r_{\pi \min}(k)$$

is satisfied for two evolving orbits with numbers j and k , then these orbits cannot cross for any i , ω , and Ω . An analysis of Table 3 and Fig. 7 indicates that this condition is not satisfied for any pair of the above orbits. Consequently, as i , ω , and Ω vary, the conditions under which the orbits will cross can be satisfied. Our numerical calculations with allowance for Uranus's orbital evolution yielded approximate times of mutual cross-

ings of the orbits for each pair of satellites and, in particular, the times most recent in the past (Table 4).

By comparing the data in Tables 3 and 4 and in Fig. 7, we can note that for the pairs of orbits (1–2) Stephano–Sycorax and Prospero–Setebos with the closest times of crossing in the past, the following conditions are satisfied:

$$r_{\pi \min}(2) < r_{\pi \min}(1) < r_{\alpha \max}(1) < r_{\alpha \max}(2),$$

i.e., the spherical apsidal layers of Stephano and Prospero are entirely within the wider layers with the boundaries $r_{\pi \min}(2) \longleftrightarrow r_{\alpha \max}(2)$ of Sycorax and Setebos, respectively. Thus, the crossing frequency of the above pairs of orbits also increases.

By contrast, for the pair orbits (1–2) Caliban–Prospero without any crossings, at least over the libration period of Ω_U (≈ 400000 years), the following conditions are satisfied:

$$r_{\pi \min}(1) < r_{\pi \min}(2) < r_{\alpha \max}(1) < r_{\alpha \max}(2),$$

the difference $r_{\alpha \max}(1) - r_{\pi \min}(2) \approx 0.67$ million km is relatively small, so the spherical apsidal layers intersect only slightly. Under these conditions, there may not be any crossings of the orbits at all, or they cross rarely.

CONCLUSION

We have studied the key features of the orbital evolution of Uranus's outer satellites in terms of Hill's double-averaged problem (a satellite version of the restricted circular three-body problem). Our estimates yielded approximate extreme parameters of the evolving orbits (eccentricities and inclinations), as well as circulation periods of the pericenter arguments and of the longitudes of the ascending nodes. These estimates were refined for the model of Uranus's evolving orbit. Allowing for additional perturbations, which are primarily attributable to Uranus's orbital motion and to the attraction by Jupiter, Saturn, and Neptune, modify the estimates of evolutionary parameters, with these modifi-

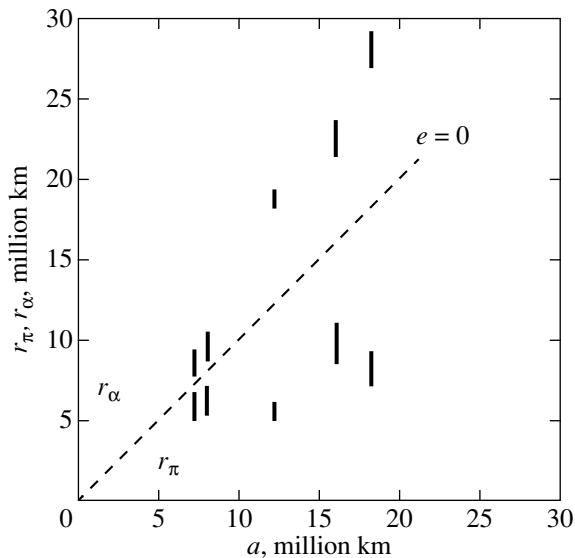


Fig. 7. Ranges of variations in pericenter and apocenter distances for various orbital semimajor axes of Uranus's outer satellites.

cations being particularly noticeable during crossings of the orbits of outer satellites. Therefore, the data in Table 4 should be perceived more as mean times that characterize the intervals between successive crossings of the orbits, when the probability of close satellite encounters increases. For the actual possibility of their close encounters to be analyzed, accurate theories of the motion must be constructed.

ACKNOWLEDGMENTS

I wish to thank N.M. Teslenko for help with the calculations. I am also grateful to V.A. Brumberg, Yu.A. Chernetenko, V.S. Ural'skaya and, particularly, G.R. Kastel' for assistance in obtaining information about Uranus's new satellites.

This work was supported by the Council of Grants of the President of Russia and the State Support for Leading Scientific Schools (grant no. 00-15-96036).

REFERENCES

1. D. W. E. Green, IAU Circ., No. 7479, 3 (2000).
2. R. A. Jacobson, Bull. Am. Astron. Soc. **31** (4), 1224 (1999).
3. M. L. Lidov, *Iskusstv. Sputniki Zemli* **8**, 5 (1961).
4. B. G. Marsden, IAU Circ., No. 7230 (1999a).
5. B. G. Marsden, IAU Circ., No. 7248 (1999b).
6. B. G. Marsden, IAU Circ., No. 7385 (2000a).
7. B. G. Marsden, Minor Planet Circ., No. 38 949 (2000b).
8. B. G. Marsden, IAU Circ., No. 7447, 1 (2000c).
9. B. G. Marsden, IAU Circ., No. 7450, 2 (2000d).
10. B. G. Marsden, IAU Circ., No. 7473 (2000e).
11. Sh. G. Sharaf and N. L. Budnikova, *Byull. Inst. Teor. Astron. Akad. Nauk SSSR* **11**, 231 (1967).
12. M. A. Vashkov'yak, *Pis'ma Astron. Zh.* **25**, 554 (1999) [*Astron. Lett.* **25**, 476 (1999)].
13. M. A. Vashkov'yak and N. M. Teslenko, *Pis'ma Astron. Zh.* **24**, 474 (1998) [*Astron. Lett.* **24**, 406 (1998)].

Translated by V. Astakhov